Additive Manufacturing of Functionally Graded Materials: Insights from Advanced Characterization and Computational Thermodynamics

by

Jorge Valilla Robles

A dissertation submitted in partial fulfillment of the requirements for the degree of Doctor of Philosophy in

Material Science & Engineering

Universidad Carlos III de Madrid

Advisor(s):

Damien Tourret
Ilchat Sabirov

Tutor:

Paula Alvaredo Olmos

December 2025

"Para las mini Valillas, Nora y Eira. Si algún día leéis esto, será que ya no soy el único científico loco de la familia".

"Everything is changing. I guess I should warn my mum. But she'll just be excited".

Kevin Parker

ACKNOWLEDGEMENTS

En más de una ocasión he meditado como sería escribir estas palabras, más bien llevo unos años dándole vueltas. Nunca mejor dicho, hacer una tesis es todo un viaje. Un viaje que pocos se atreven a emprender y casi nadie te sabe explicar. Cada viaje es una experiencia única y definitivamente, este lo ha sido y con creces. Ando escribiendo estas palabras en mi penúltimo día en este asiento, tras un apagón que nos dejó colgados, cuando ya veía la luz al final del túnel. Pero más allá de apagones, nevadas, pandemias e historias no aptas para un documento acádemico, aquí vengo a dar una pequeña muestra de cariño a muchos de mis compañeros de viaje estos años, no comparable con todo lo que he recibido a cambio.

First and foremost, I want to acknowledge my two PhD advisors, Damien and Ilchat. Thank you for your support and for taking a chance on me. Damien, you've not only been the best supervisor and boss I could ask for, but also a constant source of inspiration and wisdom over the years. I deeply admire your scientific knowledge, but even more so, your graceful and joyful approach to your work. You've shown me that spreading the word of science fairly is a right, not a privilege. Thank you for your unwavering availability, patience, and encouragement through all the ups and downs, and for creating such a welcoming group atmosphere. I'm honoured to be a small part of your journey—and grateful that you've become an important part of mine, too. Ilchat, thanks for being so welcoming and helpful, even if it took me a while to master how to polish and properly prepare my ugly-looking samples. You always had a new and constructive point of view that helped me push forward my work until today. I know you will keep pushing the (grain) boundaries of metallurgy!

También me gustaría agradecer a Paula, por su apoyo y ayuda como tutora académica y colaboradora en diferentes proyectos, además de darme la oportunidad de probar la docencia. También quiero trasladar estas palabras de agradecimiento a Jose Manuel y Mónica, por formar parte de esta tesis y por vuestro apoyo a lo largo de los años desde la UC3M o desde IMDEA. Asímismo, quiero agradecer a Pilar (AIMEN) por su apoyo y asesoramiento durante el proyecto MULTI-FAM, y

a Marta y Teri, por su inestimable ayuda tratando muestras a última hora.

Por supuesto, y en referencia al proyecto mencionado, esta tesis no habría sido posible sin el apoyo de los diferentes proyectos de los que he formado parte (MULTI-FAM, SALMONE, DAMAS, EARTH & IRIDESCENTE) al igual que la beca de movilidad María-de-Maeztu que me permitió financiar mi estancia en Colorado School of Mines. For that, I want to thank Amy for giving me the chance to be part of the team at CSM and for giving me access to amazing people and equipment at Los Alamos National Laboratory. I also want to thank my former wild-west colleagues (Adriana, Tomas, Nate, Finn, Valava, and all the downtown crew) for making those three months in Golden such a 'blast' both in and out of the lab!

Y de Colorado volvemos a TecnoGetafe, porque este viaje no tiene sentido sin mencionar la que ha sido mi casa estos años, IMDEA. He tenido la suerte de formar parte de muchas familias, –siendo mi grupo de investigación una de ellas–. I want to thank Ahmed, Adrian, and Rouhollah for being both my postdocs and mentors, and Thomas and Jose for being some of the best friends that phase-field and solidification could ever buy. I hope your time here left you with some good memories and maybe just a bit of Mediterranean scar tissue. Thanks also to Mohammad and Raúl for keeping up with the marathonian group meetings and being the next generation of TC-wizards. And for the newcomers (Valerio, Mohammad, Vittoria, Moisés), enjoy and take care of the place! You're in good hands.

Por supuesto, las mil y una familias que he formado aquí se deben a la calidad humana que me he encontrado, en muchos casos por puro azar. Y es que parece mentira que gente como NachoR, el Dundee de mi cocodrilo, nunca se cruzó en mi camino en Luleå o Barcelona pero si en un mexicano en Madrid y es el único friki del universo que entiende mis referencias a No Dunks. También parece mentira que Guille y yo compartiéramos aula durante cuatro años sin más, y ahora casi hasta compartimos perro, padre, busquedas en Wikipedia y un gran talento para el karaoke. Eu probablemente cruzó mi camino en algun momento en Ciu y sin saberlo entonces, se convirtiría en mi pythonisa y eterna compañera de padel y K2s, aunque hace ya un tiempo que se marchó a custodiar el norte de Portugal. Algo parecido a Carmen y su Castilla. Siempre será mi fiel Pocahontas, con su inmensa determinación, y ojála siempre sea mi contacto directo con el gobierno cuando sea presidenta a lomos de Babieca. A Javi en cambio, le tuve que perseguir 2 años por Europa durante el master para coincidir con él y, tras 2 esquinces e innombrables lesiones e historias, yo sigo vivo y él, casado. Parece completamente irónico hablar de como Ángela me conocía por mi lamentable monólogo de graduación y ahora me acompaña en mis paseos perrunos de madrugada y viajes alpinos, o como evité conocer a NachoE por no ir de visita a Cranfield en 2018 y ahora es mi profesor de ski, yo su padre en el padel y hace tiempo que ya conquistó little pieces of my heart. Y a David, mi mayor drugo y compañero de baile entre reinas lagartas, no le conocí por embarcarme en ese master ya mencionado. Espero también que Lola no

cuelgue el doctorado como si hizo con las botas, y que sigamos synchrotronizados con nuestro Atleti. Como no olvidarme de Andrés, la primera persona que me tomo bajo el brazo, que empezó acero y ahora vive en la sierra donde el sornoluce. Echaré de menos la infinita positividad y alegría de un corazón incomprendido como el de Davide, los canticos mudos de Oscar y como pone de los nervios a Jesús, mi fiel compañero de mesa que tanto tuvo que aguantarme (mientras Carlos se reía y nos padreaba a todos con su filosofía de vida). También espero que Marcos nos saque de pobres y me lleve en sus tablas de paddle surf allá donde el VAR no cancele penaltis. Espero poder seguir celebrando los farewells de Cillian tras 3 años despidiendose y si al final se va, sus reels me harán sentir que no está lejos. Y por supuesto, espero que Alberto (el jefe mas gracioso de IMDEA), María (cuya suegra seguro que acabará siendo medio ficus) y Venky (el futuro millonario de la C2) no dejen de preguntarme cosas de TC, aunque tenga 50 años, hijos y una hipoteca. No tendría la fuerza de seguir escribiendo estas lineas sin la infinita energia proporcionada por el caldo gallego de Teri (y su infinita sabiduría en el Spotle), el humor absurdo, inocente y puro de Laura y por el apoyo de todos mis compañeros de la 2da planta y de alguna otra en los cafes y planes nocturnos (Maral, Saumya, Paul, Yuyao, Pedro, Isa, Ángela DLC, Nabil, Jorge, ...), que así como el resto, tuvieron que comerse buenas chapas y reirme las tonterías. Por último, no puedo cerrar esta etapa sin mencionar todas esas personas que han hecho de IMDEA un lugar donde es fácil ir a trabajar. Empezando por todo el personal y técnicos de laboratorio (Amalia, Manu, Vanesa, Miguel, José Luis), quienes son el sustento del edificio, además de Cyril, Pilar, Cris, Juana, Paco, Mariana, Andrew (+ ¡y muchos mas!).

De manera paralela, este viaje que llamo tesis solo se ha podido sostener gracias a todo el apoyo que he recibido desde fuera. Los que saben saben, y tener que escuchar las mismas historias y quejas sobre tu pequeña investigación, requiere de mucha paciencia y cierta abstracción. Esa se la debo a mis amigos Quevedo de vez en cuando (Juanma y Almu), compartiendo locos viajes caseros, festis y amigos invisibles, y a todos los que han estado ahí, debajo del musgo (Arturo, Belén, Carmen, Carlos, Marina) junto con Víctor, todos estos años.

Laramente no puedo dejarme a mi compañera de viaje mas cercana. Nada de esto sería posible sin tu confianza y apoyo. Eres la que mejor sabe como sostenerme y la que mejor sabe que necesito, tanto en las buenas como en las malas, aunque ni yo sea consciente. Contigo y con Bisko somos una pequeña loca familia que nadie más puede comprender (ni falta que hace).

Por último, este viaje empieza y siempre seguirá gracias al apoyo de dos padres que todo lo que me han dado es infinito cariño y libertad para convertirme en lo que yo quisiera ser. Son mis mayores valedores, ídolos y si por mi fuera, metería sus nombres entre los autores de este documento, porque esto es tan mio como vuestro (aunque aún no sepan de que va esto de los materiales). Gracias infinitas por ser mi mayor inspiración.

PUBLISHED AND SUBMITTED CONTENT

PUBLICATIONS:

- ***"Additive Manufacturing of Stainless Steel-to-Inconel Graded Material: Insights into Microstructure, Defects, and Mechanical Properties"***
  Jorge Valilla, Miguel A. Monclús, Pilar Rey, Ilchat Sabirov, Damien Tourret. Materials & Design 257, 114469 (2025).
  https://doi.org/10.1016/j.matdes.2025.114469
  This study was wholly included in Chapters 3, 4, 5 and 6. The material from this source is not singled out with typographic means and references.

- ***"Ultrafast synthesis of SiC nanowire webs by floating catalysts rationalised through in situ measurements and thermodynamic calculations"***
  Isabel Gómez-Palos, Miguel Vazquez-Pufleau, Jorge Valilla, Álvaro Ridruejo, Damien Tourret, Juan J Vilatela. Nanoscale 14, 18175-18183 (2022).
  https://doi.org/10.1039/D2NR06016G.
  This study was wholly included in Chapters 7. The material from this source is not singled out with typographic means and references.

- ***"Exploring the Impact of Configurational Entropy on the Design and Development of CoNi-Based Superalloys for Sustainable Applications"***
  Ahad Mohammadzadeh, Akbar Heidarzadeh, Hailey Becker, Jorge Valilla Robles, Alberto Meza, Manuel Avella, Miguel A Monclús, Damien Tourret, José Manuel Torralba. Journal of Alloys and Compounds 965, 171380 (2023). https://doi.org/10.1016/j.jallcom.2023.171380.
  This study was wholly included in Chapters 7. The material from this source is not singled out with typographic means and references.

CONFERENCES:

- ***"Ultrafast synthesis of SiC nanowire webs by floating catalysts"***.
  I. Gómez-Palos, M. Vazquez-Pufleau, J. Valilla, L. Arévalo, D. Tourret and J.J. Vilatela. Nanowire Week 2022. Chamonix, France; April 2022.
  (Poster presentation). https://doi.org/10.1016/j.jallcom.2023.171380.
  This study was wholly included in Chapters 7. The material from this source is not singled out with typographic means and references.

- ***"Nanowire networks formation by floating catalyst synthesis, Case of Study: Silicon Carbide Nanowires"***
  I. Gómez-Palos, M. Vazquez-Pufleau, J. Valilla, L. Arévalo, D. Tourret and J.J. Vilatela. III Congreso sobre Materiales Multifuncionales 2022. Granada, Spain; May 2022.
  (Oral presentation).
  This study was wholly included in Chapters 7. The material from this source is not singled out with typographic means and references.

- ***"Physical and Thermodynamic Simulation of Functionally Graded Materials"***
  Jorge Valilla Robles, Damien Tourret, Ilchat Sabirov. Junior Euromat 2022. Coimbra, Portugal; July 2022. (Oral presentation).
  This study was wholly included in Chapters 3, 4, 5 and 6. The material from this source is not singled out with typographic means and references.

- ***"Analysis of multicomponent alloy systems printed via Direct Energy Deposition using Thermodynamic Simulations"***
  Jorge Valilla Robles, Ilchat Sabirov, Damien Tourret. The Minerals, Metals & Materials Society (TMS) 2023. San Diego, United States of America; March 2023. (Oral presentation).
  This study was wholly included in Chapters 3, 4, 5 and 6. The material from this source is not singled out with typographic means and references.

- ***"Spark plasma sintering of novel CoNi-based high entropy superalloy"***
  Ahad Mohammadzdeh, Alessandro De Nardi, Dariusz Garbiec, Jorge Valilla Robles, Damien Tourret, José Manuel Torralba. Congreso Español Iberoamericano de Pulvimetalurgia (CEIPM202), San Sebastián, Spain; May 2023.
  (Oral presentation).
  This study was wholly included in Chapters 7. The material from this source is not singled out with typographic means and references.

- ***"Computational Thermodynamic Analysis applied to multicomponent alloy design"***

J.Valilla, A. Mohammadzadeh, I. Sabirov, J.M.Torralba, D. Tourret. Euromat 2023. Frankfurt, Germany; September 2023. (Oral presentation).
This study was wholly included in Chapters 3, 4, 5, 6 and 7. The material from this source is not singled out with typographic means and references.

- ***"Role of manufacturing routes on the microstructural features of CoNi-based high entropy superalloy"***
  A. Mohammadzadeh, Alessandro De Nardi, Amir Mostafaei, Dariusz Garbiec, Jorge Valilla Robles, Damien Tourret, Eduard Hryh, José Manuel Torralba. Alloys for Additive Manufacturing Symposium (AAMS) 2023. Madrid, Spain; 2023 (Oral presentation).
  This study was wholly included in Chapters 7. The material from this source is not singled out with typographic means and references.

- ***"Advanced Characterization of Additively Manufactured Functionally Graded Materials (FGMs) coupled with Thermodynamic Simulations"***
  Jorge Valilla Robles, Ilchat Sabirov, Damien Tourret. The European Mechanics of Materials Conferences (EMMC) 2024. Madrid, Spain; May 2024. (Oral presentation).
  This study was wholly included in Chapters 3, 4, 5 and 6. The material from this source is not singled out with typographic means and references.

- ***"Approaching the Design of AM-Functionally Graded Materials coupled with Thermodynamic Simulations"***
  Jorge Valilla, Ilchat Sabirov, Damien Tourret. Alloys for Additive Manufacturing Symposium (AAMS) 2024. Palaiseau, France; September 2024. (Poster presentation).
  This study was wholly included in Chapters 3, 4, 5 and 6. The material from this source is not singled out with typographic means and references.

- ***"Development of Functionally Graded Materials via AM: A Combined Experimental and Computational Approach"***
  Jorge Valilla Robles, Ilchat Sabirov, Damien Tourret. The Minerals, Metals & Materials Society (TMS) 2025. Las Vegas, United States of America; March 2025. (Poster presentation).
  This study was wholly included in Chapters 3, 4, 5 and 6. The material from this source is not singled out with typographic means and references.

OTHER RESEARCH MERITS

"Research stay at Colorado School of Mines" Center of Advanced Non-Ferrous Structural Alloys (CANFSA); developing and learning about advanced X-ray and neutron diffraction under the supervision of Prof. Amy Clarke; Golden, CO, United States; July-October 2023.

FUNDING ACKNOWLEDGMENTS

The research presented here was funded by the Spanish Ministry of Science and Innovation (Agencia Estatal de Investigación) — see details below. The core research project on the study of functionally graded materials was supported by the project MultiFAM. Additional activities of thermodynamic calculations were performed in support of the research within projects EARTH and DAMAS.

- **MultiFAM**: *Desarrollo de piezas 3D multi-material y multifuncionales mediante fabricación aditiva asistida por el diseño inteligente de materiales y proceso* (2020-2022). Funding programme: Programa Estatal de I+D+i Orientada a los Retos de la Sociedad. Reference: RTC2019-007129-5
- **EARTH**: *High Entropy Alloys Resistant To Hydrogen embrittlement* (2022-2024). Funding programme: Proyectos Estratégicos Orientados a la Transición Ecológica y a la Transición Digital. Reference: TED2021-130255B-C33
- **DAMAS**: *Diseño de Aleaciones Maestras para Aceros Sinterizados* (2022-2025). Funding programme: Proyectos en colaboración público-privada. Reference: CPP2021-008682

CONTENTS

LIST OF FIGURES

LIST OF TABLES

GLOSSARY

Acronym	**Definition**
AFM	Atomic Force Microscopy
AM	Additive Manufacturing
BCC	Body-Centered Cubic
BCT	Body-centred Tetragonal
BD	Build Direction
BSE	Backscatter Electron
CalPhaD	Calculation of Phase Diagrams
CSI	Crack Susceptibility Index
CTE	Coefficient of Thermal Expansion
CW	Continuous Wave
CVD	Chemical Vapor Deposition
DED	Direct Energy Deposition
DFT	Density Functional Theory
DMD	Direct Metal Deposition
DMW	Dissimilar Metal Weld
EBAM	Electron Beam Additive Manufacturing
EBSD	Electron Backscatter Diffraction
EDS/EDX	Energy-dispersive X-ray spectroscopy
FCC	Face-Centered Cubic
FGM	Functionally Graded Materials
GCP	Geometrically Close-Packed Phase
HAZ	Heat Affected Zone
HEA	High Entropy Alloy

Table 1: Recurrent acronyms used throughout this thesis.

Acronym	Definition
HEAPS	High-Entropy Alloys Predicting Software
HCP	Hexagonal Close-Packed
HMDS	Hexamethyldisilane
HPT	High-Pressure Torsion
IMDEA	Instituto Madrileño de Estudios Avanzados
IN718	Inconel 718
IPF	Inverse Pole Figure
JPL	Jet Propulsion Laboratory
LENS	Laser Engineering Net Shape
LVDT	Linear Variable Displacement Transducer
MMC	Metal Matrix Composite
PVD	Physical Vapor Deposition
QCW	Quasi-Continuous Wave
SD	Scanning Direction
SDAS	Secondary Dendritic Arm Spacing
SE	Secondary Electron
SFE	Stacking Fault Energy
SLM	Selective Laser Melting
SEM	Scanning Electron Microscopy
SS316L	AISI Stainless Steel 316L
SSIM	Structural Similarity Index Measure
STEeP	Scheil Ternary Projection
TBC	Thermal Barrier Coating
TCP	Topologically Close-Packed Phase
TEM	Transmission Electron Microscopy
UZ	Unmelted Zone
VED	Volumetric Energy Density
XCT	X-Ray Computed Tomography
XRD	X-Ray Diffraction
YAG	Yttrium Aluminum Garnet

Table 2: Recurrent acronyms used throughout this thesis.

CHAPTER 1

ABSTRACT

With the growing interest in additive manufacturing (AM) of metallic materials, several techniques have evolved up to the point of enabling new routes for manufacturing heterogeneous materials tailor-made for specific needs. That is the case of direct energy deposition (DED) manufacturing, whose features are particularly well suited for making functionally graded materials (FGMs). These materials show a gradual change in materials composition — and hence microstructures, properties, and functionalities. FGMs come as a great option when dealing with dissimilar joints or location-specific properties in a bulk part. However, FGM manufacturing is not without flaws and challenges. Apart from common AM-related defects, challenges arise, such as property mismatches or the formation of unexpected phases, which must be addressed.

This document starts by introducing a review of the state-of-the-art in AM of FGMs, addressing their challenges and most impactful case studies, describing the methods and results to date related to the specific materials in this work, and a detailed look at future perspectives. Most of the work in this dissertation falls within the scope of the national collaborative project Multi-FAM ("Development of 3D multi-material and multi-functional parts through AM assisted by intelligent material and process design") funded by the Spanish Ministry of Science and Innovation (Agencia Estatal de Investigación, Proyectos Retos-Colaboración 2019, RTC2019-007129-5). The project aimed to manufacture 3D printed multi-material parts of particular relevance to the steelmaking industry. The consortium was lead by ArcelorMittal and included AIMEN Technology Centre. IMDEA Materials contributed to the experimental and computational study of material compatibility between the selected alloy systems (AISI SS316L and Inconel 718). To do so, this work combined computational thermodynamic simulations with advanced microstructural and mechanical characterization and other exploratory experimental techniques (e.g. Gleeble physical simulation, X-ray tomography, and neutron diffraction). CalPhaD

(Calculation of Phase Diagrams) has been the primary method for thermodynamic simulations to obtain both alloy systems phase equilibrium and properties while also exploring the composition space between them. These were compared and complemented with several microstructural, mechanical, and thermal characterizations of actual printed FGMs, which were previously optimized and designed for DED manufacturing.

The latter part of the dissertation addresses several case scenarios (side projects) in which CalPhaD simulations were used to support other studies, e.g. in the scope of alloy design of High Entropy Alloys (HEAs) for hydrogen storage or high-temperature applications, and master alloys for powder sintering of steels.

CHAPTER 2

RESUMEN

Gracias al creciente interés en la fabricación aditiva (AM) de materiales metálicos y todas las ventajas que aporta, varias técnicas han evolucionado hasta el punto de habilitar nuevas vías de fabricación para necesidades cada vez más específicas. Este es el caso de la fabricación mediante deposición directa de energía (DED) que gracias a sus características, permiten la fabricación de materiales con gradiente funcional (FGMs). Este tipo de materiales presentan un cambio gradual de propiedades como la composición del material, lo que los convierte en una alternativa interesante a la hora de trabajar con uniones disímiles o para casos donde se requieren propiedades muy localizadas. Sin embargo, esta técnica arroja una nueva series de retos y dificultades. Además de los defectos ya impuestos por la fabricación aditiva, también surgen nuevos desafíos relacionados con la mezcla de diferentes materiales, tales como desajustes en las propiedades o la formación de fases inesperadas. Estos retos por tanto, deben ser abordados con detenimiento.

Este documento comienza con una revisión exhaustiva del estado del arte sobre los FGMs, abordando sus desafíos y varios casos, describiendo los métodos y resultados hasta la fecha, además de un análisis detallado de las perspectivas futuras. Gran parte del trabajo en esta tésis see da en el marco de un consorcio nacional ("Retos de Colaboración 2019") con ArcelorMittal y el Centro Tecnológico AIMEN llamado Multi-FAM ("Desarrollo de piezas 3D multimateriales y multifuncionales a través de AM asistida por el diseño inteligente de materiales y procesos"), que tiene como objetivo fabricar piezas multimateriales impresas en 3D para necesidades industriales específicas. IMDEA Materiales interviene en la selección y diseño de los materiales mediante el desarrollo de herramientas y metodologías que evaluan la compatibilidad de los materiales(AISI SS316L e Inconel 718). Para ello, este trabajo combinó simulaciones termodinámicas computacionales con caracterización microestructural y mecánica avanzada, así como otras técnicas exploratorias. CalPhaD (Cálculo de Diagramas de Fase) ha sido la principal metodología aplicada

para las simulaciones termodinámicas, con el fin de obtener información sobre las fases en equilibrio y propiedades de ambas alaciones, siendo además capaces de explorar el espacio composicional entre ellos. Para validar estas simulaciones, se compararon y complementaron con caracterización microestructurales, mecánicas y térmicas de FGMs ya impresos, que previamente fueron optimizados y diseñados para la fabricación mediante DED.

La última parte del documento aborda diferentes casos see aplica la metodología CalPhaD en busca de mejorar el diseño de aleaciones de alta entropía (HEAs) para diferentes aplicaciones como almacenamiento de hidrógeno o aplicaciones a alta temperatura, así como aleaciones maestras de acero para la sinterización de polvos.

CHAPTER 3

INTRODUCTION & STATE OF THE ART

3.1. Motivation & Objectives

Despite the established role of metallic materials in modern society, there are still plenty of challenges in which material science and, more precisely, physical metallurgy can develop tailored solutions that suit many specific applications. In many cases, industrial parts not only require different properties, but these properties are also specifically required with geometrical constraints, making the engineering more challenging. Since most engineering materials were manufactured aiming for homogeneous characteristics [144], joining techniques such as welding are a typical, economical, and efficient way to combine metals permanently [41] and obtain different properties within the same part. Unfortunately, most of these traditional joining techniques lead to sharp gradients in composition, which lead to abrupt gradients in properties that can promote failure mechanisms. [138].

Nevertheless, it is still necessary to find more specific solutions for particular industries where a graded transition of properties is beneficial [56], such as aerospace [5], biomedical [111, 133], nuclear, automobile, or defense [103]. This is why the use of and research on functionally graded materials (FGMs) has increased in recent years alongside major advances in additive manufacturing (AM)[72]. FGMs represent a family of materials in which compositions (and therefore constituents and/or the microstructure itself) gradually change alongside the spatial directions. This results in a gradual change in properties (such as mechanical, thermal, chemical, or its cost) that can be fine-tuned for specific applications [190]. An example of a specific application can be found in Figure 3.1, where an FGM solution is applied to alleviate the drawbacks of some traditional dissimilar joints between two alloys for a nuclear application [171]. Yet, these novel materials and manufacturing routes do not come without drawbacks, which will be addressed in the following chapters.

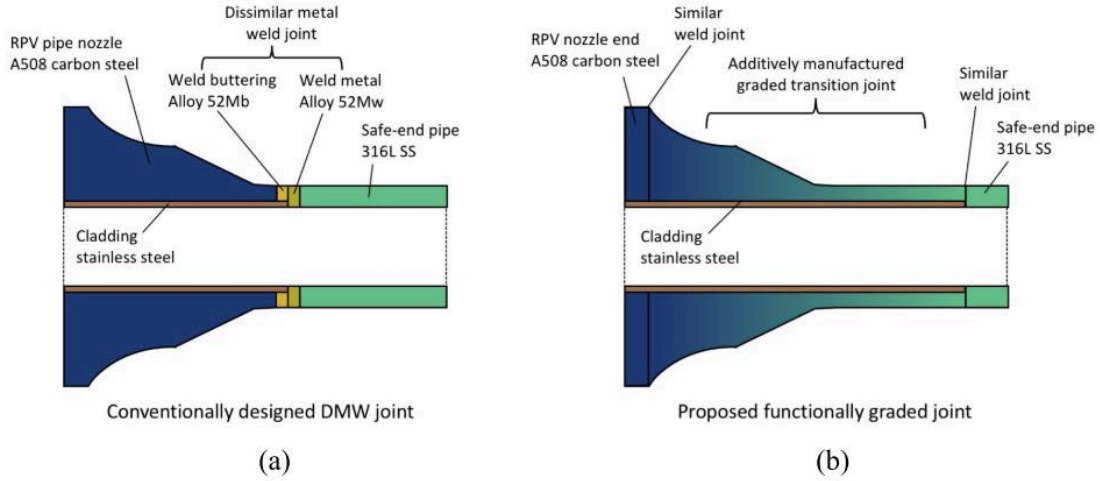

Figure 3.1: (a) Cross section of a dissimilar weld joining (carbon steel nozzle with austenitic stainless steel). (b) Solution using functionally graded joints [171].

Most of this thesis is part of a larger collaborative project called Multi-FAM, coordinated by steel manufacturer ArcelorMittal, together with AIMEN Technology Centre, and IMDEA Materials. This collaborative project aims to manufacture 3D-printed multi-material structures for the steelmaking industry, and to provide further insight into novel tools for intelligent thermodynamic simulations and material characterization. A key objective is to establish a methodology for the design and manufacture of FGM structures not only for purely academic purposes but also to be applied in industrial sites.

The demonstrator proposed for this study is a 300 mm diameter gas injection nozzle used for manufacturing steel (Figure 3.2), traditionally made from GG20 carbon steel or tool steels. This gives the part excellent impact resistance, but the wear and tear (Figure 3.3) due to the working conditions (namely, working in close contact with melted metal at high temperature) requires quick replacements. This wear is related to high-temperature fatigue cycles that sometimes lead to fracture. For that reason, using a FGM that combines excellent behavior at high temperatures (especially fatigue) on the surface and good tenacity (and more cost-efficient) alloy on the inside could be an optimal solution.

Beyond this study, in addition to a thorough characterization (microstructural, mechanical, and computational) of graded samples, we aimed to gain further insight into the capabilities of the CalPhaD method for other applications related to advanced alloy design and material selection for other technological applications. Hence, while the core of this thesis focuses on the analysis of FGMs, the latter Chapter 7 describes the use of CalPhaD in other contexts — for instance the design of Hydrogen-embrittlement-resistant high-entropy alloys, or master alloys for sintered steels.

Figure 3.2: Design of the current part [9].

Figure 3.3: Example of the damage of a gas injection nozzle [9].

3.2. State of the art

3.2.1. Additive manufacturing

Although FGMs can be manufactured through many techniques, such as chemical (CVD) and physical (PVD) vapor deposition, among other techniques [144], additive manufacturing is becoming one of the most relevant. AM refers to a growing range of processing techniques that consists of progressively adding material, which usually comes as a powder or wire feedstock, layer by layer until manufacturing the final part [88]. The process parameters (e.g. heat source power and speed, path planning, etc.) are directly inferred and calibrated from a digital model of the bulk material to be manufactured. This allows manufacturing complex geometries unattainable by other traditional techniques, while reducing material waste. This also leads to fewer post-processing steps, a booster for sectors such as medical and aerospace [46]. Traditionally, AM techniques have been mainly deployed to build (macroscopically) homogeneous parts, with powder bed techniques like Laser Powder Bed Fusion (LPBF, see Figure 3.4) being one of the most common [47]. When dealing with gradients that involve changes in composition, precise control of feed-

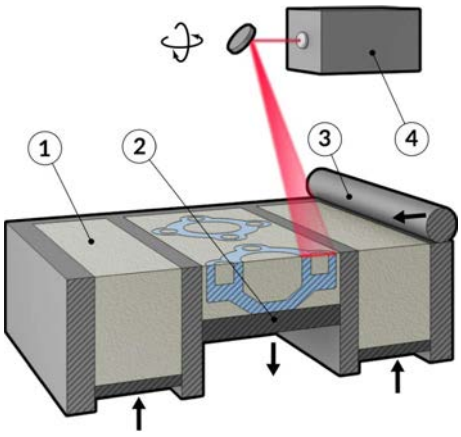

Figure 3.4: Sketch of an SLM/SLS setup. 1-Metal Powder; 2-Building platform; 3-Roller; 4-Laser [2].

stock material and the ability to change it mid-build is necessary. One viable option would be premixing the feedstock powders [61], but that would not be efficient regarding waste reduction [138]. Therefore, other techniques, such as Direct Energy Deposition (DED), appear more suitable.

Direct Energy Deposition (DED)

In DED techniques, such as LB (laser beam), EB (electron beam), and DED-Arc [49, 106, 141], the feedstock material (either powder or wire) is pushed or blown to be melted directly by a focused energy source — for example, a laser beam, an electron beam, or an electrical arc — as it is being deposited (as detailed in Fig. 3.5) The deposition head is commonly mounted on a mobile system, e.g. a robot arm, to raster a specific area with a predefined deposition pattern to create a part layer by layer from a computer-aided design (CAD) file.

Blown-powder DED systems allow for multiple feedstock sources, which can be interchangeable or mixed powders from various hoppers in controlled quantities (in a setup similar to Fig. 3.6). Another benefit of DED is the deposition rate and the larger size of the manufactured parts, while conversely losing some geometric accuracy (higher layer thickness and lower resolution) [3]. Consequently, DED is commonly used for manufacturing large parts, to deposit directly onto existing

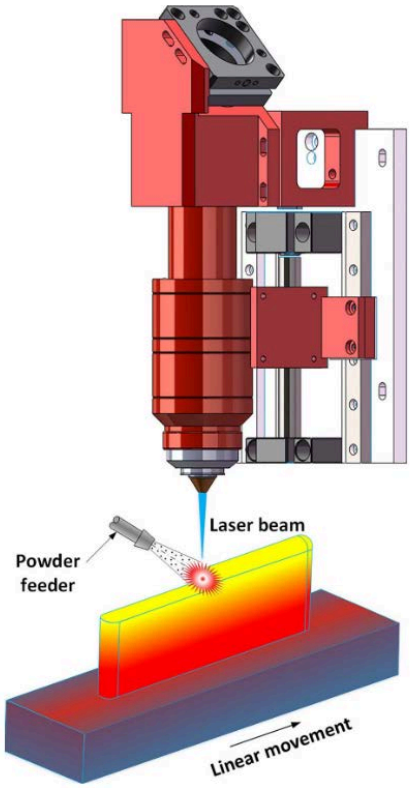

Figure 3.5: Sketch of a DED setup [100].

components to add feature or repair [139] and to change the chemical compositions within a part to produce functionally graded materials. For these reasons, DED is an interesting alternative in terms of versatility and overall manufacturing costs compared to similar techniques in the market (Fig. 3.7).

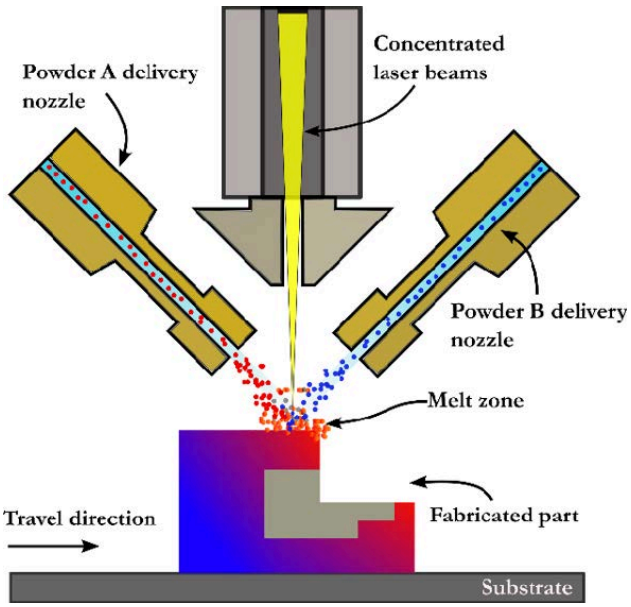

Figure 3.6: Sketch of a DED set-up utilizing a multi-material configuration(Adapted from [169]).

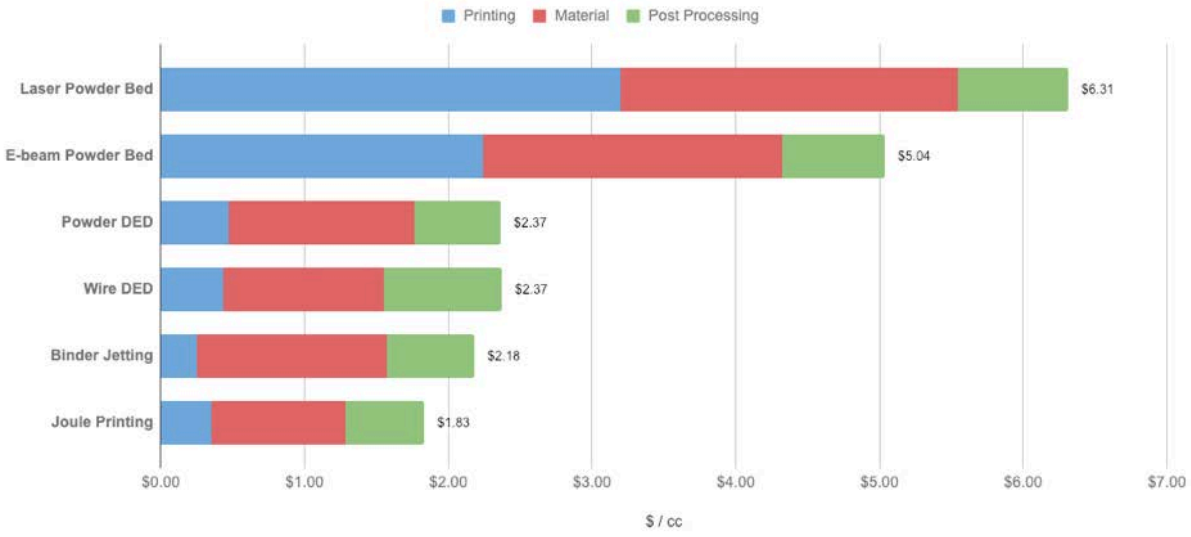

Figure 3.7: Additive Manufacturing for Titanium (Dollars) Per Cubic Centimeter [73].

Process parameters:

As illustrated in Fig. 3.8, several parameters must be controlled to obtain the best deposition and, consequently, the best part quality and desired geometry. Apart from the feedstock material and the alloy design (that will both be discussed in further segments), the manufacturing system allows for a certain freedom regarding process parameters that must be adjusted depending on each application. A study in [137] shows the key parameters related to the deposition process as follows:

- **Laser parameters**: Laser power changes the working temperature, the melt pool size, the cooling rate, and the ability to melt or remelt. This causes vast defects and microstructure variation if the energy source is too high (lower cooling rate with coarser microstructure and columnar grains) or too low (higher cooling rates and equiaxed grains). Laser wavelength determines the amount of energy absorbed by the material. The spot size/focal offset distance controls energy density and melt pool size, which increases the amount of powder melted (higher build rate but higher surface roughness and less resolution) [137].

- **Scan parameters**: Scan speed is related to the energy density absorbed by the material, thus influencing several parameters (cooling rates, microstructures, lack of fusion). Hatch width (distance between two consecutive scanning lines within the same layer) must not be too high (lack of fusion) nor too low (in situ heat treatment effects). Idle time between layers controls temperature gradients and, consequently, microstructure. Layer thickness is also essential (key for geometric accuracy and heat dissipation) [137].

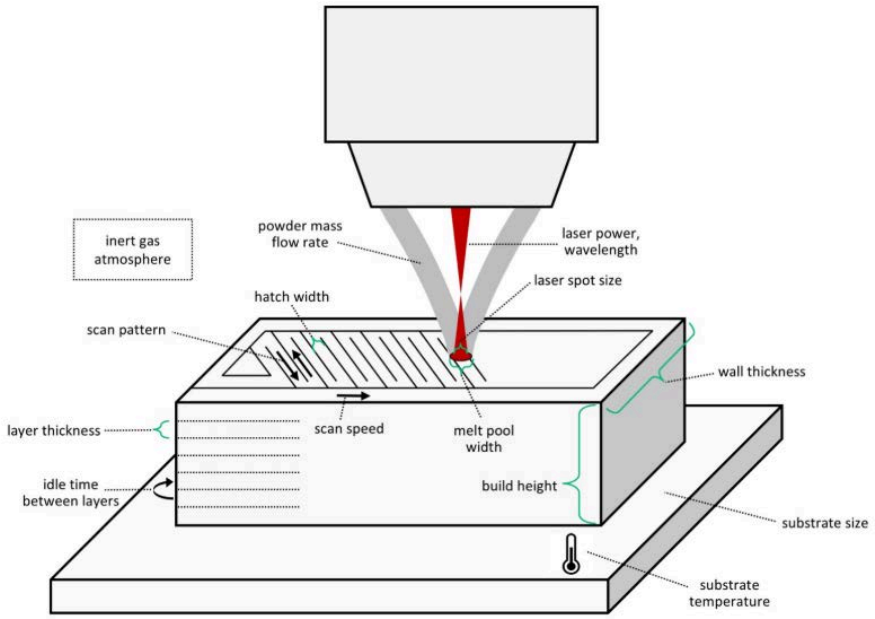

Figure 3.8: Sketch showcasing some of the most relevant process parameters [137].

- **Other parameters**: The feed rate controls the mass flow, determining the layer uniformity and height. High rates require higher amounts of energy to melt the substrate, which can cause poor layer adherence, while slower rates can cause overheating and, thus, underbuilding and less geometrical accuracy. Substrate temperature and size, which influence the cooling rate and the building atmosphere, are also relevant. Using an inert and controlled atmosphere will prevent the formation of oxides, impurities, and inclusions and improve layer adherence and wettability [137].

3.2.2. Feedstock material

DED can be used with both wire or powder feedstock. Wire enables faster deposition rates [11], better material utilization [1, 162], lower cost and more accessible. In contrast, powder allows for better resolution (saving costs since less postprocessing is needed at the end) and is most appropriate for progressive grading, i.e. in situ mixing of different powder feedstock. In this study, the primary feedstock material in use was powder.

Powder-based material must be controlled to obtain a clean and accurate deposition and the desired microstructure. One of the most critical parameters is particle size. Ideally, a finer powder size is better for focusing the stream to a precise point and obtaining a higher resolution. Still, extremely small particle size can lead to inefficient flowability (due to agglomeration and formation of clusters) that leads to uneven spreading [89]. Therefore, a balance between coarser (⌀: 90-120 µm) and small (⌀: 0.1-5 µm) particle sizes must be achieved.

Particle sphericity is another parameter to obtain good flowability and ensure uniform deposited powder, where closer to sphere-like geometry allows for a better spreading and uniform deposited layer (good packing). Conversely, irregular shapes tend to cause friction and interlocking. Differences between material morphology can be seen in Fig. 3.9. A way to characterize the three-dimensional shape of the particles is by using X-ray computed tomography [153]. To check for good flowability, the powder must exhibit close to laminar-like fluid flow (resembling fine sand) instead of chaotic breaking and cleaving (like baking flour) [11]. Some studies [116] suggest that a combination of small and larger particles (in a bimodal or even trimodal distribution as seen in Fig. 3.10) is the best suited for additive manufacturing, increasing the powder density by about 30% if the amount of fine particles reaches 30%. It is essential not to have many small particles so they do not agglomerate and stop filling the voids between bigger particles, as seen in Fig. 3.11. This distribution is controlled by sieving particles by size.

In regards to powder flow and the melting pool created when melting the powder, it has been brought to light [8, 130] how surface tension (through the Marangoni effect) can cause intense fluid flow where new powder is mixed with remelted layers,

contributing to undesired and uncontrolled mixing.

Powder chemistry is also crucial to controlling element segregation and impurity levels. It is extremely important, especially for highly reactive materials like titanium or aluminum, to be aware of oxygen, nitrogen, and hydrogen contents since these could lead to brittleness and formation of undesirable phases [19, 184].

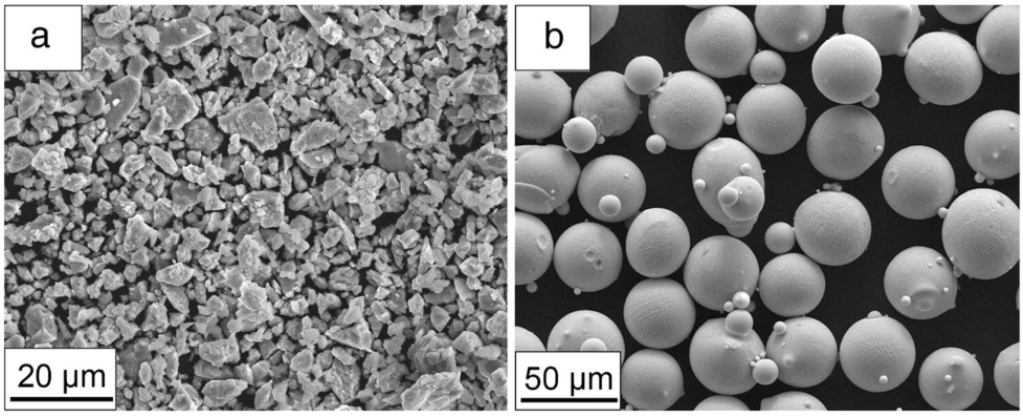

Figure 3.9: SEM images of (a) as-milled amorphous Al alloy powder (b) HEA (High Entropy Alloys) gas-atomized particles [166].

As expected, the nature of the feedstock material is at least as critical to the process as the process itself. The importance of the characteristics described below [137] will be extensively discussed in following chapters. Still, as a matter of brief introduction, it is important to consider the following properties when choosing building materials:

- **Melting temperature and melting range:** This is related to the amount of energy input needed and, in the case of a wide melting range (big gap between solidus and liquidus temperature), propensity to suffer microsegregation, heterogeneous microstructure, and properties, as well as solidification cracking.

- **Laser absorptivity:** If the material reflects most of the laser energy instead of absorbing it, it will be challenging to deposit, requiring even higher energy inputs and/or slower building speeds (see Fig. 3.12).

- **Thermal conductivity:** If too high, heat will dissipate from the melt pool quicker, leading to poor layer-to-layer consolidation and adherence.

- **Coefficient of thermal expansion:** Taking into account the high cooling rates present in the process, the larger the CTE, the larger the contraction during the melting process; thus, there is a higher probability of thermal stresses and thermal distortion that can lead to failure.

- **Solid state phase transformations:** These types of transformations during the cooling process can lead to volumetric changes that can cause stresses.

- **Oxidation properties:** The formation of oxides leads to not only poor me-

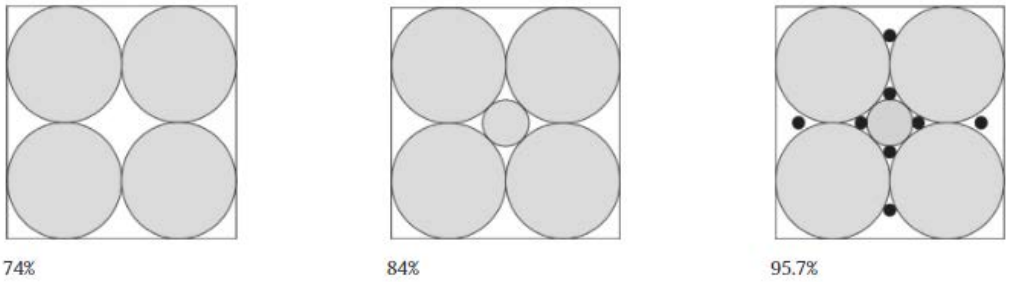

Figure 3.10: Packing arrangement and density of different distribution models [195].

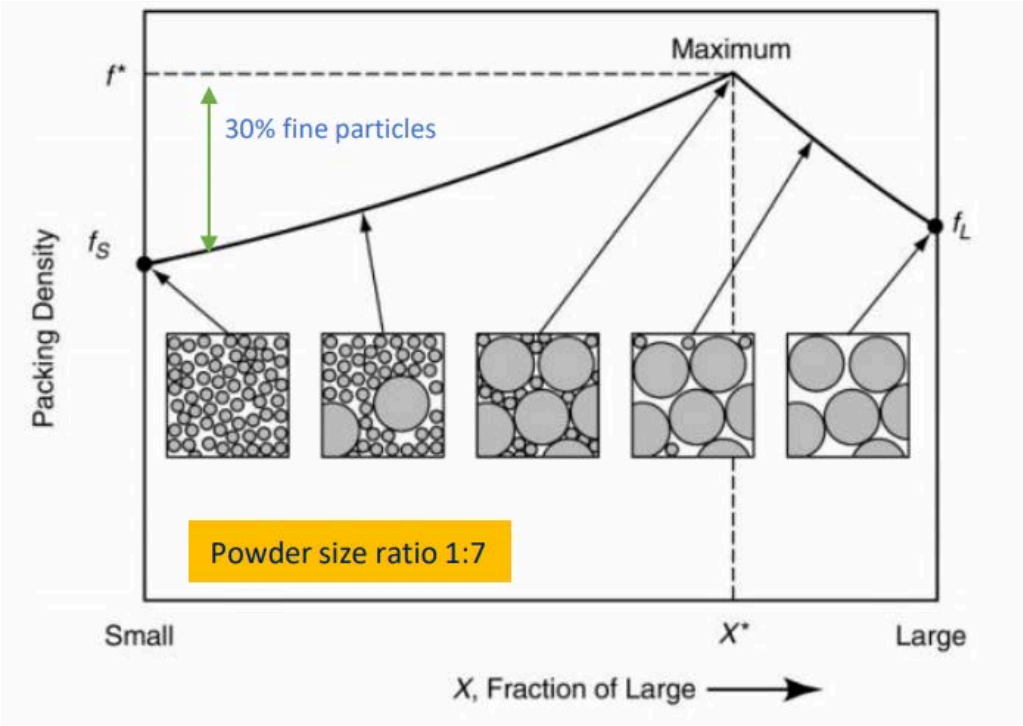

Figure 3.11: Ideal of the size distribution of particles related to their packing density [116].

chanical properties and undesired microstructure but also poor adherence in the substrate for the following layers.

3.2.3. Solidification and microstructure evolution

Materials under additive manufacturing processes can suffer rapid and very focused solidification conditions since a significant amount of energy input is concentrated into a small molten pool. These rapid solidification mechanisms lead to insufficient diffusion time, leading to compositional heterogeneities, with some phases unable to reach equilibrium compositions [137]. This leads to unexpected microstructures and properties that rely heavily on cooling rates.

Two variables are commonly used to further explain the influence of solidification

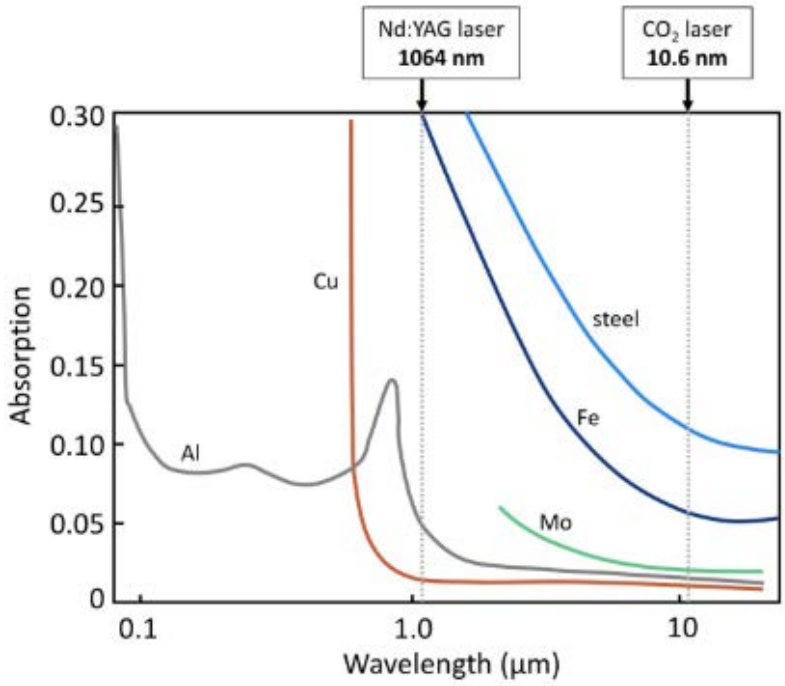

Figure 3.12: Absorption of incident laser energy for different metals. Redrawn by [137] based on [80].

in the final structure: G (Thermal gradient, °C/mm) and R (solidification rate, mm/s), which can also be defined as the solid/liquid interface velocity. The product (GR) is the cooling rate (°C/s) [53]. The influence of these variables upon the resulting microstructure is depicted in Fig. 3.13. The solid/liquid interface tends to be planar when the solidification rate is slow. On the other hand, if the solidification rate is higher but still shows a low thermal gradient, equiaxed dendrites will appear as the solidification structure. The cooling rate (GR) determines the overall scale and nature of the solidification microstructure (the higher the cooling rate, the finer the microstructure). This comes as a result of lower diffusion length L with an increase of solification rate.

$$L = \frac{D}{R} \tag{3.1}$$

with D the solute diffusivity.

Due to the rapid cooling inherent to the process ($10^3 - 10^6$ °C/s [7]), laser-deposited alloys tend to form fine structures (cellular/dendritic), which enhances mechanical properties but at the same time also enhances microsegregation, which is not considered in equilibrium solidification [137]. A prime example is interdendritic segregation, which leads to the precipitation of potentially detrimental secondary phases that not only enhance brittleness because of their incoherent crystallographic structure but also deplete the matrix composition in potential strengthening species. This phenomenon is difficult to prevent and requires a heat treatment to correct and reverse, even though signs of the initial melt pool boundaries will still be present.

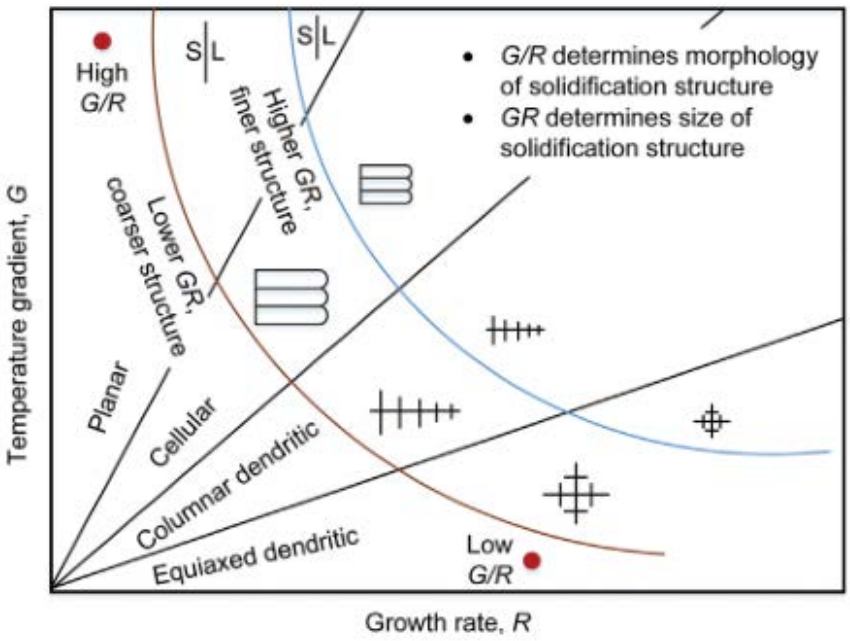

Figure 3.13: Thermal gradient G, the growth rate R, and the possible solidification microstructures [10].

Upon each new deposition, not only is there a new melt pool, but there is also some remelting and remixing from the previously deposited layer, which helps consolidate the macroscopic structure but also generates a complex and less predictable thermal history (Fig. 3.14). Each layer acts as a nucleation site for the next one, creating a macroscopic columnar structure in the build direction (since this direction has greater temperature gradients and heat conduction [137]) with clear boundaries formed by the meltpools (Fig. 3.15). The larger the heat output, the more remarkable the columnar structure, which leads to a defined material texture and anisotropic properties [66]. A good example is when analyzing specific properties across the building height. After knowing the thermal history, it is expected that as more layers are deposited, heat accumulates and thermal gradients decrease. When studying these effects in SS 316L [6], it could be seen that the first layers show higher hardness due to the rapid cooling rates and finer grain structure than in progressive layers, which exhibit larger grain sizes. Conversely, when studying this effect with alloys that show martensitic transformation [172], the continuous reheating tempers the martensite and thus reduces the hardness values from the initial layers.

3.2.4. Functionally graded materials (FGMs)

FGMs are a class of materials that exhibit a smooth and progressive gradient in the nature of the material (like its microstructure or composition), typically graded from one relatively well-known material to another [81]. Bulk parts with gradients in composition can thus achieve gradients in microstructure and properties.

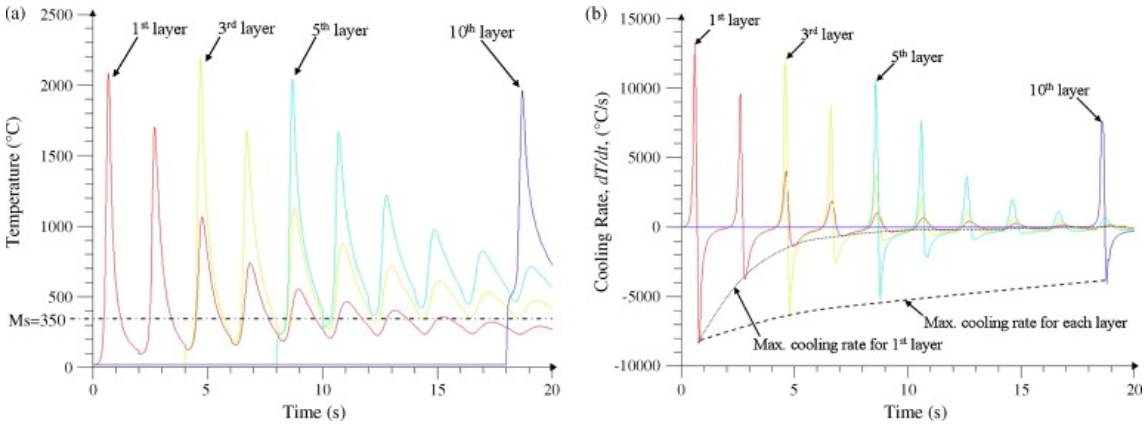

Figure 3.14: (a) Thermal cycles and (b) cooling rates as a function of time for different layers in a laser deposited alloy [172].

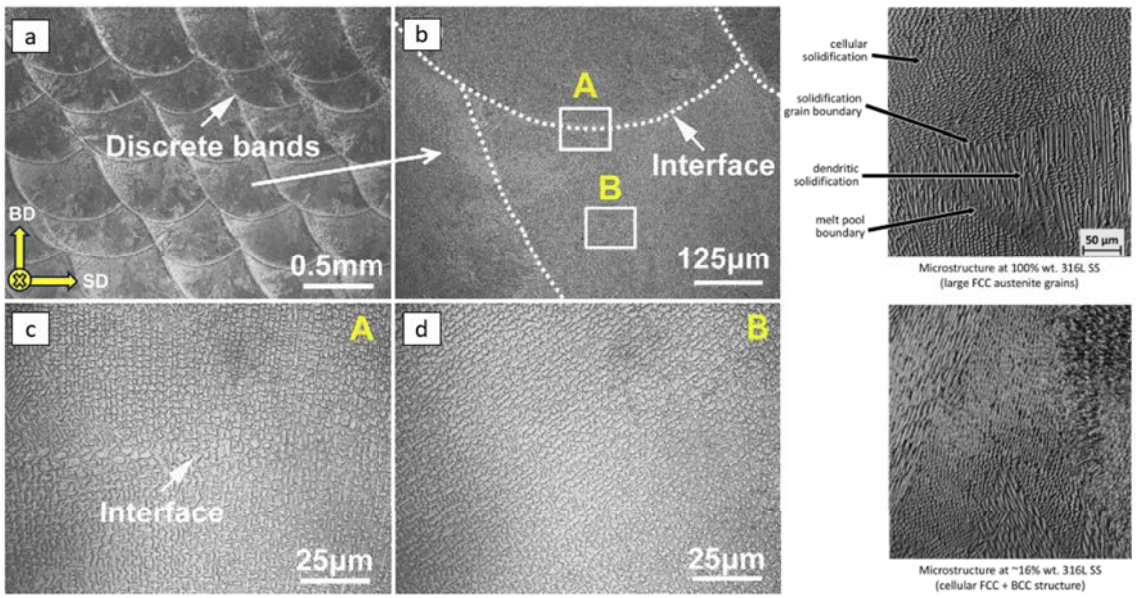

Figure 3.15: Micrographs of a longitudinal cross-section of Inconel 718 samples, showing the grain boundaries and submicron structure. BD: build direction; SD: scanning direction [181] (left). Microstructure of 316L SS that show both the internal structure and the melt pool boundaries [18] (right).

The intermediate gradient zone avoids sharp transitions that can cause a multitude of issues (like hot cracking and creep-related defects [58]), extensively reported in welding [112], where the use of Dissimilar Metal Welds (DMWs) has been a solution but not without its limitations [58]. FGMs have been studied in multiple materials such as polymers (early 1970s [124]) and in various fields like biotechnology [11] and biomedicine [133]. They can be seen in nature [38], for instance, considering bone structure or the transverse structure of plants.

Regarding bulk metallic materials, one of the first implementations of this technology was as a functional solution for thermal barrier coatings for the Japanese space shuttle project in 1983 [124]. This solution was meant to reduce the thermal stress related to the metal and ceramic interfaces. In recent years, the interest in FGMs has grown in several industrial sectors [57, 99] because of the potential of tailoring gradients to specific needs.

Figure 3.16 shows how properties follow a similar trend by smoothly transitioning from one material to the other, aiming for a monotonic behavior.

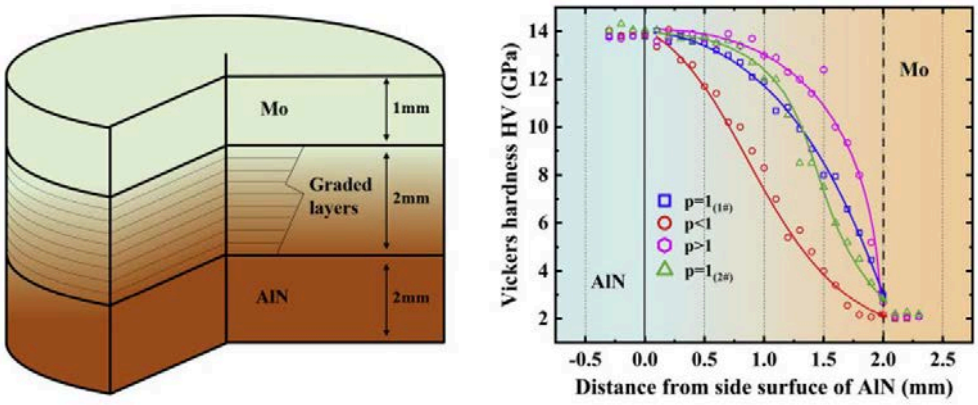

Figure 3.16: FGM structure (AlN to Mo) and its variation of Vickers hardness along the gradient[39].

Among important milestones in the advances of FGM AM, work at NASA's Jet Propulsion Laboratory (JPL) has shown how different implementations of the DED technique can produce different types of FGMs [72]. A rotating mechanism attached to the substrate rod in place while depositing the material can create a radially graded structure, as shown in Fig. 3.17. The materials in use are both iron-based alloys, but they have specific properties that differ from one to the other. The stainless steel 304L is a cheaper structural support, while the outer material (Invar 36) gives the rod minimal thermal expansion. In this case, the final application for a similar rod is as an insert for a spacecraft panel (Fig. 3.18).

Other interesting research from JPL [71] focused on the manufacturing of rocket nozzles from refractory metals and lightweight alloys (Fig. 3.19), or the implementation of strengthening solutions for lightweight alloys. In this case, titanium alloys and TiC are used to create MMC (metal matrix composites), taking into account the

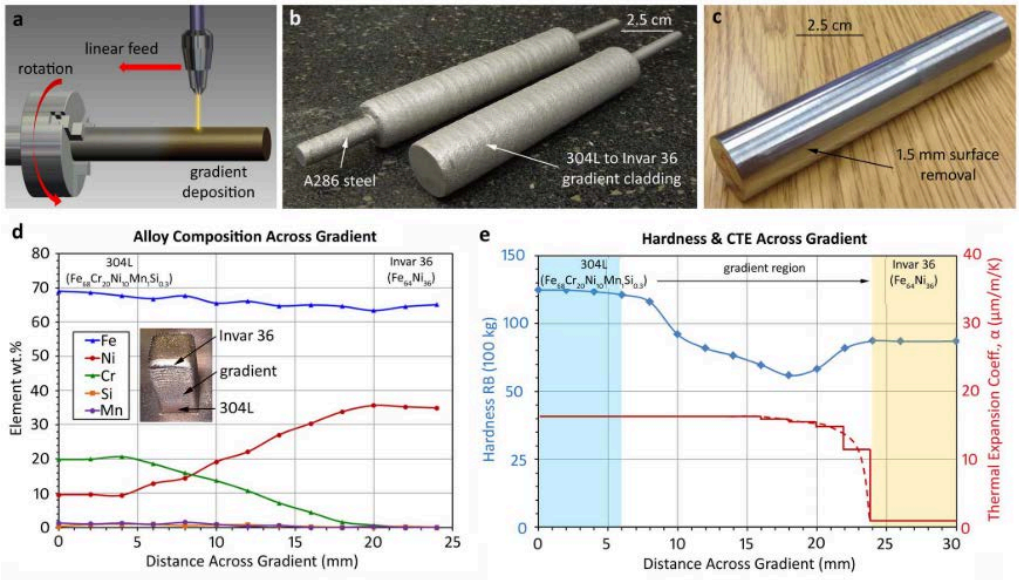

Figure 3.17: (a) Rotational deposition process. (b) Radially graded alloys where 304 L to Invar 36 gradient was applied to a rotating A286 stainless steel rod. (c) Final rod part after a 1.5mm surface removal (d) Variation of each element alongside the composition gradient. (e) Change in hardness and CTE alongside the gradient. [72]

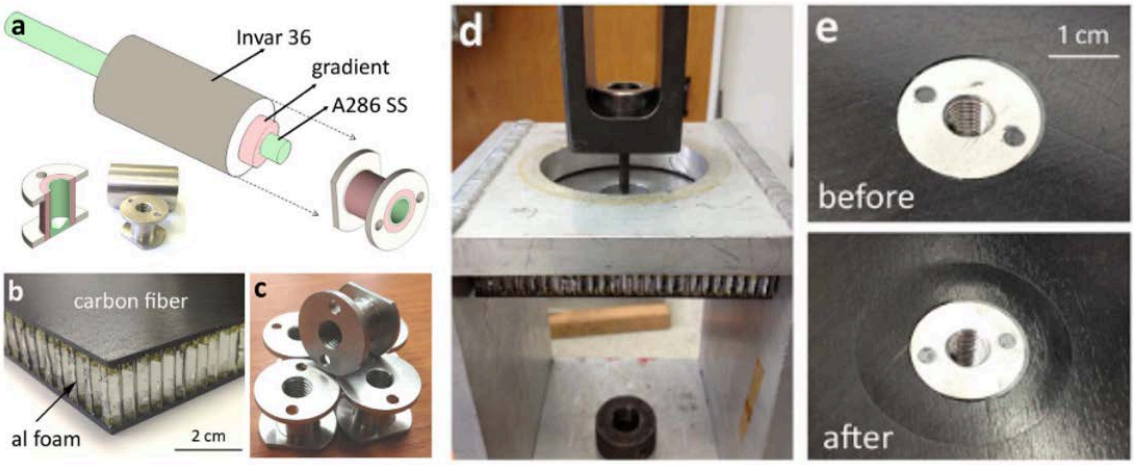

Figure 3.18: (a) Schematic of the graded rod (b) Carbon fiber/aluminum foam structure. (c) Inserts. (d) Pull-out testing for the low-temperature cycled inserts. (e) Before and after images of the insert pull-out tests show deformation in the carbon fiber panel. [72]

difference in density and melting temperatures of the metal and ceramic particles by controlling the volume fraction of both during deposition (Fig. 3.20).

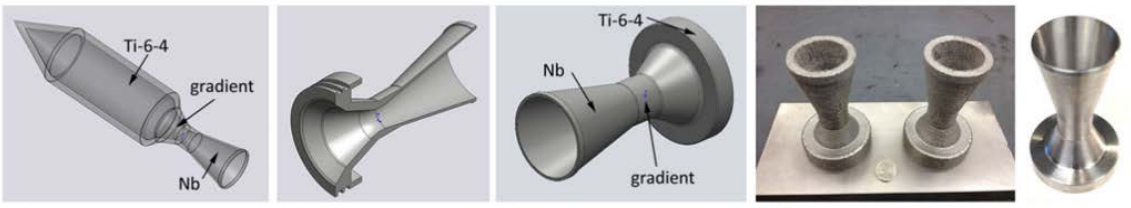

Figure 3.19: Prototyping of the desired part and the location of each material (Nb and Ti-alloy respectively) depending on the properties required [71].

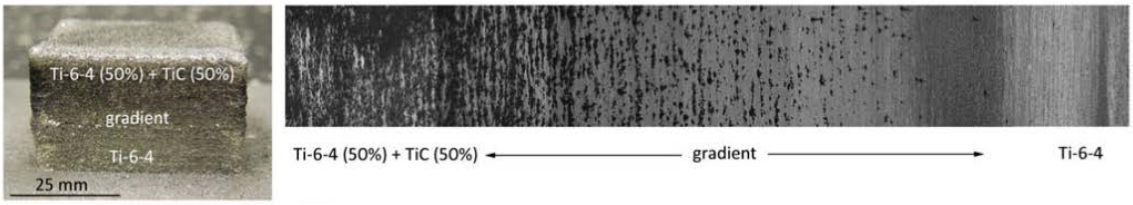

Figure 3.20: Image of the final material gradient and micrographs that show the difference between the TiC particles (in black) and the Ti-alloy matrix [71].

3.2.5. Computational thermodynamics

Computational thermodynamics methods, such as CalPhaD (Calculation of Phase Diagram), stand as a powerful tool to study equilibrium states and expected phase transformations in complex alloys — and even more so in mixtures of complex multicomponent alloys.

The CalPhaD method

This approach, initially considered back in the 1970s [158] is based on the compound energy formalism [37, 54] that consists of analyzing the Gibbs energy of each phase in a system (as a function of temperature, composition, and/or other thermodynamic variables of interest) to obtain quantitative predictions of phase equilibrium for a desired set of conditions [72] in complex multicomponent systems. The initial data is extracted from empirical and theoretical data, which are collected in databases [22]. The result of this computational approach can lead to the construction of arbitrary phase diagrams and other types of data layouts, which are great tools for predicting expected phases to be established under certain conditions [113]. We can utilize phase diagrams as a first-order approach, which gives a route map of under what conditions certain phases appear in a binary, ternary, or higher-order system of selected elements.

When designing simulations applying CalPhaD, the way of work follows a simple yet strict flow, depicted in Fig. 3.21. As described before, we first need to select an appropriate database that contains all of the elements present in our system. This database will contain different thermodynamic data from different families of elements (Fe-based, Ni-based, Al-based, etc.), how they interact with each other, and which phases can form at different thermodynamic conditions. Once the database and the element are selected, we can filter the number of possible phases, making our system manageable for the computation. Finally, we must fulfill all degrees of freedom of the system by imposing different conditions, such as temperature, pressure, volume, composition, etc., enabling the calculation of Gibbs polynomial functions for each combination. Finally, we will apply compound energy formalism, which compares all of these Gibbs energies, looking to minimize them as much as possible in the system, resulting in the election of specific phases, their compositions, and their resulting fractions.

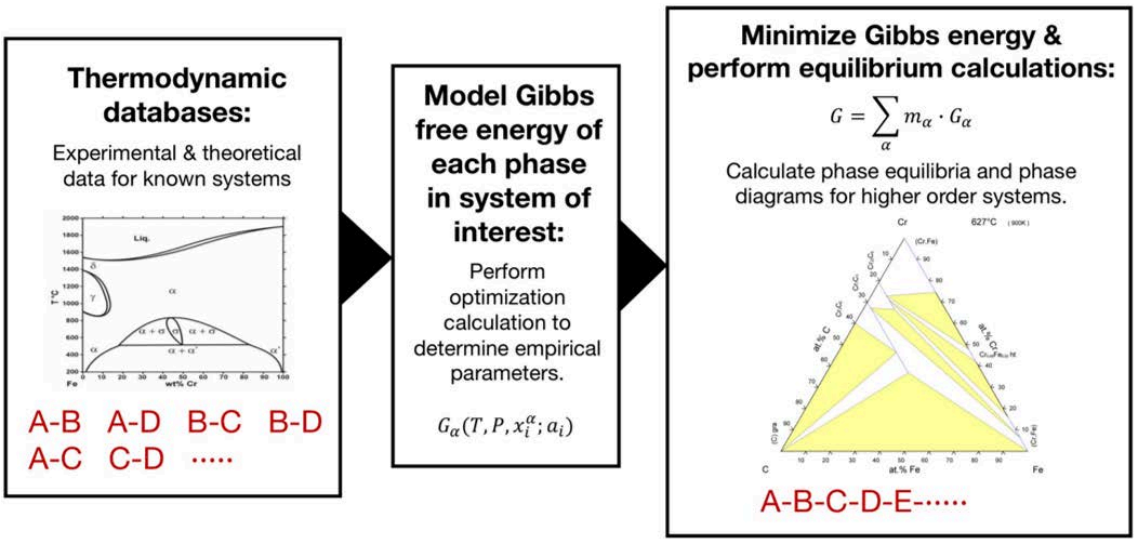

Figure 3.21: Schematic of how CalPhaD methodology is applied [137].

Even though laser deposition may lead to a non-equilibrium process, the analysis of equilibria at given compositions and temperatures can be extremely useful to anticipate the formation of phases when compared to real experiments [21, 22, 23, 26, 37, 138]. Equilibrium phase diagram calculations may even be used to design complex composition paths within a multicomponent phase diagrams using multiple feeders, e.g. to avoid entering a region containing a known undesirable phase [85, 86].

Studies in the literature have found that a Gulliver-Scheil model, in spite of its restrictive assumptions (no solid diffusion and full equilibrium in the liquid phase and at the interface), was often reliable to predict the resulting phases in DED-printed FGMs (see, e.g., [24, 26]). These results support the fact that the kinetic departure from equilibrium of the interface (e.g. solute trapping, kinetic undercool-

ing) is limited under DED-relevant conditions. Still, some discrepancies were also noted on the presence of certain phases (e.g., C14 [23], σ [22], or BCC [20] phases). Moreover, even when all phases are properly predicted by CalPhaD, small deviations in composition or temperature ranges may exist compared to experimentally measured values [21]. Nevertheless, the method remains extremely valuable to explore greatly multicomponent alloy space. Therefore, here we use CalPhaD as a tool to rationalize experimental observations rather than a fully quantitative prediction tool.

Application to Functionally Graded Materials

There have been several works applying the CalPhaD method to the study of FGMs [20, 21, 22, 23, 25, 26, 27, 50, 76, 77, 85, 98, 107, 165, 189]. Ternary phase diagrams are a great initial roadmap to design an optimal gradient path from the starting and ending point of the part alloy composition (Fig. 3.22). Choosing a convenient range of temperatures is necessary to obtain a representative ternary diagram. It is useful to choose a range where the kinetics of a phase transformation of interest start to slow down or stop [37]. The main limitation is that only a few elements are considered, which is the most representative of the case study. Conversely, as described in previous chapters, some minor alloying elements like Nb, Mn, and Mo can be critical in forming several phases.

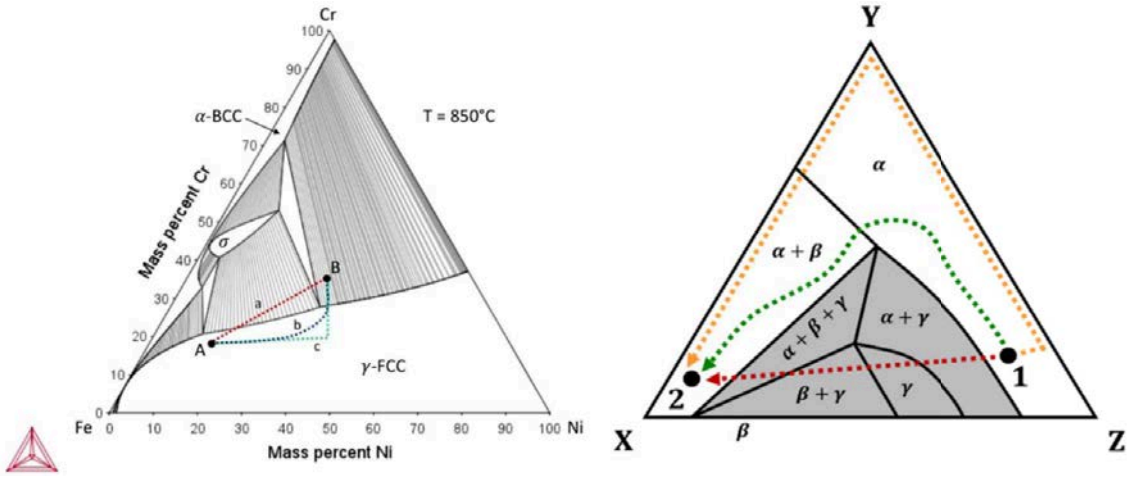

Figure 3.22: Gradient paths in both a real Fe-Cr-Ni system obtained using the Thermo-Calc TCFE7 database [18] and a sketch of a phase diagram [50]. Both diagrams show multiple routes to reach an endpoint and how some undesired phases appear depending on the path.

Obtaining an optimal gradient path is critical to avoid undesired phase formation or regions of insolubility. The work of [50, 86] shows a promising path planning optimization strategy based on machine learning robot path algorithms alongside CalPhaD data. Different criteria can be addressed to extensively design the path

(minimum path length or that better prevents undesired phase areas). Despite this being a very interesting technique, this option was out of the scope of this thesis since we could not move in the tridimensional space of the diagram, which requires at least three powder tanks, while only two tanks (one for each alloy) were used in our case.

Novel Gulliver-Scheil assumptions can also be interesting to apply to FGMs, as the work in [123] shows the creation of Scheil ternary projection (STeP) diagrams, which are generated by mapping Scheil calculations over the composition space to find nonequilibrium phases and microstructures (Fig. 3.23). These diagrams show more appearance of intermetallic phases than equilibrium diagrams and only show if a phase is or is not present (and not its composition or phase fraction), as well as not being able to account for solid-state transformations.

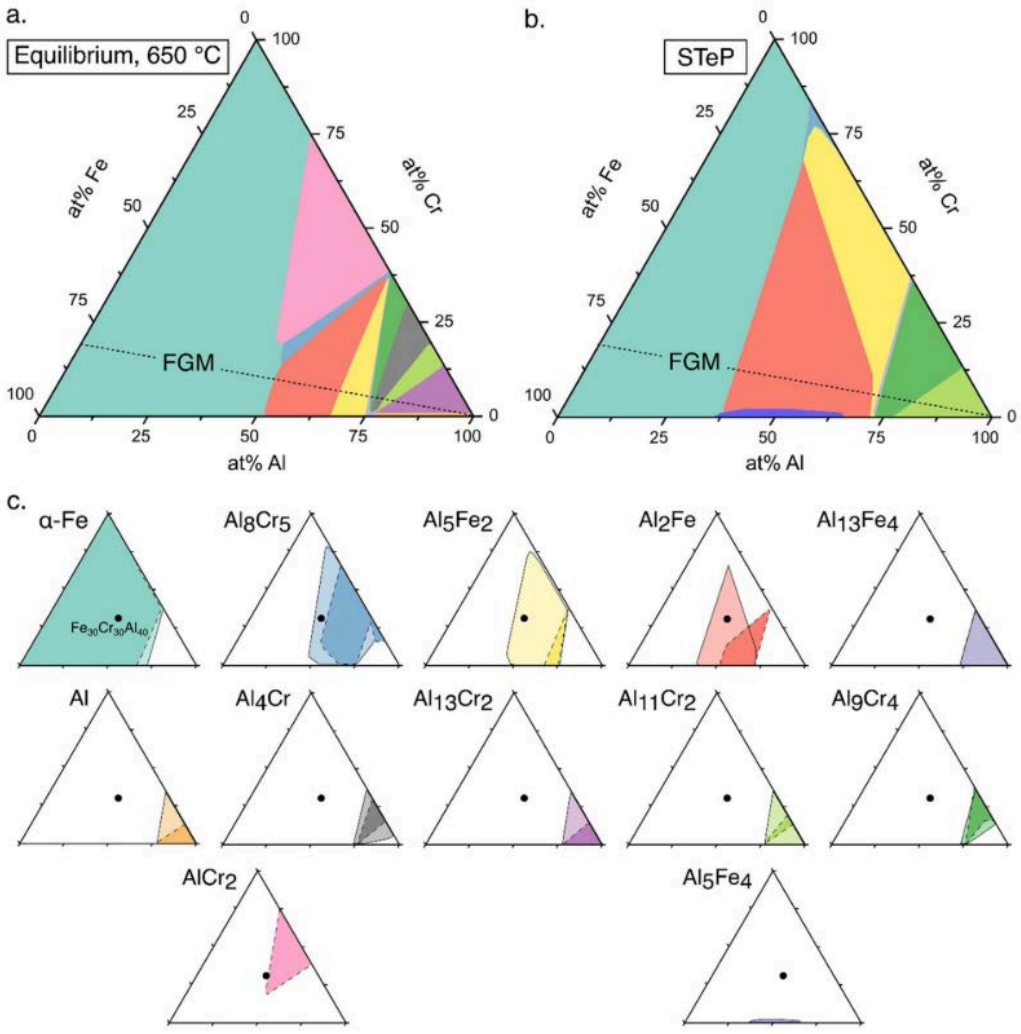

Figure 3.23: (a) Equilibrium Fe-Cr-Al ternary diagram (b) Fe-Cr-Al STeP diagram.(c) Overlapped diagrams (equilibrium and STeP from the different phases.[123]

3.3. Main challenges

As seen in previous chapters, FGMs stand as a promising solution for specific technical needs. In order to successfully manufacture and establish a way of working with them, there are some obstacles to overcome since simply joining two random alloy systems together does not work smoothly in the vast majority of cases. Finding a way to overcome these challenges differentiates conceptualization and application. It is for these challenges that a design methodology must be explored to find the most suitable solutions.

3.3.1. Thermal mismatch

Since DED is fusion-based, the melting temperature across the material grading is one of the first properties to check. Materials with significant differences in melting temperatures (Table 3.1) tend not to be compatible [138] and may lead to the appearance of dilution and cracks in the lower melting alloy [79]. For this purpose, it is common to use trimetallic joints [58] or intermediate materials [23], which mitigate the significant difference in thermal properties by adding another alloy with intermediate properties. Issues can also appear when big drops in melting temperature cause overflow and formation of liquid in the gradient [21].

Table 3.1: Melting temperatures of commonly used metals and alloys (from [138])

Material	T_m (°C)	CTE (10^{-6}/°C)
Magnesium	650	26
Aluminum	660	22.9 - 23.6
Bronze	913	17.5 - 18
Brass	927	18 - 19
Copper	1085	17.1
Cobalt	1495	13.6
Nickel Alloys	1290 - 1430	12.6 - 12.8 (Invar = 1.3)
Austenitic stainless steels	1405 - 1444	16 - 16.9
Martensitic stainless steels	1400 - 1510	10.2 - 10.8
Low alloy steels	1490 - 1500	12.2
Titanium	1660	8.6
Chromium	1890	6 - 7
Zirconium	1752 - 1850	6
Niobium	2469	7.3
Molybdenum	2623	4.8
Tungsten	3422	4.5

In addition, differences in thermal conductivity lead to uneven heat dissipation,

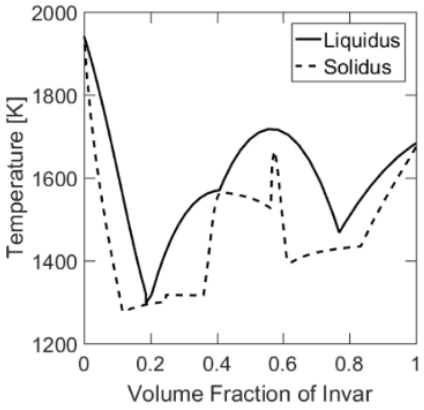

Figure 3.24: Solidus and liquidus lines as a function of the composition of Invar in a Ti-Invar FGM. It can be seen how there is almost a 700K drop in melting temperature at approximately 12 vol% (solidus) and 18 vol% (liquidus) in Invar [21].

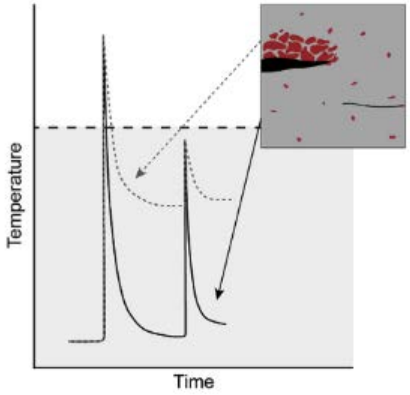

Figure 3.25: Thermal profiles of the sample. The horizontal line shows the upper-temperature limit for σ phase formation. Uniform curves represent areas with minimal cracks, while dashed curve shows areas with larger cracks related to the larger amounts of σ [22].

resulting in a lack of heat input (which may cause a lack of fusion) in some parts and, in some cases, the formation of unexpected non-equilibrium phases [104]. This comes as a result of uncontrolled heat treatments in specific zones of the part (where thermal conductivity is lower). It was also observed [22] that when cracks appear, heat cannot quickly dissipate, thus producing an unexpected thermal history that may result in greater amounts of undesired (e.g. σ) phase (Fig. 3.24 and Fig. 3.25). One potential solution is to readjust process parameters in situ to tailor the heat input. Considering common metals and alloys, both Al and Cu show high thermal conductivity, thus making them incompatible with, for example, many steel grades [138].

Joining two alloy systems with very different coefficients of thermal expansion (CTE) can also result in defects. Such mismatch (See Table 3.1) leads to stress concentrations added to the preexisting residual stresses [58] due to the uneven contraction of both constituents (the higher CTE material experiences tensile stresses, while the lower CTE material experiences compressive stresses) [138]. The amount of tension accumulated can be approximately related to these mismatches through

$$\sigma = \frac{\triangle T}{E}(\alpha_2 - \alpha_1) \ , \tag{3.2}$$

where σ is the resulting stress, ΔT is the temperature range, E the average Young modulus, and α is the CTE of each material (denoted by subscripts 1 and 2) [84].

Stresses are still present when having two materials with similar CTE, since multiple phenomena coincide (cooling rate and difference in mechanical properties lead to different plastic accommodation of stresses). These can typically be allevi-

ated with heat treatments [95, 110, 145, 183], but when the mismatch is too high, heat treatments cannot suppress the accumulated tensions [138]. Creep, fatigue, and stress corrosion cracking [138] are especially affected by this mismatch. The use of layers with materials of intermediate CTE has been a common solution from the welding community, despite some studies [33] suggesting that it is not enough. Better mismatch control can be achieved by controlling how gradually the material evolves. However, assuming that CTE has a linear variation with composition may be an inaccurate assumption [51].

3.3.2. Formation of secondary phases

The formation of intermetallic phases is one of the most challenging aspects of manufacturing functionally graded parts. While the thermal mismatch can be roughly estimated a priori and, in some cases, prevented or cured, intermetallic formation is the result of many interacting factors (composition, process parameters, cooling rates, alloy thermodynamics and kinetics, transport of species,...).

These phases are not always detrimental to the overall part quality. As a matter of fact, in some cases like in Ni superalloys, the formation of phases like γ' ($Ni_3Al(Ti)$) or γ" (Ni_3Nb) [17], which are coherent (semicoherent in the case of γ") with the Ni matrix, are used to strengthen the material. This is a case where the relation of atomic radius (Al/Ni = 1.14, Ti/Ni = 1.17, Nb/Ni = 1.33) has a straight relation with the amount of coherence of the precipitate and the matrix. Yet, most of these phases, mostly based on ionic or covalent bonds with complex crystallographic structures, are unable to accommodate thermal and residual stresses. In addition to depleting the matrix in solute species (sometimes forming these phases at grain boundaries as in Fig 3.27), they lower the ductility and toughness and cause crack initiation and propagation (embrittlement) [132]. The depletion of the matrix can also affect the corrosion resistance (like the segregation of Cr in stainless steels, which is necessary in great quantities to maintain a good corrosion resistance).

Analyzing the expected phases in that exact composition/temperature region is useful to address this issue. For that purpose, phase diagrams are essential and can help assess the solubility limits in binary or ternary systems (See Fig. 3.28). Unfortunately, most commercial alloys are composed of multiple elements, and the effect of each one (despite having a very small amount in most cases) can be critical when analyzing this problem. This is a special challenge since the thermodynamic interactions and the kinetics of all the species become more complex.

The work from [22, 23] shows a deep characterization analysis of how σ forms in different FGMs (See Fig. 3.29 and Fig. 3.30). As mentioned, the thermal history and heat dissipation are most important, leading to phase formations deviating from thermodynamic (equilibrium) calculations.

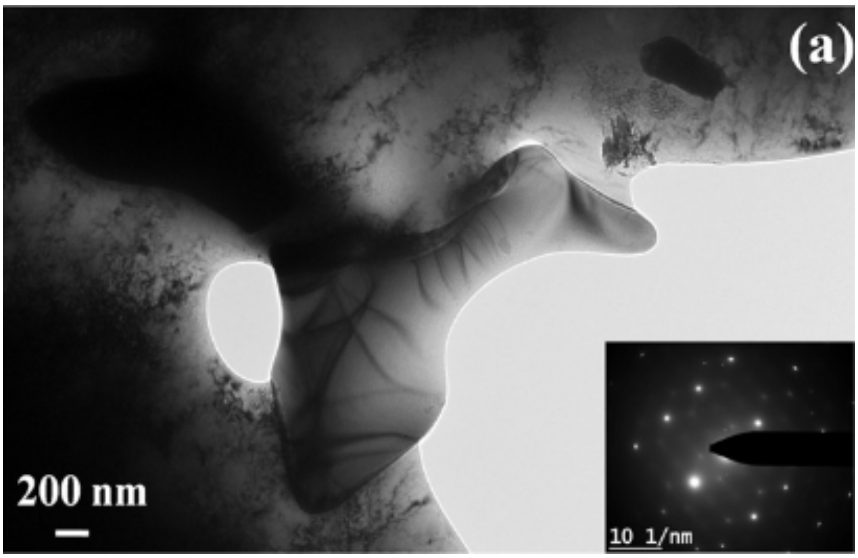

Figure 3.26: TEM image of Laves phase in an Inconel 718 alloy. [114].

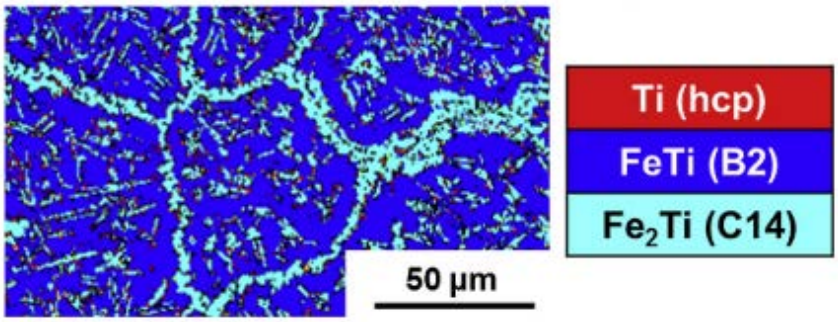

Figure 3.27: EBSD map of a Invar-Ti-6Al-4V alloy (specifically layer with 3 vol% Invar, 97 vol% Ti-6Al-4V). This map shows how the intermetallic C14 Laves phase precipitates at the grain boundaries [21].

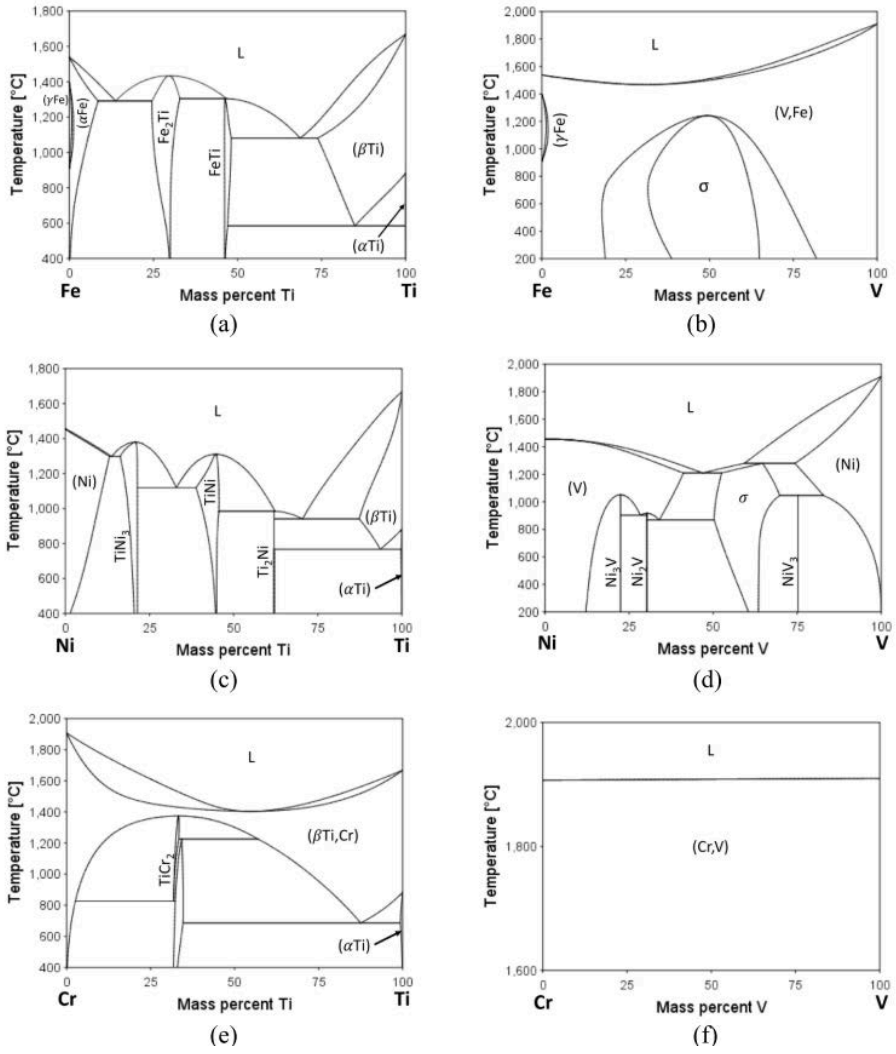

Figure 3.28: Example of multiple binary phase diagrams from common alloying elements, showing the formation of certain intermetallic phases and solubility of all phases. For example, diagram (f) shows complete solubility between Cr and V (considering equilibrium conditions), while most diagrams show at least some undesired phases like σ. All diagrams are adapted by [137] and were obtained using Thermo-Calc and the binary TCBIN database.

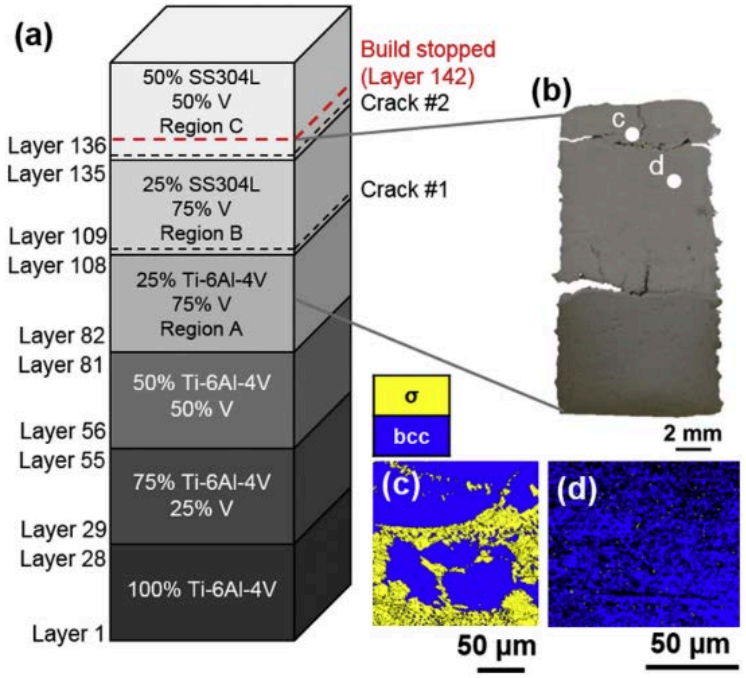

Figure 3.29: (a) Ti-6Al-4V to V to 304L stainless steel FGM (b) Cross section and (c-d) EBSD maps of the phases close and far from cracks and how the amount of σ phase changes [23].

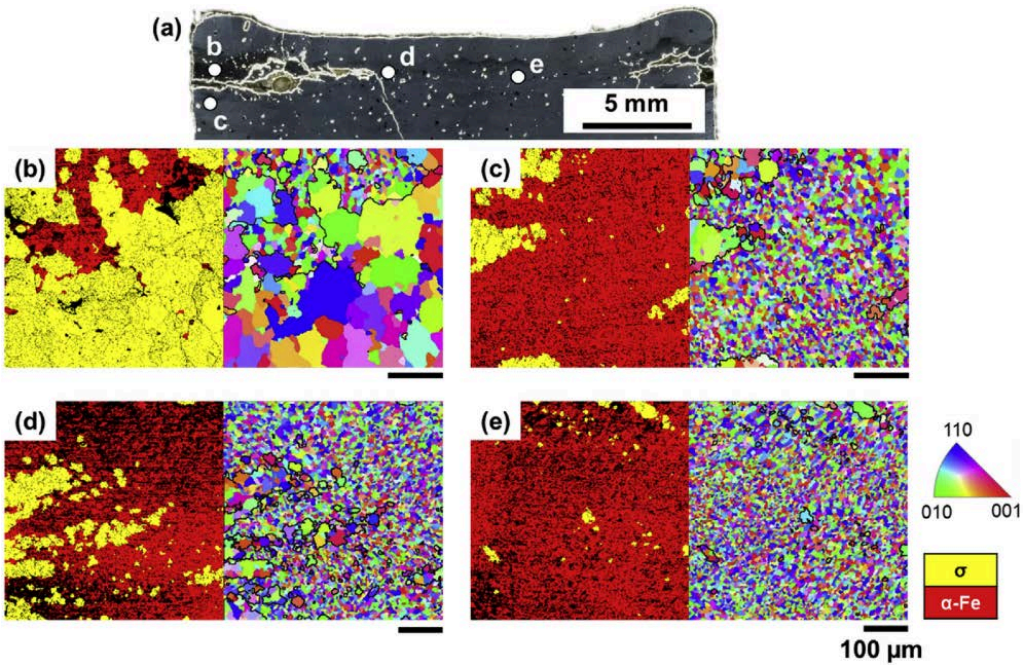

Figure 3.30: (a) Cross section of an SS420 steel to pure V. (b-e) EBSD maps of the phases close and far from cracks and how the amount of σ phase changes [22].

3.3.3. Solidification cracking

Solidification cracking is a major underlying mechanism for the emergence of defects in graded materials. This appears when grain cohesion is hindered by the formation of cracks as solidification occurs in the mushy zone (the region with a mixture of solid and liquid) [173]. When dendritic growth is present, this mushy zone may become narrow and challenging for proper liquid feeding, as seen in region 2 in Fig. 3.31, unable to accommodate contraction-related strains. In these regions, and due to the difficulty of feeding liquid, the transverse shear strength is very low compared to the liquid droplets in Region 3, where the two-phase solid has almost the same strength as the solid and can sustain the shear stresses. Region 1 can accommodate strain with sufficient liquid flow [173].

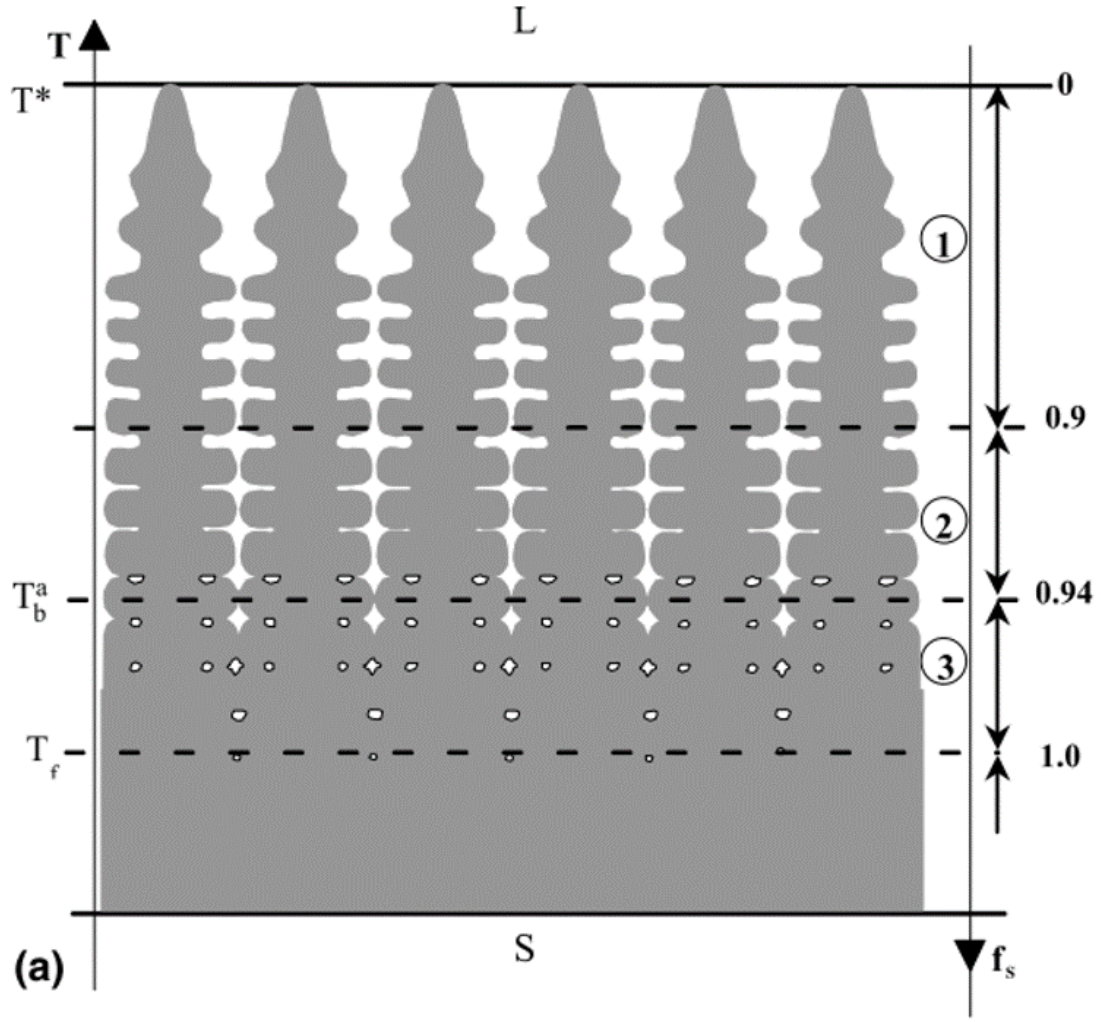

Figure 3.31: Schematic of the different regions within the mushy zone during columnar dendritic solidification. T^* (tip temperature), T_b^a (coalescence temperature of attractive grain boundary) and T_f (solidus temperature). Regions 1,2 & 3 are explained in the text [173].

For this reason, the solidification temperature range [43] and the solid fraction

evolution at high solid fraction (i.e. $f_s \approx 0.9$ and above) [173] play a critical role in assessing solidification cracking. Other factors like grain structure and primary solidification phase may also be critical [159].

Different criteria have been established to parametrize the susceptibility of cracking for a given material [135]. In our analysis, we use the classical formula proposed by Kou [90, 91, 159]

$$\mathrm{CSI} = \frac{dT}{d(\sqrt{f_s})} \tag{3.3}$$

that relates a Crack Susceptibility Index (CSI) to the variation of solid fraction f_s with temperature T, typically assessing a value close to $f_s \approx 1$ [90] or its maximum across the freezing range [157]. The solid fraction, and its evolution with temperature, may be calculated using Gulliver-Scheil calculation results.

3.3.4. Other relevant issues

Other challenges will affect the final result besides the main ones highlighted above. One of the main aspects is dilution in the melt pool, as the solidified material from the previous layer mixes with the newly added material, creating unexpected and non-negligible composition changes, especially when layer variations are considered [188]. In addition, the interaction between the melt pool, solidified material, atmosphere, and surface tension phenomena (like the Marangoni effect [97]) affect the fluid flow pattern in the melt pool, resulting in deeper or shallower melt pools.

When dealing with several alloying elements of different characteristics, it is critical to study their kinetics of diffusion and interaction since the migration of interstitial elements like C and N (since these are the fastest) causes not only the formation of intermetallics and carbides but also segregation and matrix depletion. The migration of these elements is an especially interesting phenomenon to study in the interface between the different alloys to analyze their possible compatibility. For example, C tends to form carbides with specific elements like Cr, which is necessary for stainless steel to sustain its corrosion resistance. Moreover, the diffusion of these elements is favorable in some crystallographic systems over others (like BCC over FCC), causing the formation of carbides at the interface between them that can form creep voids [58]. This is a common issue between ferritic and austenitic joints. Other phenomenons to consider include uphill diffusion [45], which happens when species move from low concentration to high concentration sites driven by differences in chemical potential [87, 156]. This can happen at high temperatures, during heat treatments, or during the component life cycle.

Any of the above can also be combined with defects related to the additive manufacturing processes itself, which may — in and of itself — already lead to great challenges to print fully dense defect-free parts even in non-graded materials [32, 48,

179]. Some of these defects are related to poor surface preparation and surface tension related to the molten material's poor wettability, leading to balling phenomena [31]. The most relevant defects are probably porosity and powder entrapment [31]. Porosity is commonly related to lack of fusion. It can be both irregular (mostly at layer boundaries and due to lack of fusion and consolidation or thermal contractions) and spherical (due to trapped gas from the feedstock material, material evaporation, or Marangoni flow from the melt pool [31]). Porosity is often a good nucleation site for cracks and reduces the ductility and fatigue strength of the final specimen [160]. Oxidation and overall material degradation during melting is often an issue if the atmosphere and process parameters are not under control. Moreover, residual stresses (often generated following the build direction [137]) are one of the most relevant defects to be controlled with laser deposition methods. These originate from the complex thermal history and the high cooling rates added to the material contraction, which can induce cracks, distortion, and other specific AM defects [31].

3.4. Summary of context and motivations

From the review above, it is clear that significant knowledge gaps remain in understanding the relationship between microstructural control and manufacturing parameters, to be able to avoid some of the defects described above. Gaining a deeper understanding of the mechanisms underlying these gradient microstructures and their impact on structural integrity is crucial for improving control over the final material properties, thereby enhancing their practical applicability.

In this context, a more comprehensive mechanical and physical characterization remains key, alongside further refinement of simulation tools. Together, these efforts will enable more precise microstructural control and support the design of materials with superior properties and broader applications.

CHAPTER 4

MATERIALS & METHODS

4.1. Materials

For our target application (injection nozzle for metal manufacturing applications), the two metallic alloys of choice are stainless steel AISI 316L (SS316L) and Ni-based superalloy Inconel 718 (IN718) as described in Table 4.1. These are two commercially qualified alloys with great corrosion resistance and, especially in the case of Inconel 718, great overall behavior at high temperatures. The austenitic stainless steel acts as a more cost-friendly solution in regions where high-temperature properties are not as critical while having good corrosion resistance and structural integrity at high temperatures. Both alloys show an austenitic matrix with similar lattice parameters and not-so-distant CTE values (13.0 µm/(m°C) for Inconel 718 and 16 µm/(m°C) for SS316L) [70].

4.1.1. 316L Austenitic Stainless Steel

This austenitic steel is one of the most common and studied stainless alloys. It has a high amount of Ni to obtain an austenitic structure and, with the addition of Cr, great corrosion resistance thanks to a duplex oxide film [70], as well as good performance at high temperatures [75]. The main difference between the 316/317 family and the 302/304 (very common) family of austenitic stainless steels is the addition of Mo, which enhances the pitting corrosion resistance, resistance at reducing atmosphere, as well as the resistance to chloride solutions. Adding Mo, which enhances the BCC structure, requires higher amounts of Ni to stabilize the austenitic FCC structure [75]. The "L" suffix stands for lower amounts of C content to prevent precipitation of carbides and thus prevent sensitization and overall matrix depletion [75]. This comes as a great solution for alloys meant to be welded (similar to laser deposition) since welded areas are the most critical in terms of corrosion resistance

Table 4.1: Nominal composition of feedstock powders provided by the suppliers.

wt(%)	Fe	Ni	Cr	C	Mn	Si	Ti	Mo	Nb	Al	Co	Cu	Ta
AISI 316L	65.99	12.60	16.90	0.01	1.30	0.60	/	2.60	/	/	/	/	/
IN718	18.25	53.07	18.92	0.05	0.01	0.03	0.92	3.11	5.15	0.42	0.05	0.01	0.01

and degradation. These alloys are used in various applications such as nuclear reactors, heat exchangers, piping, cryogenic applications [137], maritime applications, or common cutlery. Regarding additive manufacturing, several studies confirm that this family of alloys shows cellular (or "branchless dendritic") solidification [137].

Typical 316L microstructures consist of mainly FCC γ phase. Still, in some cases when dealing with welding, some δ ferrite phase may appear, which can then form σ phase [75] (normally FeCr [83]), with very poor coherence with austenite, as well as high interfacial energy, leading to increased interface cracking [131]. Therefore, this phase acts as a detrimental intermetallic that deteriorates the overall ductility and toughness [14]. This phase is especially critical when working at 650°C - 850°C and can even be observed at higher temperatures (close to 950°C [83]). It is also especially concerning with greater amounts of Cr [83].

4.1.2. Inconel 718 Ni superalloy

Nickel-based superalloys are alloy systems with great corrosion resistance and high mechanical properties at high temperatures and in oxidizing and corrosive environments. These alloys are commonly used in aircraft and rocket engines as well as power turbines and other demanding industrial applications [4] where service temperature can sometimes exceed 1050 °C and in some cases rise to 1200 °C, which is near to 90% of the melting temperature of the material [132].

These alloys have FCC γ structures, but due to the amount of different alloying elements (see Fig 4.1) and to how much these constitute of the final alloy weight fraction (up to 40% in some cases [132]), several other crystalline structures precipitate, giving different properties. The most representative precipitate is the γ' ($Ni_3Al(Ti)$) phase, which strengthens the matrix without being brittle since its microstructure (FCC) is coherent with the matrix [17, 36]. Other precipitates are the γ" (Ni_3Nb), which has a BCT structure [152] that form coherent disc shape phases, acting as a common strengthening precipitate for Ni-Fe superalloys [17], and the η phase, which has an HCP structure that may appear in cellular or intragranular fashion (this last one as acicular platelets [17]). These are known as GCPs (geometrically close-packed phases). Depending on the amount of C content, carbides (as MC (like (Ti,Nb)C), M_6C or $M_{23}C_6$) can form, being beneficial as dispersion hardeners or as grain boundary stabilizers [17]) but can also be detrimental if they consume elements thus depleting the matrix.

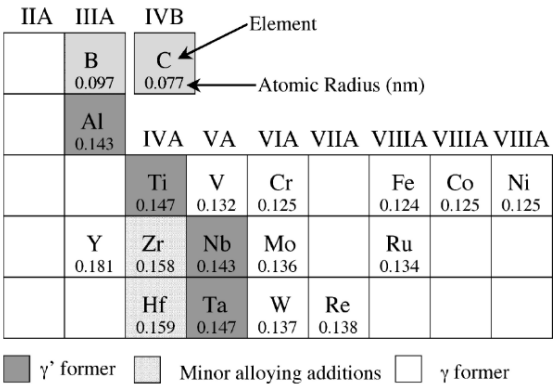

Figure 4.1: Principal alloying elements in Ni-based superalloys [132]

Conversely, these amounts of alloying elements have to be limited to avoid phases known to be detrimental to the overall integrity of the material. This group of phases is called TCPs (topologically close-packed phases) [134]. These phases, rich in refractory elements, have complex crystallographic structures, not coherent with the matrix, which are characterized as close-packed layers of atoms [132] (see Table 4.2).

Table 4.2: Principal TCPs in Ni-based superalloys (from [17, 70])

Phase	Crystal Structure	Formula	Description
Laves	Hexagonal	$(Fe,Ni,Cr)_2(Nb,Mo,Si)$	- Irregular elongated globules or platelets. - Common in Fe or Co alloys after prolonged exposure at high temperature.
σ	Tetragonal	FeCr, FeCrMo, CrCo	- Irregular elongated globules. - Common in Fe-Ni and Co alloys after prolonged exposure at 540°C - 980°C.
δ	Orthorhombic	Ni_3Nb	- Acicular shape. - Common in Inconel 718 at 815°C - 980°C - Formed by cellular reaction (low T aging) or precipitation (high T aging)
μ	Rhombohedral	$(Fe,Co)_7(Mo,W)_6$	- Irregular Widmanstatten platelets. - Common in alloys with high amounts of refractory (Mo, W) at high temperatures.

Most of the Ni-based superalloys are based on the Ni-Al binary system. Still, the 718 alloy is a precipitation-hardened alloy based on a Ni-Fe-Cr stable matrix with reinforcement coming from secondary elements like Ti, Nb, or Al [34], which gives it great strength, corrosion, and oxidation resistance as well as good creep and fatigue behavior at medium temperature. The most relevant strengthener is the γ" phase, which increases properties at moderate temperatures. When dealing with fusion processes, IN718 has some drawbacks, especially hot cracking (where post and pre-heat treatments may come as a solution [164]) and macrosegregation. The latter is a recurrent issue where the partition of elements modifies the expected microstructure composition. This often comes as the segregation of elements like Nb

to interdendritic regions, which leads to the precipitation of intermetallics like Laves phases [181] (see Fig. 4.2 as an example of different intermetallic morphologies). This has been widely studied — for instance, the work [108] demonstrated a relation between process parameters and the amount of Nb segregation. It was demonstrated that by applying low laser energy and speed (obtaining a higher cooling rate), Nb segregation was reduced, thus avoiding the formation of Nb-based Laves phases.

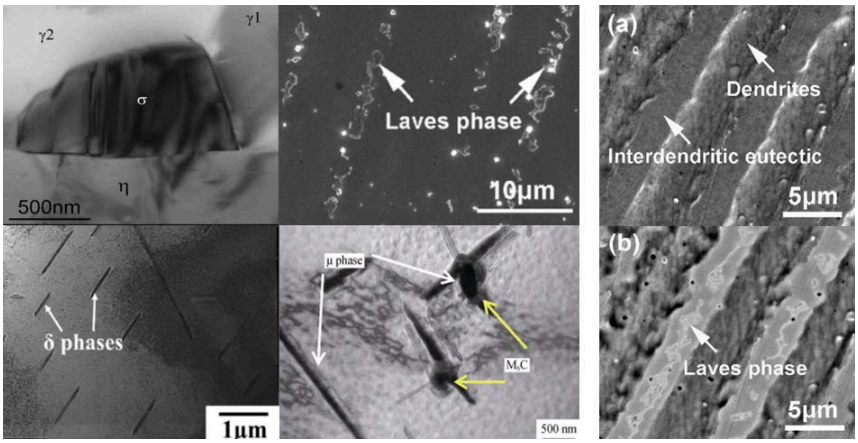

Figure 4.2: On the left side, TEM examples of some TCPs (σ [92], Laves [181], δ [93], μ [13]), carbides[13] and GCPs (η, γ', γ" [92]). On the right side, (a) Secondary electron (SE) and (b) backscattered electron (BSE) images in Inconel 718 [181].

In [108], a new procedure to avoid interdendritic Laves phase was obtained by adjusting the energy input. This laser mode, called quasi-continuous-wave (QCW) in contrast to typical continuous wave (CW) laser deposition (Fig. 4.3), offers better control of the thermal input (improved cooling rate and less solidification time) and a fine and discrete microstructure (Fig. 4.3).

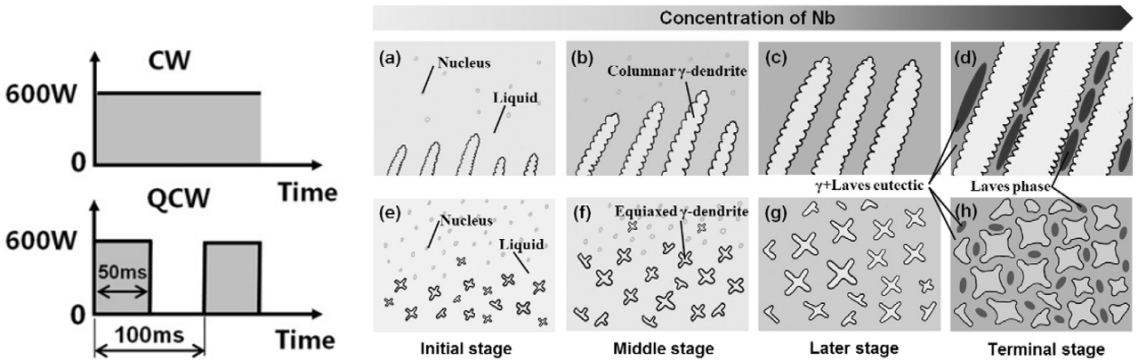

Figure 4.3: Laves phases growth with the content of Nb [181] with (a-d) CW input (e-h) QCW input [181].

4.1.3. Previous work and material compatibility

There are already some studies where we can find some insight on the combination of these two alloys. Both Fe and Ni alloys often show similar thermophysical properties and similar crystallographic structures (γ Fe-FCC Austenite with $a = 3.60$ Å, γ Ni-FCC with $a = 3.62$ Å and γ"-Ni_3Nb (BCT) with $a = 3.60$ Å and $c = 7.41$ Å). Dissimilar fusion joints have greatly interested the welding community, even though solidification cracking has come as an obstacle [140, 159]. This cracking comes as a result of the segregation of elements and impurities, which then cause detrimental phases formation and low melting liquid films along the grain boundaries [140] that fail when shrinkage appears during solidification [137]. This could be fixed in some cases by reducing the grain size [140] by carefully controlling the process parameters.

In recent years, there have been some studies about making FGMs out of these alloy systems. In one of these studies [180], 316L/IN718 graded joints were done with different grading directions (see Fig. 4.4). Strong directional growth appears (through <100> crystallographic directions and texturing in the (111) plane). Columnar dendrites appear to prevail more in FGM1 (columnar to equiaxed transition) than in FGM2 (see Fig. 4.4). It is also stated that by adding more IN718, the primary arm spacing of dendrites increases as a result of a decrease in temperature gradient due to heat accumulation as the overall deposition gets thicker.

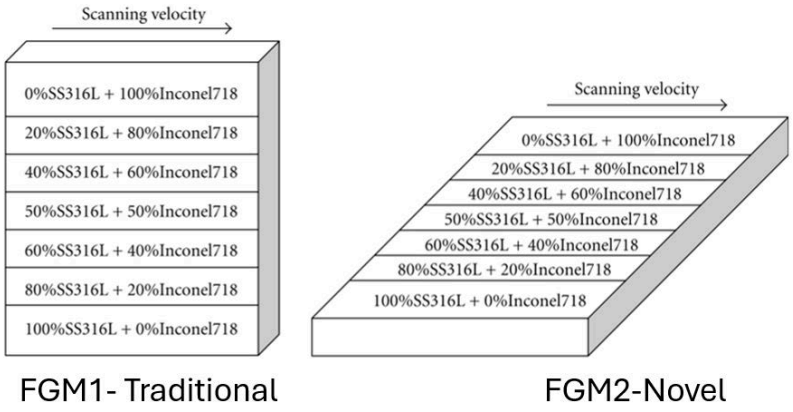

Figure 4.4: Sketch of both FGM builds. (Adapted from [180]).

In terms of mechanical properties, this change in grading directions exhibits a clear bimodal behavior, as shown in Fig. 4.5. Also worth mentioning that, for FGM1, microhardness exhibits a gradual drop when adding In718 to the mix, whereas FGM2 shows almost a linear increase in microhardness with the addition of IN718. In both cases, the hardness values increase with the amount of IN718 thanks to the addition of solid solution-strengthening elements like Mo, Nb, Cr, and Ti. Friction tests show good wear resistance all around.

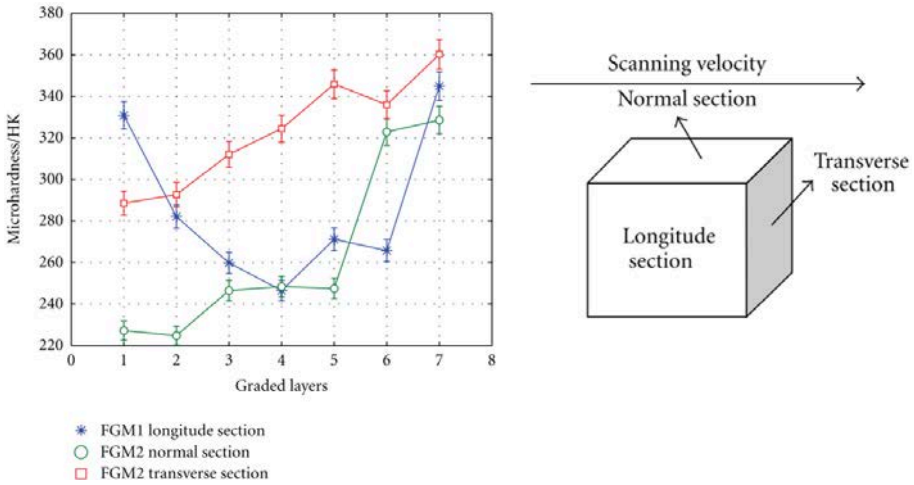

Figure 4.5: Microhardness results out of FGM1 and FGM2 [180]

Other relevant publications [148, 149] show columnar grains that provide good bonding between layers. In contrast, the transitions between columnar and cellular microstructure do not negatively affect the sample's integrity, as the hardness test shows. Process parameters like power and powder mass flow and solidification rates significantly influence secondary dendritic arm spacing (SDAS). With lower values of laser power, lower SDAS was obtained. The tensile strength was also related to the variation of these parameters, showing increased values with powder mass flow rate and being inversely proportional to the laser power. The formation of NbC carbides (at higher Inconel contents) was observed, serving as a potential parameter to fine-tune the hardness of the joint depending on its content.

The work in [70] uses electron beam AM to join both alloys, depositing 316L on an IN718 substrate and vice versa. IN718 deposition onto 316L showed no porosity or cracks and a columnar grain structure with some precipitates (intra and intergranular), which most likely are NbC, showing depletion of Fe, Ni, and Cr and enrichment of Nb and Mo. Other C-depleted areas still show the formation of other phases that seem to be TCP phases. This can be explained by adding more Fe content to the matrix, the solubility of Nb and Mo decreases [70]. Further analysis showed a 2:1 relation between (Fe, Ni, Cr):(Nb, Mo, Si), which fits the relation for Laves phases. These low melting point phases can lead to solidification cracking. Microhardness along the joint is consistent and shows no relation with the difference in the grain morphology. SS316L deposition onto IN718 showed a columnar structure, different from the expected equiaxed in 316L. Some defects like partly melted powder and unmelted/unconsolidated layers appear, as well as intergranular cracking in the unmelted zone (UZ), fusion zone (FZ), and heat-affected zone (HAZ). Interdendritic porosity and some intragranular precipitates were present in the UZ. After fabrication, the substrate showed carbide formation and acicular δ phase (Fig. 4.6). Beneath it, there was no apparent formation of this phase due to the exposure below its solidus temperature (996°C). Dilution of Fe in the FZ

while having an increasing concentration of Nb, Mo, and Ni justifies the formation of precipitates and the carbides caused by a higher concentration of C in that zone.

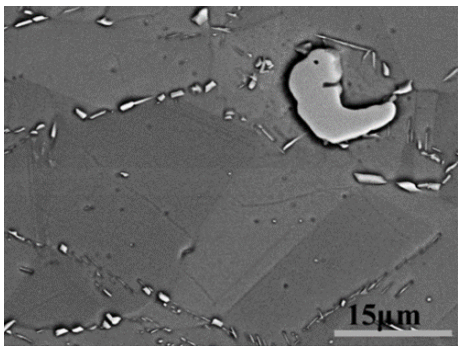

Figure 4.6: Image of acicular δ phase [70]

Energy-dispersive X-ray spectroscopy (EDS) analysis of the cracks shows a high content of Cr and C where $M_{23}C_6$ carbides can form at intergranular sites after exposure at elevated temperatures (700°C - 900°C), depleting the matrix and being a cause of intergranular corrosion [105]. Cracks could be caused by the difference in CTE (IN718 has higher stiffness at higher temperatures, which causes poorer warpability and less ability to accommodate tension from the interface). For this issue, a pre-heating treatment is convenient for the substrate. Hardness was consistent (apart from a drop in hardness values next to the interface in the 316L area).

The composition gradient as a process parameter of an IN718/316L FGM joint was studied [161], where three different gradient steps (20% (component A), 10% (component B) and 5% (component C)) were manufactured (Fig. 4.7). All gradients showed good layer bonding, linear change of the elements along the gradient, and columnar dendrites with some equiaxed grains (interface between morphologies occur at the edge and top areas of the samples due to uneven heat flow direction [94]). Primary dendritic arm spacing (PDAS) increased (with more fluctuations) with smaller composition gradients. The maximum value of PDAS appears at 100% IN718. The relation between PDAS and composition gradient can be caused by the heat accumulation of several deposited layers, which leads to a coarser columnar microstructure. In addition, decreased cooling rates give time for remelting secondary dendrites, promoting the growth of the primary ones. This concludes that a small composition gradient is unsuitable for obtaining a fine and dense microstructure. In further composition analysis, it was observed that by 60% of Inconel, secondary phases appeared in interdendritic sites. EDS showed the presence of Nb and Mo enriched Laves phases. The 316L was mainly constituted of austenite and some small areas of ferrite, while the addition of Inconel (as low as 20%) showed some peaks of secondary phases.

In terms of microhardness, it was observed that at first, the 316L solidified as primary ferrite, thus obtaining a higher value. After several deposition and heat accumulations, this primary ferrite undergoes a “ferritic-austenitic solidification mode”,

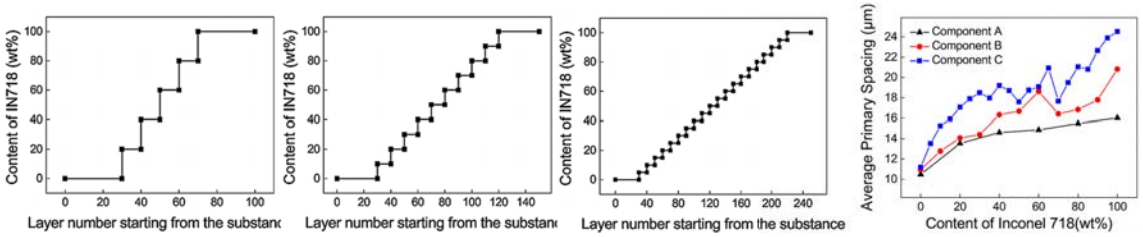

Figure 4.7: Variation of PDAS between the three component gradients [161]

resulting in austenite and some small (5%) values of retained ferrite, which caused a decrease in hardness. When more content of Inconel is added, the content of Nb and Mo increases, reinforcing the matrix up to a peak until secondary phases are formed, depleting the matrix and lowering the values of overall microhardness. With decreasing composition gradient (component C), the distribution of microhardness values shows larger ranges; This can come as a result of increasing PDAS with the composition gradient, values which relate to the size and compactness of the dendrites varying more as they grow larger.

Tensile tests showed that component B (with 10% steps) had the highest UTS (Ultimate Tensile Strength) elongation to failure and intermediate yield strength. With component A (5% steps), thermal cracks are the source of decreased properties. Fracture characterization showed micro-pores induced failure, where Laves phases are the main source of micro-pore formation.

In [118], blocks of multiple alternating layers of IN718 and SS316L were manufactured by DED to investigate the deposition of each material, its microstructure, and several mechanical properties. Fig. 4.8 shows that two different interfaces appear depending on what alloy is deposited on top of which. This results from applying different laser inputs to each alloy since the temperature intervals between solidus and liquidus differ. The volumetric laser energy density (VED) of IN718 is smaller than in 316L, causing the need to apply more power when depositing this alloy, causing remelting of some of the previously deposited Inconel layers. This produces melt pools with more intermixing of elements, thus creating gradual interfaces. Other properties, such as thermal conductivity and laser absorption (both lower in IN718), are important factors. Regarding microstructure, the sharp interface shows a clear boundary regarding grain size, while the gradual interface shows grains of IN718 and SS316L of similar size (Fig. 4.8). This coarsening of the 316L grains results from the difference in thermal conductivity between both alloys. Sharp interfaces show higher values of tensile properties, while the gradual interfaces show scattered tensile strength values. These scattered results can result from a more heterogeneous distribution of elements in the gradual interface. Tensile tests did not show any difference in the elastic regime. However, plastic deformation and fracture behavior differ when checking the density of microstructural defects. This shows that the gradual interface houses microstructural defects in approximately 15% of the frac-

ture surface area while sharp interfaces show up to approximately 2.5%. Overall, the tensile properties were closer to the weaker alloy (316L). Fracture resistance was also studied, showing that it increases when the crack grows from IN718 to 316L, while crack extensions seem to appear when going from 316L to IN718.

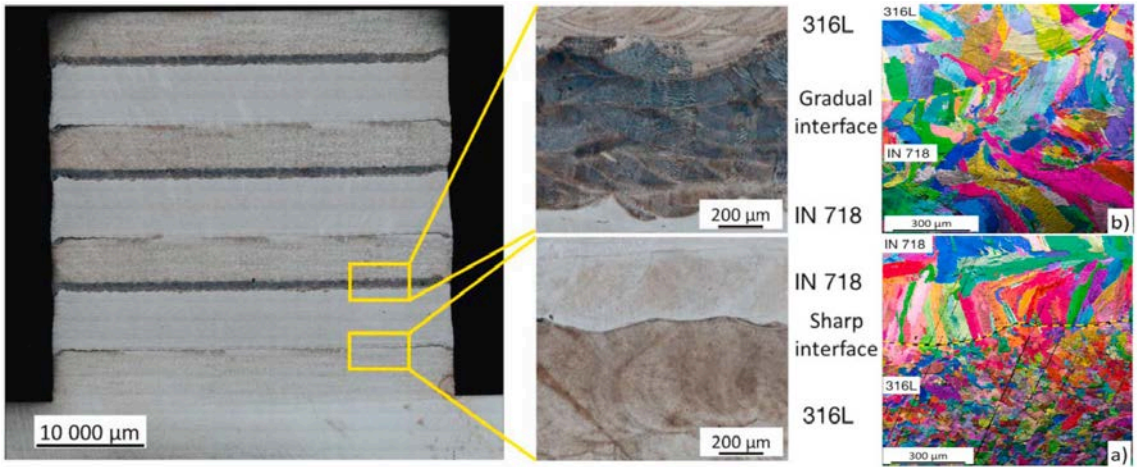

Figure 4.8: Optical microscope image that shows the different interfaces as well as EBSD mapping of both interfaces[118].

As in [70] previously described, a recent study [125] also shows the formation of Laves and δ'' when analyzing the microstructure of DED manufactured IN718-SS316L FGMs. It also highlights the formation of δ-ferrite dendritic structures at entire 316L contents that evolve into fully austenitic with the slightest values of IN718 in the mix. When increasing the values of IN718, the austenite grains start disintegrating due to the secondary phase growth (Laves and δ''). In addition to this analysis and overall mechanical characterization, along with some other work mentioned before, there is also a comprehensive wear-resistance study to optimize milling processes better. The result was that downward milling from 316L towards IN718 is the optimal solution for different industrial applications.

Another recent study [146] gives a deeper insight into grain morphology evolution along the gradient, especially when comparing as-build to different types of homogenization treatments. The microstructure after homogenization shows the formation of MC-carbides (probably NbC carbides), removing the Laves phase as seen in Fig. 4.9. Fig. 4.10 reveals that we obtain a grain-refined microstructure for a high content of IN718 (around 77 wt.%) and especially for an exposure time of 1h. Authors suggest that this could come as a result of grain boundary pinning particles due to carbide formation, residual stress-induced stored energy due to the unique laser melting process, or entropic influence on diffusion kinetics.

SS316L-IN718 alloy mixtures have also been studied for other additive manufacturing techniques, most recently using selective laser melting (SLM) [61, 143]. The work in [61] uses a graded pre-mixed powder tank to manufacture an FGM sample, obtaining sound samples that show columnar to equiaxed transition and gradual

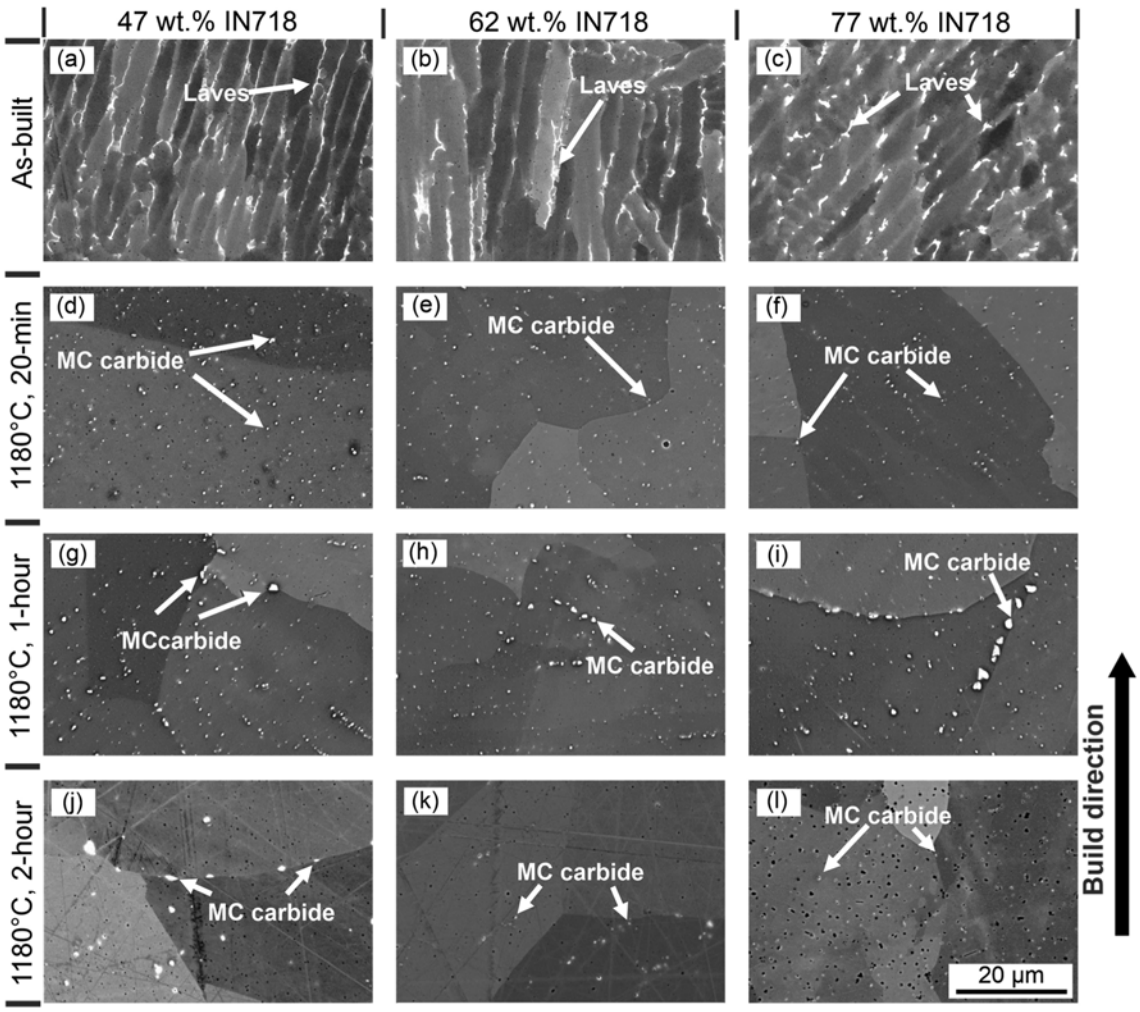

Figure 4.9: SEM images showing the microstructure evolution along an SS316L-IN718 alloy mixture. (a-c) As-built condition. (d-l) Samples after homogenization at 1180°C after different time exposures. MC carbides are highly concentrated with Nb and can be considered as NbC. [146].

change in composition but with low resolution in terms of grading steps. In the case of [143], several layers of SS316L are deposited. Afterward, they switch the powder tank to IN718, and several layers of this alloy are deposited. In this case, a sharp transition was formed, followed by a high-pressure torsion (HPT). This severe plastic deformation process has been demonstrated in this study to be very useful for consolidating and eliminating porosity in the joint.

In summary, substantial work has already been done on the grading or joining these two alloy systems, illustrating the great interest and strong potential in their combination.

Moreover, most advanced studies on FGM have demonstrated the need to combine multi-scale characterization and testing with computational thermodynamics, in particular based on CalPhaD analyses, which has already been done extensively with other alloy combinations, but not with this alloy combination, which was mostly

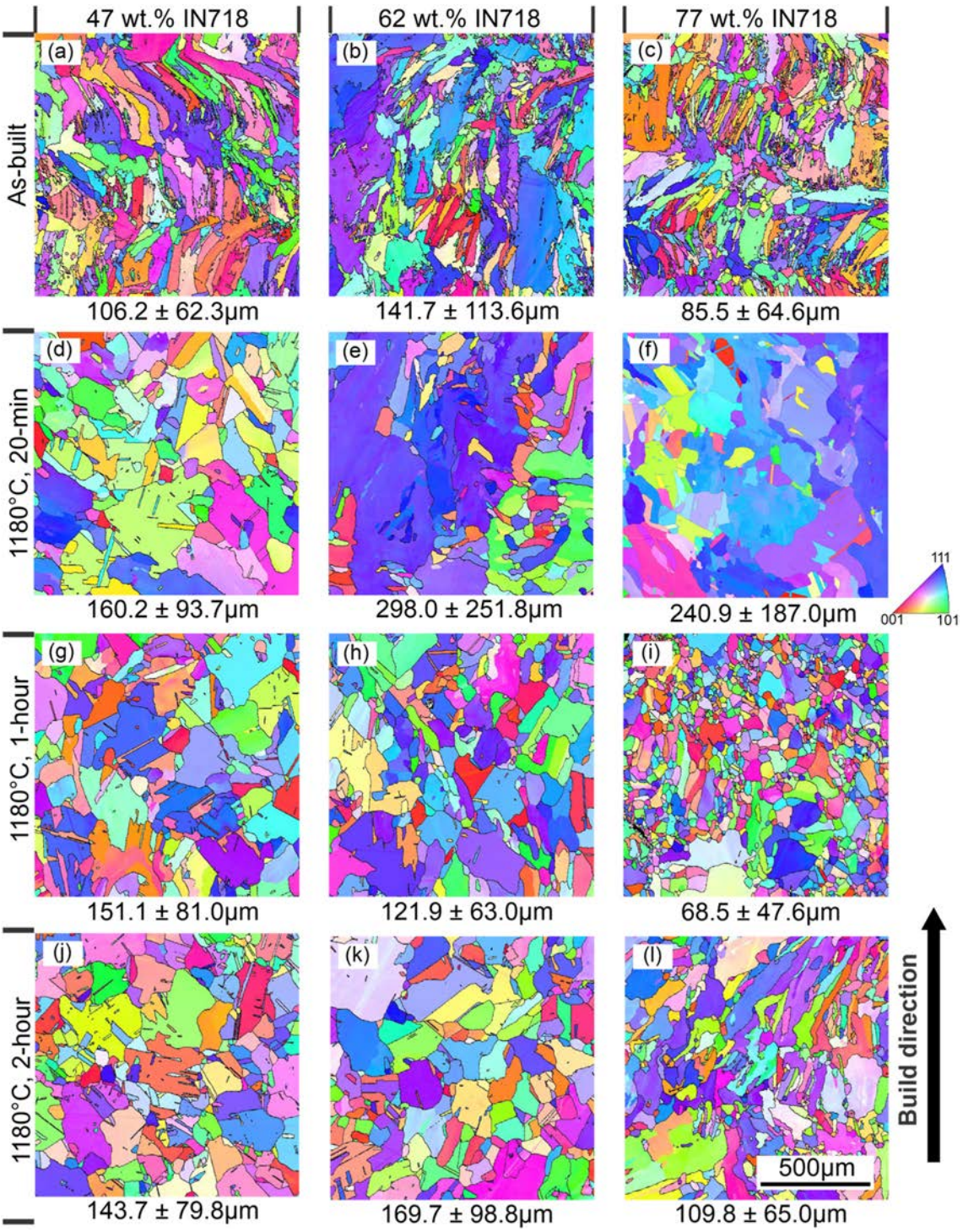

Figure 4.10: IPF generated maps of different mixed within the gradient. (a-c) As-built condition. (d-l) Samples after homogenization at 1180°C after different time exposures. The average grain size and standard deviation for each case are shown below each image. [146].

studied experimentally.

For these reasons, there are still some areas to tackle and push further to better understand the material compatibility and the growth of different defects. Most

of these studies detail a consistent change in grain morphology, interdendritic crack formation, and intermetallic formation – and several of them highlight the formation of these defects, but their underlying causes often remain elusive. Hence, further quantitative analyses remain required, in particular in correlating potential defects (e.g. micro-cracks) with microstructures, phases, solute segregation and heterogeneous properties at the microstructural scale.

Here, our main objective is to advance our understanding of these underlying mechanisms. To do so, we rely on FGM printing experiments using different printing strategies (e.g. changing the discrete composition step between layers along the gradient), followed by a broad range of characterization (microscopy, diffraction, spectroscopy) and mechanical testing (macro/micro-hardness mapping, dilatometry, compression) campaigns, supported by thermodynamic (CalPhaD) calculations.

4.2. Experimental Work

4.2.1. Fabrication

Throughout this study, all printed samples have been fabricated using powder as the feedstock material at AIMEN Technology Center in Galicia, Spain. The 316L powder was supplied by Höganäs AB, and the IN718 powder by MetcoAdd. The composition of the feedstock powders is detailed in Table 4.1. Manufacturing was done using a DED-LB/Mp setup with a Coax8 powder nozzle, a Medicoat powder feeder, a BEO D70 laser head with a Trudisk 16kW laser, and utilizing Argon as the shield gas. Printing parameters varied depending on the alloy (1.8 kW power input for IN718, 1.3 kW for 316L, and 1.5 kW for the gradient zone). Deposition velocity remains constant for all regions and configurations (10 mm/s) and powder flow rate changed between IN718 (6 g/min) and the 316L and gradient (8 g/min) regions.

All printed samples consisted of straight walls of width ≈ 7 mm, length ≈ 63 mm and variable height depending on the grading configuration. All samples consisted of first depositing 30 layers of 316L on a stainless steel plate, followed by the specific gradient configuration, and followed by 30 layers of IN718. Different gradient configurations, illustrated in Fig. 4.11, were explored to study their effect on the evolution of microstructure and properties between both materials.

A first batch of samples (labeled FGM05, FGM10, and FGM20) was manufactured with variable composition steps per layer, namely changing the mixing of alloy powders by steps of 5, 10, and 20 wt.%, respectively. With a constant layer height of ≈ 0.67 mm, the composition of each layer was changed, hence resulting in a gradient zone of ≈ 14.07 mm (FGM05), ≈ 7.37 mm (FGM10), or ≈ 4.02 mm (FGM20).

A second batch (labeled FGM10-2C and FGM20-5C) was also fabricated using a specific number of layers per composition step in order to keep the height of

the transition zone similar to the FGM05 sample, hence resulting in a composition change every two layers for FGM10-2C and every five layers for FGM20-5C.

Three other configurations were explored. Sample FGM20-SP was manufactured as the FGM20 configuration, but using the same printing parameters (1.3 kW) throughout the entire wall. Sample FGM-S was built with a sharp transition from full 316L to full IN718 between successive layers.

Finally, sample FGM70-10 was built with a sharp transition from 316L to 70 wt.% IN718 and then continuing in steps of 10% until IN718. This last configuration was chosen due to the presence of cracks in the region with low amount of IN718 mixed with 316L.

Other samples were printed for dilatometry testing. These consisted of cylindrical samples of 6 mm in diameter and approximately 10 mm in length, precisely cut to obtain two parallel planar surfaces. Each cylindrical sample was printed by mixing 316L and IN718 in a fixed proportion in order for each to represent one given composition along the gradient. Using steps of 10 wt.%, we thus printed 11 different compositions to be tested (including the two full-316L and full-IN718 end members). In total, we printed 33 such samples in order to perform three tests per composition.

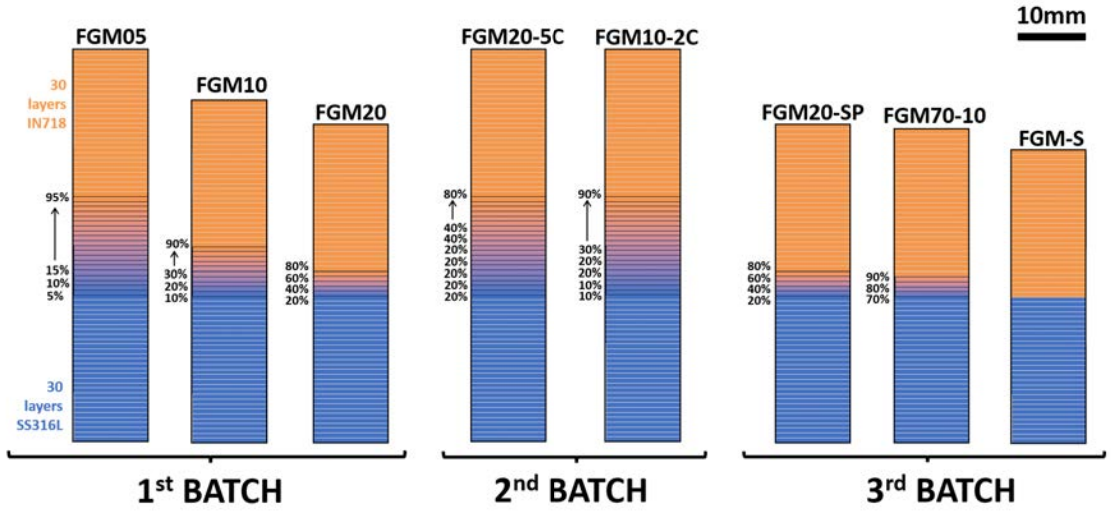

Figure 4.11: All grading configurations studied during the time of this work. From each pillar, numerous samples were extracted for several uses.

4.2.2. Microstructural Analysis

All as-fabricated pillars were sectioned with abrasive rotary disc-cutting machines into specimens that were 15.5 mm in width and up to 58 mm in length (depending on the gradient configuration). In all cases, samples were ground with SiC grit paper

and polished up to 0.25 µm with diamond slurries and slightly etched and further polished with OP-S (colloidal silica) as the final stage of metallographic preparation.

The microstructure of all samples was examined with both optical (Olympus BX51) and scanning electron microscopes (SEM) (Thermo Fisher Apreo 2S LoVac and FEI Quanta Helios NanoLab 600i). Additional EDX (Energy Dispersive X-ray spectroscopy) analysis was performed along with the SEM characterization to study the composition profiles of both alloys, especially focusing on interface morphologies and segregation patterns. In this case, an Oxford detector attached to the Zeiss EVO MA15 system was used, and the processing of the spectra was done using the INCA software. We also identified the phases and grain morphology of the samples using the Kikuchi patterns obtained from an EBSD (Electron backscatter diffraction) detector (NordlysNano from Oxford Instruments). To do so, we used an accelerating voltage of 20 kV, with all samples tilted at 70°, providing an EBSD image with a pixel size of 0.05 µm. The overall data post-processing was handled with the AZTEC software and TSL OIM Analysis tools. To obtain the information from the phase maps, we utilized the default HKL database from Aztec, as well as adding the crystallographic information for some phases (Fe2Nb(C14Laves).hkl, Fe7Mo6(MuPhase).hkl, Ni3Nb(Delta).hkl, NbMo.hkl, NiNb.hkl, NiNb2.hkl). All micrographs discussed in the following sections are oriented parallel to the build direction (BD), which is indicated by an arrow on each micrograph.

In the presence of cracks, we used an automated combination of optical micrographs to build a composite image of approximately 13.5 to 14.5 mm (through the wall thickness) by 4 to 6 mm along the height of the sample, roughly centered along the cracked region, with a resolution better than 1 µm/pixel (namely 1.15 pixel/µm). From the resulting images, we removed the regions exhibiting indents from the hardness tests, adjusted the maximum brightness, applied a thresholding to the 8 bit-converted grayscale image, and filtered resulting regions with a circularity below 0.5 using FIJI–ImageJ ("Analyze Particle" tool). This procedure results in a global cracked area fraction and average area of crack features, used to quantitatively compare the different samples.

Figure 4.12 shows processing steps for the quantification of cracks in (a) FGM05, (b) FGM10, and (c) FGM20. For each sample, the blue-outlined image is the raw optical montage, with regions used for indentation removed (blank areas). The center green-outlined image shows the processed image after brightness adjustment (typically, resetting its maximum to ≈ 180), conversion to 8-bit grayscale, and binary thresholding (at ≈ 200). The red-outlined images, shows the final cracked areas, after a particle analysis filter (considering only regions with a circularity ≤ 0.5).

Complementarily, some XRD (Panalytical Empyrean X-ray Diffractometer) analysis was also performed during the international stay at the Colorado School of Mines. This allowed a deeper understanding of phases and residual strain concen-

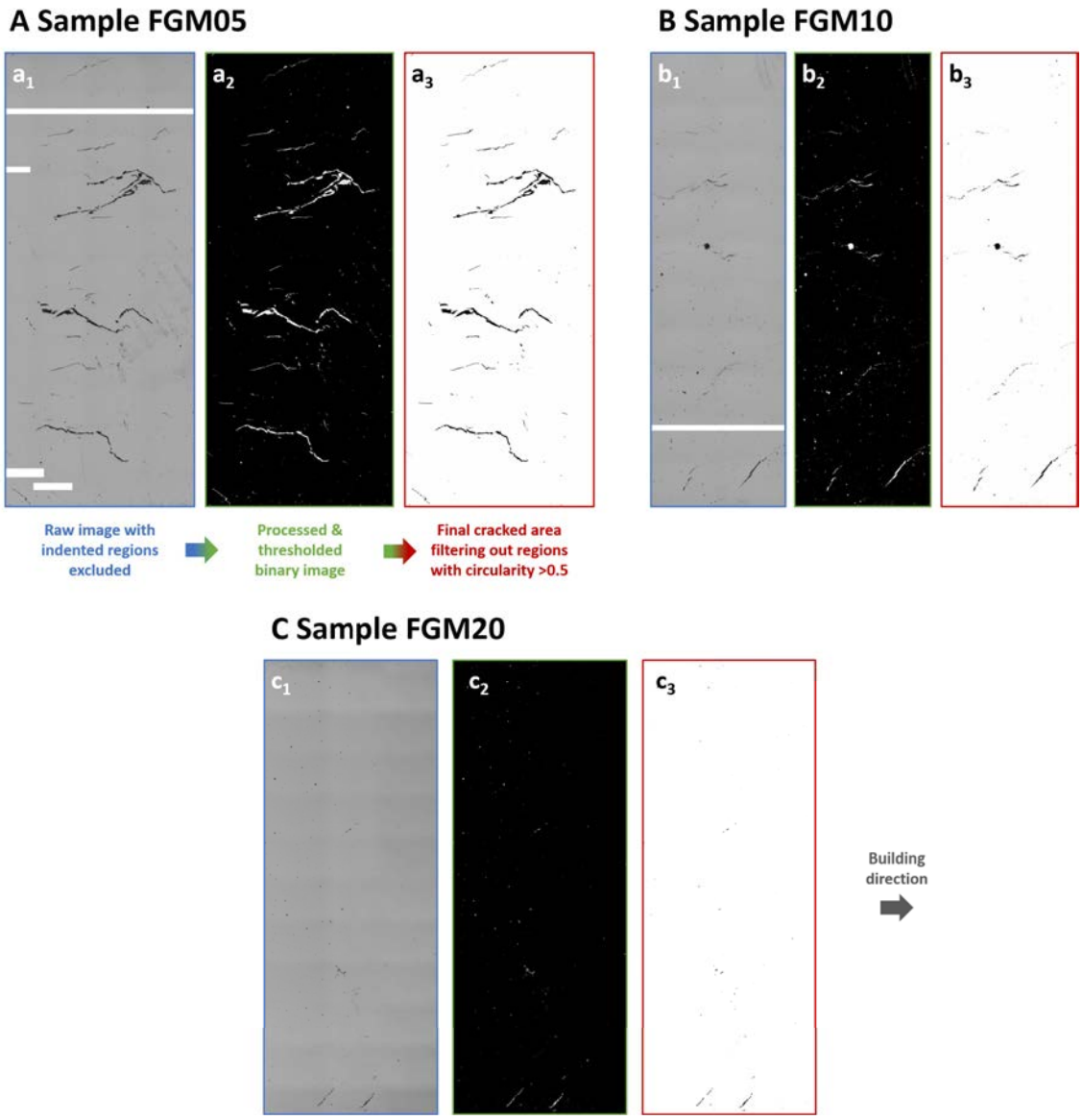

Figure 4.12: Analysis of cracked regions for (a) FGM05, (b) FGM10, and (c) FGM20, showing different steps of the image processing procedure: (a_1,b_1,c_1) raw optical images with indented regions removed, (a_2,b_2,c_2) Processed image after brightness adjustment, and grayscale thresholding, and (a_3,b_3,c_3) final resulting cracked regions. The analyzed regions are: (a) 14.5×6 mm^2, (b) 13.5×4 mm^2, and (c) 14.5×5.5 mm^2.

tration when analyzing the peak intensity, broadening, and shift in the XRD spectra along different angles. This equipment also allowed for sequential measurements by changing the position of the X and Y axes in the sample, enabling complete scans along entire FGM samples. We utilized Cu-source X-rays and Cr-source for the fixed angle and residual strain measurements for basic scans.

4.2.3. Mechanical Characterization

Microhardness tests were performed throughout the entire surface of the FGM05, FGM10, and FGM20 samples. Indents were done using an Innovates Microhardness equipment by applying 200 gf (gram-force) with 10 seconds of dwell time every 150 µm in a straight line, following the build direction, resulting in 190, 110, and 84 indents per sample, respectively. The spacing between indents was adjusted to avoid any overlapping of plastically deformed zones. In order to correlate micromechanical properties with segregation patterns from EDX analysis, we also performed nanohardness mapping on the same sites using a Hysitron TriboIndenter TI950. With its integrated optical microscope, it was possible to find the same area where the EDX map was obtained.

Several nanoindentation maps were obtained by performing an array of indents using a maximum load of 1 mN and loading, holding, and unloading times of 0.1 second. The indent spacing was adjusted to cover the desired area while avoiding overlapping of plastically deformed zones under each indent. The load-displacement data at each point was then analyzed to obtain hardness values by using the Oliver and Pharr method [126].

The smaller maps were made by programming a grid of 20×20 indentations with an indent spacing of 0.8 µm, covering an area 16 µm $\times$ 16 µm. Bigger maps comprised a grid of 22×22 indentations with an indent spacing of 1.5 µm, covering an area of 30 µm $\times$ 30 µm.

Compression tests were also carried out to evaluate macroscopic properties within the gradient and compare with bulk alloys. These were performed on cylindrical samples (9 mm in length and 6 mm in diameter) extracted from FGM05, FGM10, and FGM20 specimens, with the cylinder axis aligned with the build direction (illustrated in later Fig. 5.17). Testing was performed using an Instron 3384 universal testing machine, using two tungsten plates in contact with the sample and with an applied strain rate of 0.54 mm/min. The load was recorded from the machine while the displacement was collected by an LVDT (Linear Variable Displacement Transducer) system.

4.2.4. Dilatometry

Dilatometry tests were carried out to examine the evolution of thermal expansion along the gradient, which has been documented as a potential cause of cracking in FGMs [136]. For that purpose, we analyzed 33 cylindrical samples of 6 mm in diameter and approximately 10 mm in length, each printed with a given 316L-to-IN718 composition ratio. The samples (three of each composition) were cleaned with ethanol in an ultrasonic bath, tested under the same heat ramp, applied force (0.25N) with a NETZSCH DIL 402 Expedis Supreme system, calibrated using fused

silica specimens, and under an Ar atmosphere. The CTE (coefficient of thermal expansion) values were calculated from the obtained dilatometry curves between (150-300) °C using the NETZSCH Proteus software.

4.2.5. Physical simulation

In addition to the characterization and testing procedures mentioned above, we also explored and assessed the potential use of physical simulation (e.g. Gleeble experiments) to study the material compatibility of SS316L and IN718 alloys.

To perform these physical simulation tests, a Gleeble 3800 thermo/mechanical simulator (Dynamic Systems Inc.) was used. It allows the user to simulate heat treatments (even with specific mechanical constraints) in small specimens as if dealing with macroscopic samples in an industrial environment. The heating of the sample is done by Joule effect where an electric current circulates through the sample, while strategically placed thermocouples control the temperature. Due to the high melting temperature of both alloys, R-type (Platinum Rhodium -13% / Platinum) thermocouples were needed. Compressed air or water quenching system can be attached to control the cooling rates, which add to the cooling channels from structural parts inside the system (like the grips) that allow for structural integrity for the machine parts. Fig. 4.13 properly depicts the setup, temperature and force cycle applied in this case.

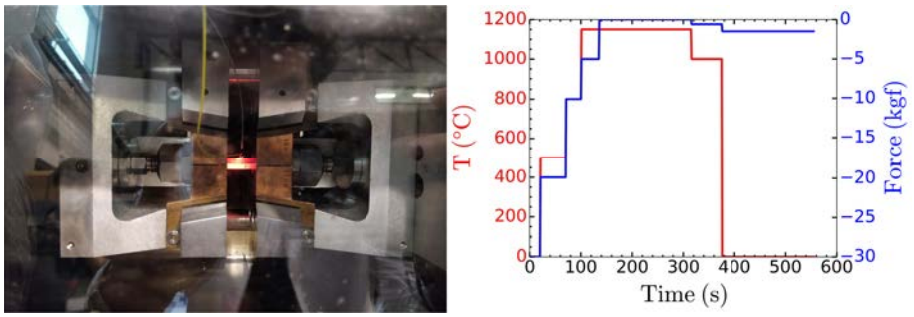

Figure 4.13: (Left) Picture of the Gleeble setup, using Cu grips and R-type thermocouples are attached to both samples. (Right) Curves of both temperature and, applied forces during the cycle.

The objective of using this system is to simulate the dissimilar joining of 316L and IN718 alloys and check whether it is possible to create a sound joint in the first place and afterward analyze the microstructure, paying special emphasis to the interface and interdiffusion that may occur. Since both alloys have close melting temperature T_m, one needed to be better insulated (in this case, IN718, as it has a lower T_m) than the other to melt only one of them. With that in mind, a special setup (see Fig. 4.14) was designed, where two cylindrical samples (50×10 mm) of stainless steel and one (5×10 mm) of IN718 in the middle are joined. The region of

the intermediate IN718 cylinder was covered with Tungsten foil to retain as much heat in that area as possible. This foil also works as a physical barrier for the liquid metal until it solidifies. One reference thermocouple was welded to one of the 316L rods and one to the IN718 to control the temperature. ArcelorMittal provided all rod samples.

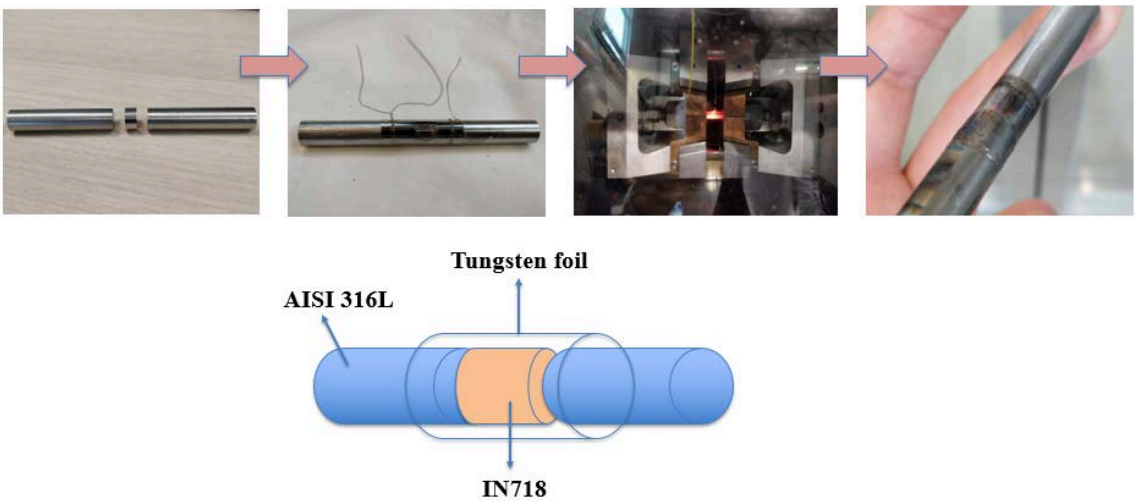

Figure 4.14: Picture (top) and schematics (bottom) of the sample setup, from the initial specimens until the final bonded part.

4.3. Computational Thermodynamics (CalPhaD)

We supported the interpretation of our experimental results with a range of thermodynamic calculations, using the CalPhaD (Calculation of Phase Diagrams) method. Here, all simulations were performed using the Thermo-Calc software, versions 2022a and 2024a (Thermo-Calc Software AB, Solna, Sweden) with the TCNI8, TCFE9, and TCHEA6 databases, depending on each case.

First, we calculated different phase diagrams, including relevant binaries (e.g. Fe-Ni, Fe-Cr, Fe-Mo, and Fe-Nb systems) and ternaries (e.g. Fe-Ni-Cr, Fe-Ni-Cr, and Fe-Ni-Mo systems). We also calculated the temperature-composition intersection of the full multicomponent phase diagram with the composition going linearly from full-316L to full-IN718 composition. These phase diagrams are useful as they provide a baseline for potential secondary phases (e.g. intermetallics) that would be expected from the major alloying elements.

We also calculated different solidification paths along the gradient. We considered both full equilibrium (i.e. lever rule) and Gulliver-Scheil assumptions for nominal compositions ranging from 316L to IN718 with intermediate steps of 10 wt.% mixing of alloys. Gulliver-Scheil simulations, assuming instantaneous species diffusion in the liquid state and null diffusion in the solid state, tend to be more reasonable

for relatively fast processes, such as DED, except for fast diffusing elements like C or N (present in steels).

When performing Gulliver-Scheil simulations, we perform local equilibrium of the remaining liquid during solidification, removing the formed solid at each step and thus resetting the overall composition to the one of the new liquid (Fig. 4.15). In the case of full equilibrium (Lever rule) solidification, the entire system is considered at each step, considering both diffusion in the liquid and the solid, allowing solid-state transformations to occur [67]. Some modifications of Gulliver-Scheil, which include back-diffusion of fast-diffusing elements, can reach para-equilibrium states, but in the case performed, no significant differences appeared between models.

The resulting output is useful to assess the microsegregation patterns of the different elements during the solidification process, and it provides input data for solidification cracking criteria [159]. In both lever and Gulliver-Scheil calculations, we particularly track the fraction of phases, as well as their species concentrations.

Finally, we also used CalPhaD to calculate the coefficient of thermal expansion (CTE) across the gradient by estimating the volumetric expansion between 150 and 300°C, here using the TCFE9 database. This data is meant to be compared with dilatometry results and thus assess the capability of the CalPhaD approach to provide reasonable CTE predictions (critical for the design of new metallic FGMs).

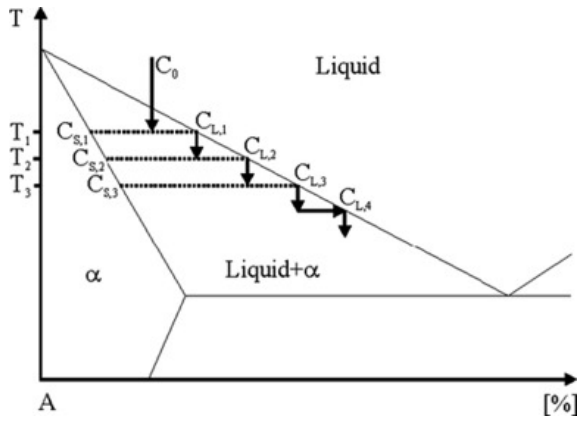

Figure 4.15: Schematic of the Gulliver-Scheil model [147].

CHAPTER 5

RESULTS

5.1. Microstructural Analysis

Feedstock

The first step was to properly select and characterize the feedstock powders to be used for the fabrication process. This characterization campaign was done collaboratively with AIMEN Technology Center, choosing a 316L powder provided by Höganäs AB and an IN718 powder provided by MetcoAdd, with compositions detailed in Table 4.1.

The IN718 powder, shown in Fig. 5.1, showed a better average size distribution and sphericity than other options from other suppliers (e.g., Metcocladd). When analyzing the microstructure of the powder with SEM, we observed a clear dendritic structure, mostly concentric towards the surface of the particle. When analyzing the composition of both the dendritic and interdendritic constituents by EDX, there was a clear difference in Nb content, observing a jump of even double the expected wt.%, depleting base elements such as Fe, Ni, and Cr.

When analyzing the 316L powders, the selected powder showed a good size distribution, with an overall precise composition range compared to theoretical values. The microstructure also shows a dendritic structure (Fig. 5.2), with few oxide inclusions in some of the particles, as well as some formation of carbides.

Printed samples

Following the steps described in the method section, the first batch of samples was printed, as shown in Fig. 5.3. After some grinding, these three pillars already show three distinctive areas (316L, Gradient, IN718) as well as the meltpool arrangement

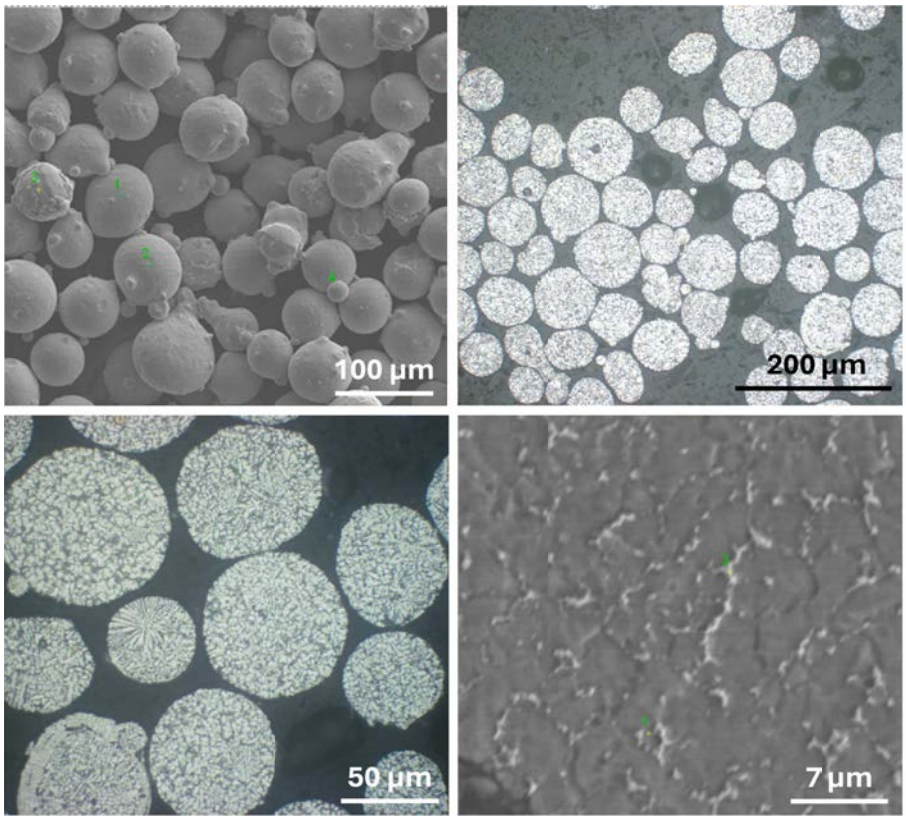

Figure 5.1: Micrographs of IN718 powder.

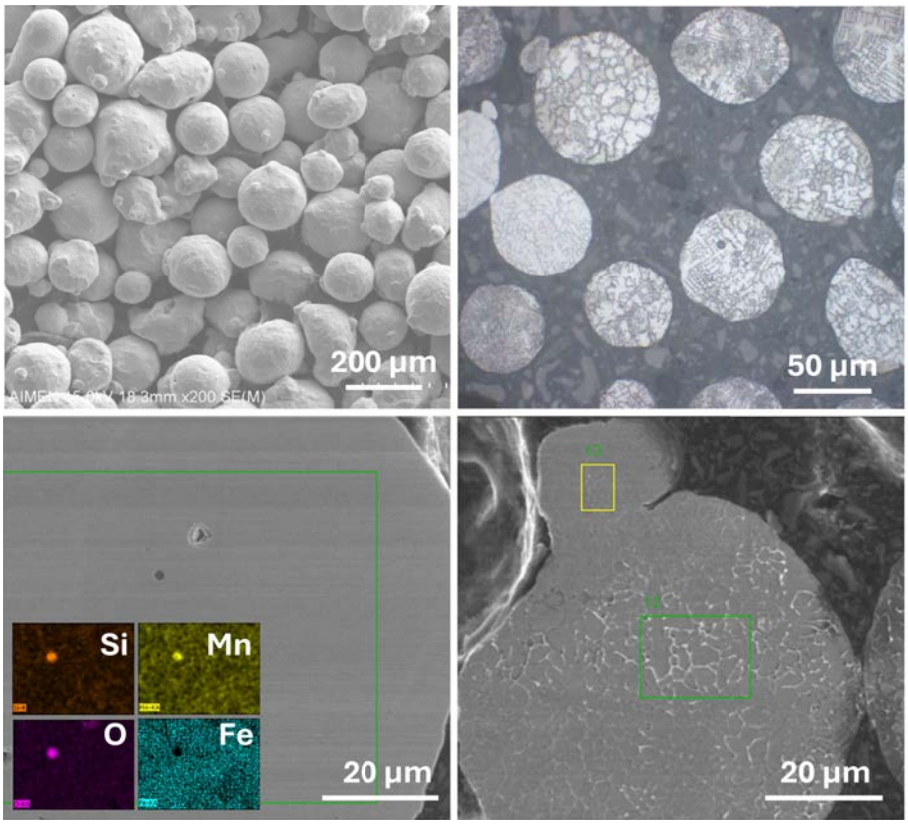

Figure 5.2: Micrographs of 316L powder.

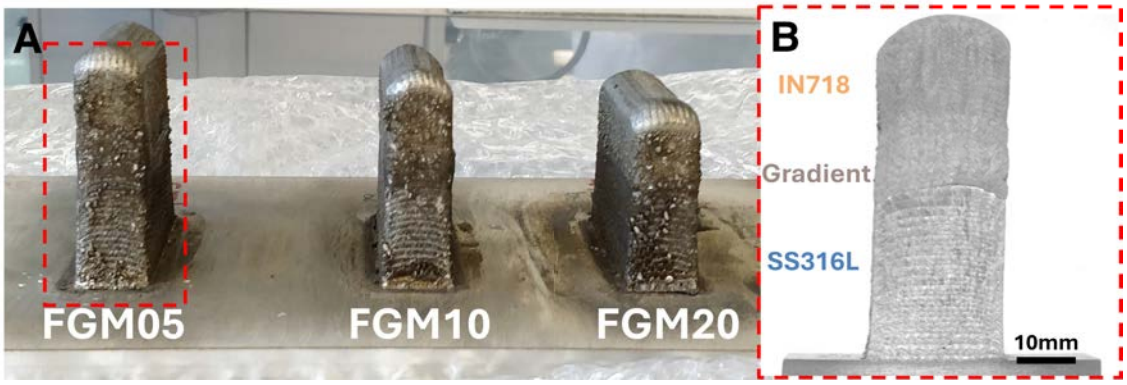

Figure 5.3: DED-printed samples studied here: (a) photography of as-printed walls still attached to the 316L base plate; (b) macrograph cross-section of the FGM10 sample, showing single-alloy as well as grading regions;

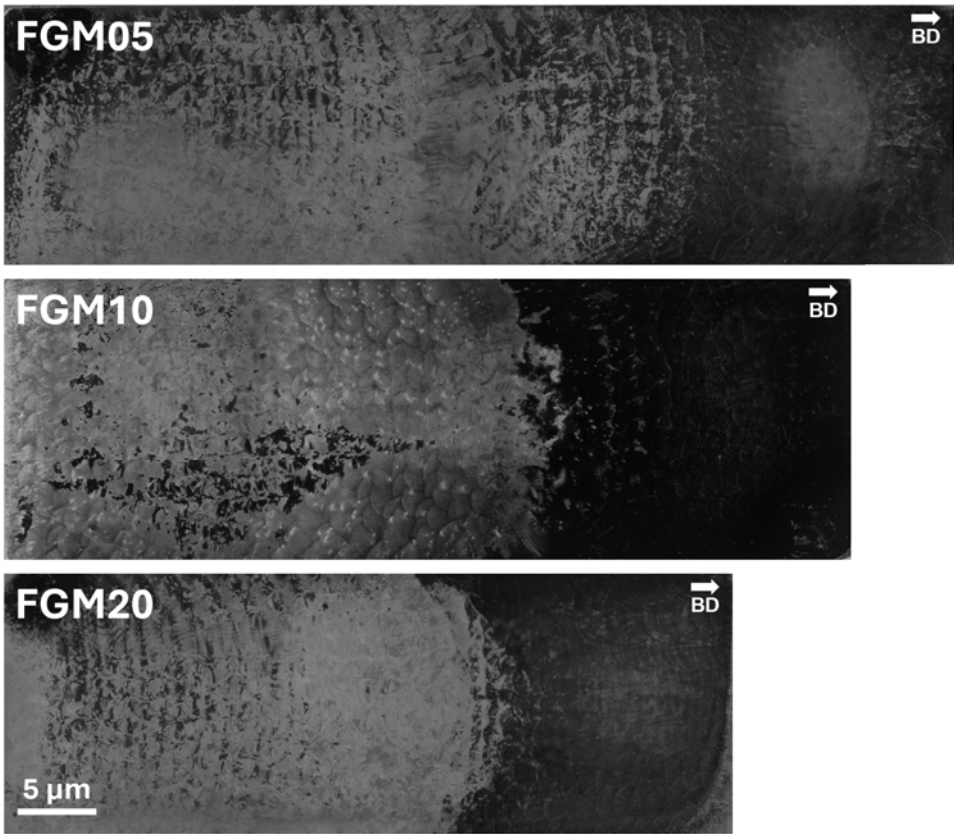

Figure 5.4: Polished samples after etching.

and morphology (Fig. 5.3). When trying to grind deeper, polish, and attack, these samples presented a particular challenge, as having different compositions on the same sample meant different hardness values and interaction with the etchant. This is visible in Fig. 5.4, where we can also see the melt pool layout in better detail.

Qualitatively, all microstructures present columnar grains that become progressively finer with increasing IN718 content (Fig. 5.7). This is consistent with previous works [98], which suggested that this may be attributed to the increased heat ca-

pacity with the increasing weight percent of IN718. Intergranular segregation is also remarkable for all concentrations along the gradient, but increasingly so when increasing the content of IN718. These patterns already appear with the smallest amount of IN718 in the gradient and become increasingly more present.

Most samples exhibit significant cracking in the gradient, more specifically within a range approximately from about 10 to 25 wt.% IN718. Figures 5.6 and 5.7 shows micrographs of samples FGM05, FGM10, and FGM20, all experiencing intergranular cracking in this region. Cracks are typically oriented along the build direction or close to it. These cracks also follow the intergranular segregation patterns, as better illustrated in Fig. 5.7 (b-c) and Fig. 5.9(a-b). FGM05 shows, both in density and length, a higher susceptibility to cracking, while the configurations with the largest compositional steps and hence the lowest number of steps, namely FGM20, shows the fewest and smallest cracks.

A subset of the images used to extract quantitative measurements of the crack features, as well as the post-processed binary thresholded images are illustrated in Fig. 5.5. The resulting fraction of cracked area is 1.03% with an average feature (i.e.

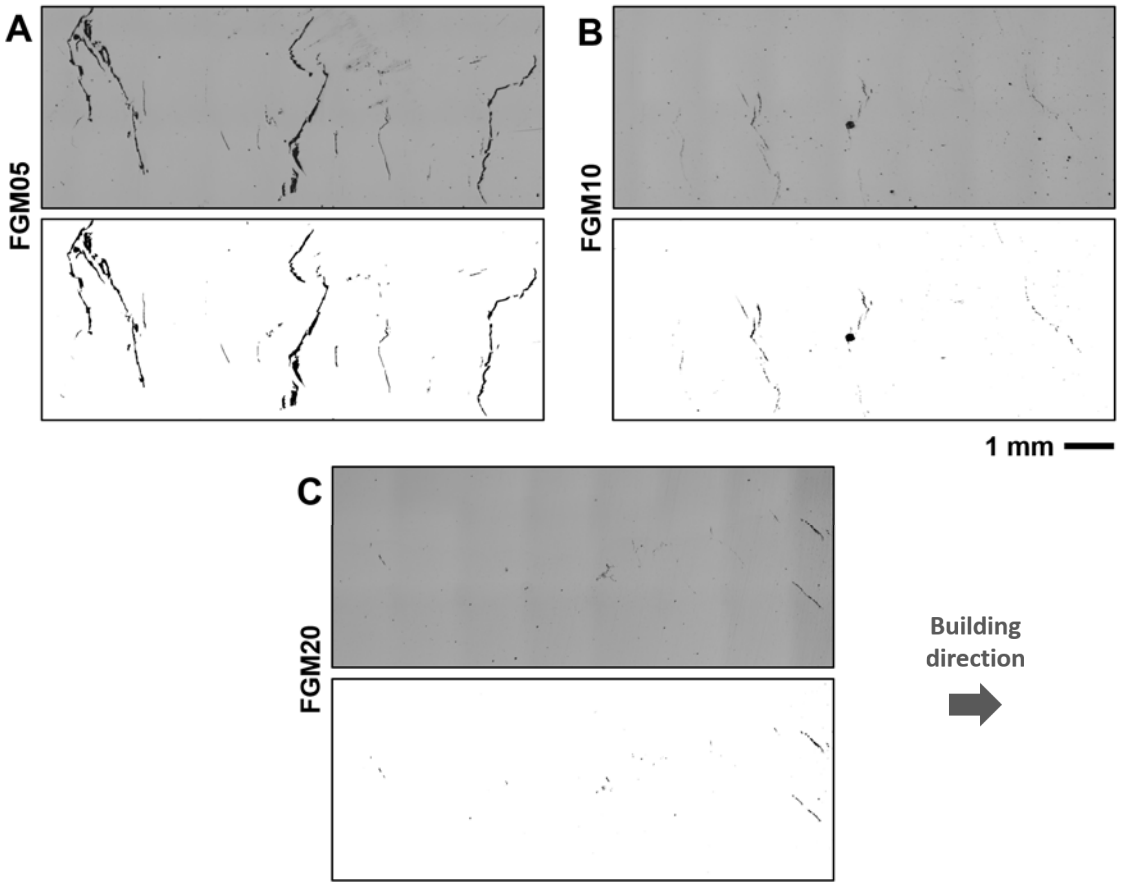

Figure 5.5: Cracked areas in (a) FGM05, (b) FGM10, and (c) FGM20 samples: (top) images from optical microscopy and (bottom) post-processed binary thresholded images used to calculate the cracked region area.

crack) size of 3859 µm^2 for the FGM05 sample, compared to 0.330% and 425 µm^2 for FGM10, and 0.057% and 257 µm^2 for FGM20, respectively. In the FGM05 sample, some cracks span several millimeters in length. Hence, even though the cracks are typically located in the 10–25 wt.% IN718 range, with a layer height of 0.67 mm, this corresponds to a cracked composition range actually broader than 20% IN718.

Cracks follow the interdendritic segregation patterns, as detailed in Fig. 5.9. Some of these cracks appear next to eutectic structures (Fig. 5.9c) typical of late-stage solidification in strongly segregated regions. The EBSD phase map in Fig. 5.9e identify this eutectic structure as a mixture of Ni-rich and Fe-rich FCC phases, with some amount of C14 Laves and traces of δ phase. Such secondary phases (Laves

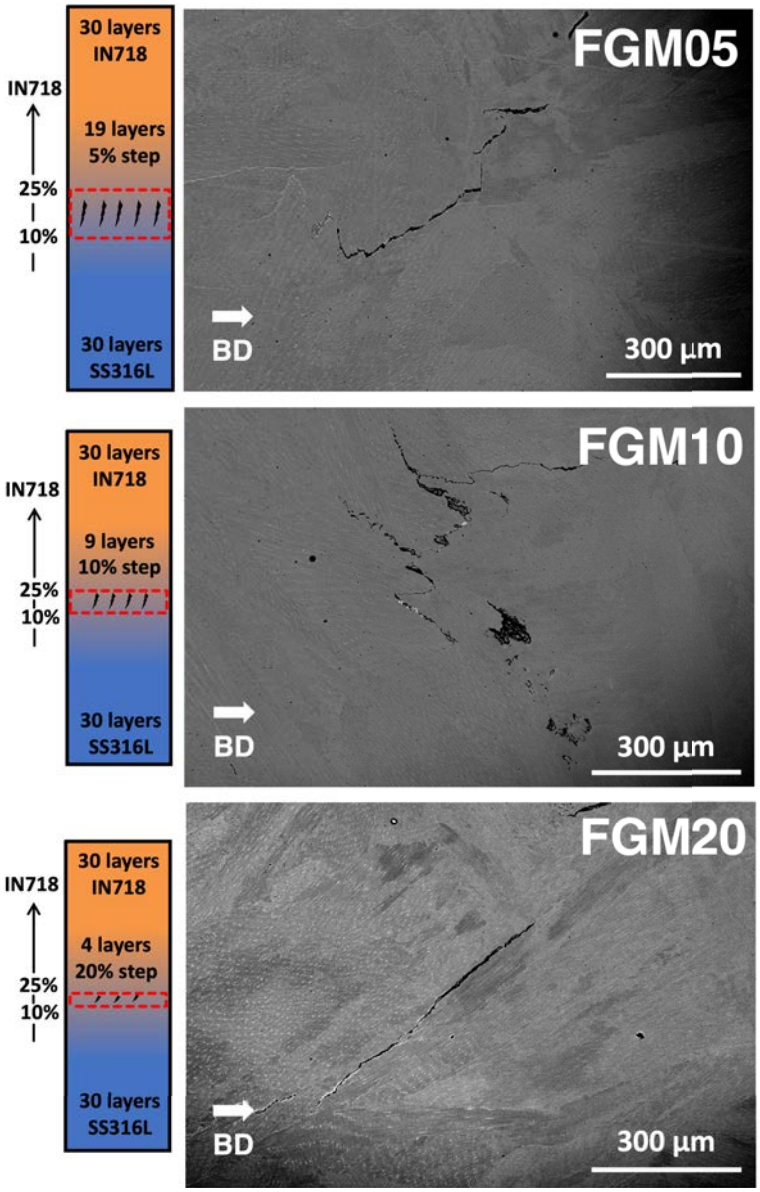

Figure 5.6: SEM micrographs of FGM05, FGM10 and FGM20 samples illustrate the crack morphology and grain structure. The schematics illustrate the region where cracks appear and their size and density.

and δ) are typically undesired due to their detrimental impact on the mechanical properties [132]. Previous works from other groups have also reported that secondary phases in additively manufactured FGMs are often associated with cracking, possibly linked to the change and heterogeneity in heat flow along the sample [22].

Counterintuitively, the results of the first batch suggest that a steeper composition gradient reduces the extent of cracking. Hence, the selection of additional printing parameters for the second (FGM20-5C, FGM10-2C) and third (FGM20-SP, FGM70-10, FGM-S) sample batches was aimed at studying the effect of the total gradient height (batch 2) and other printing parameters, such as laser power or a steep jump to 70 wt.% IN718 (batch 3) on crack mitigation. The resulting microstructures are illustrated in Fig. 5.8.

In the second batch, cracks were still present in all configurations, hinting at a lack of direct dependence on the height of the graded region. FGM20-5C, illustrated in Fig. 5.8a, had a comparable crack density as the worst-case scenario of the first batch (FGM05), while the FGM10-2C microstructure, shown in Fig. 5.8b, was close to that of the FGM10 sample, with an intermediate number of cracks.

In the third batch, with a fixed set of printing parameters, the FGM20-SP sample (Fig. 5.8c) showed similar defects as the previously printed FGM20 from the first

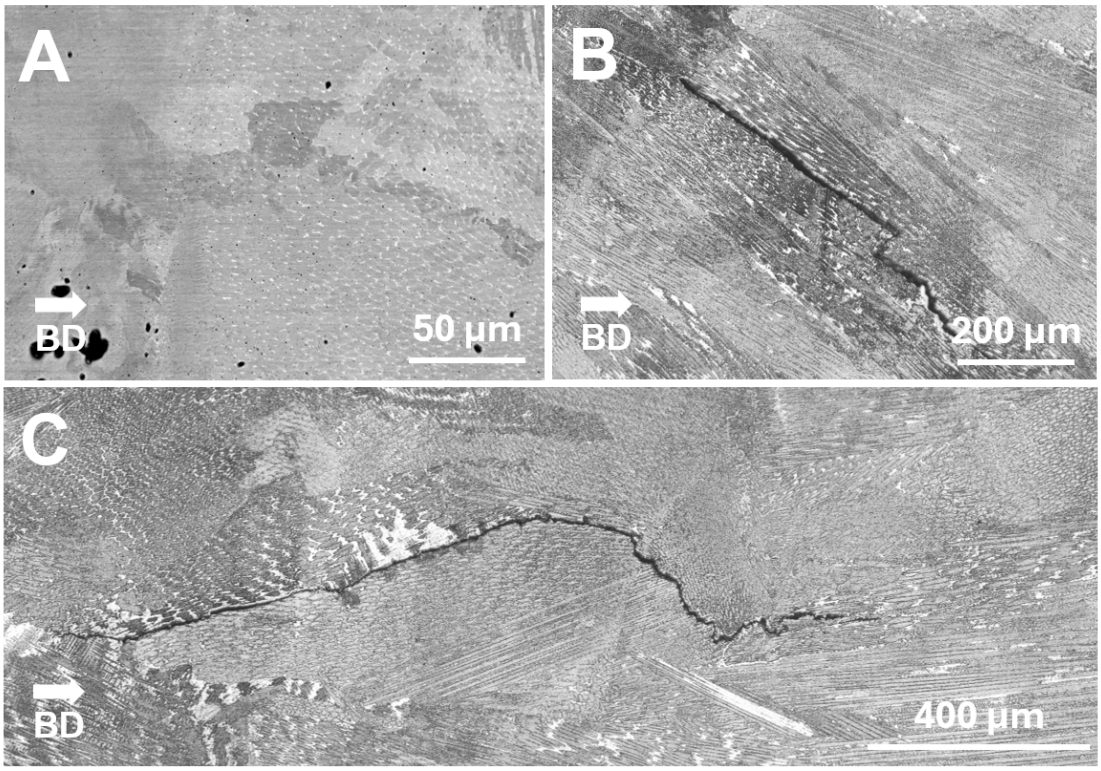

Figure 5.7: (a) Transition microstructure between 316L and small additions of IN718. (b-c) Different cracks of different scale lengths throughout segregated areas. All pictures exracted from FGM05.

batch, also suggesting a relative independence upon laser power (as long as the rest of the sample could be printed with close to no defect). Sample FGM-S with a sharp transition instead of a progressive gradient between alloys (Fig. 5.8d) also revealed cracking as the other samples, in this case right in the boundary between both alloys, but in less quantity that the worst case scenarios in FGM05 or FGM10. In comparison, FGM70-10 with a sharp transition from 316L to 70 wt.% IN718 and then steps of 10 wt.% IN718, hence jumping over the typical high crack density region, exhibited significantly reduced crack density and typical crack length (Fig. 5.8e). However, cracking was not fully avoided in any of the samples. Our interpretations of the origin and underlying mechanisms for cracking are discussed further on the basis of extensive microstructural and mechanical analyses, as well as thermodynamic calculations detailed in the following subsections.

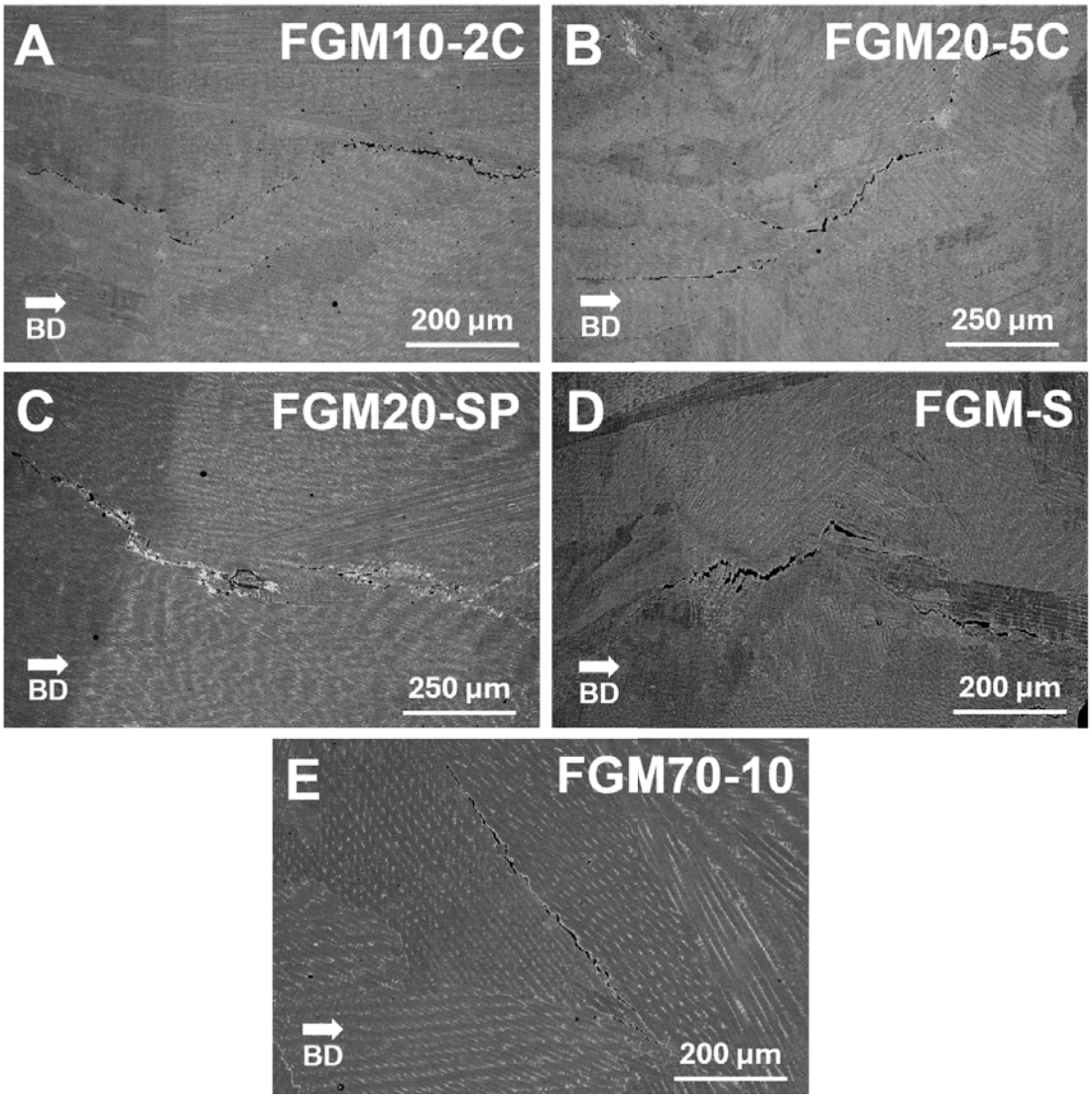

Figure 5.8: SEM micrographs illustrating the different crack morphologies for the different samples of the last two batches.

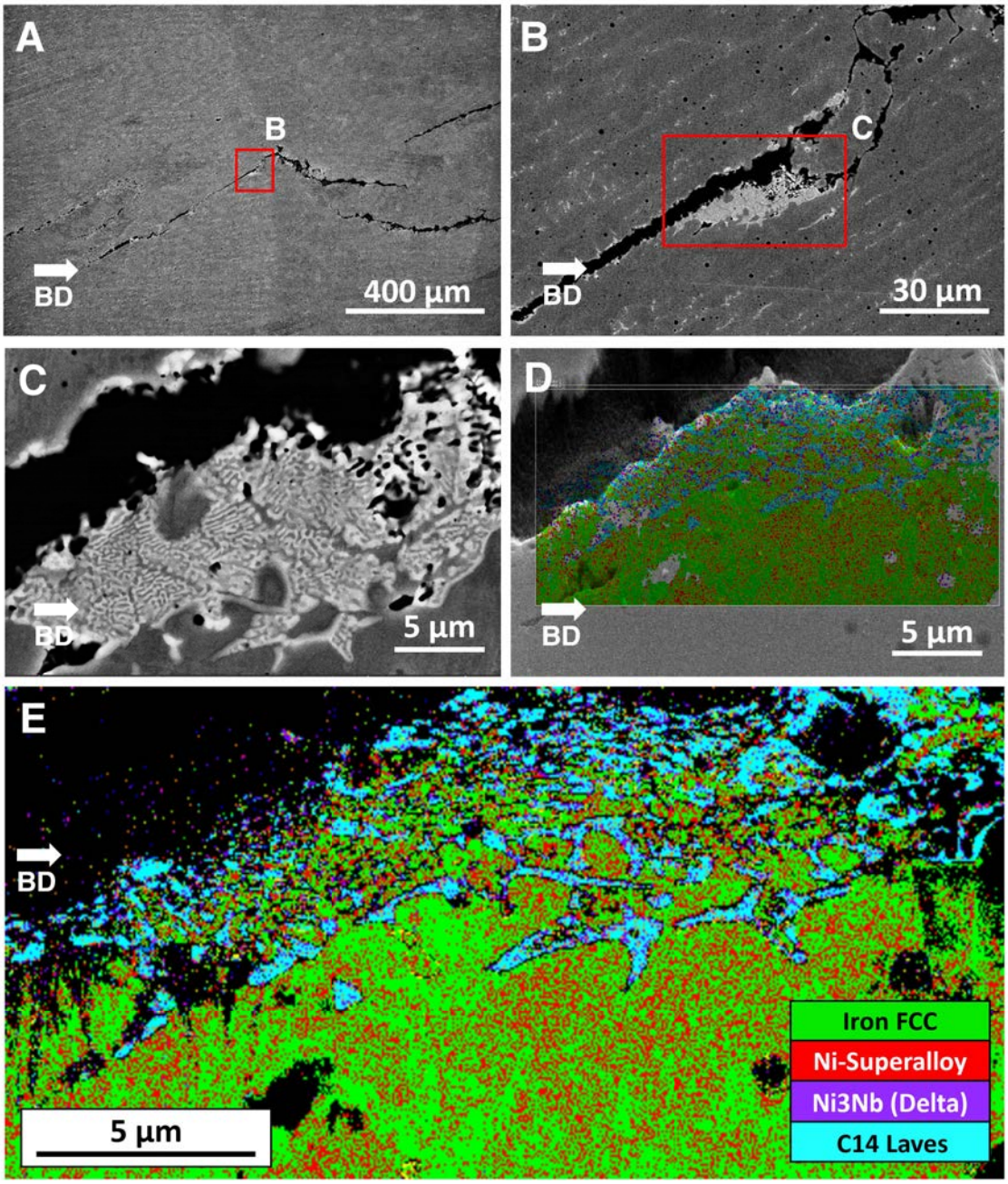

Figure 5.9: (a) SEM micrograph of a crack at approximately 15wt.% IN718 in the FGM05 sample. (b-c) Close-up, which details the eutectic microstructure. (e) EBSD phase map showcasing the different phases detected in the frame detailed in (d).

5.1.1. Solute microsegregation and micromechanical characterization

The segregation patterns and the preferred cracking path had a strong correlation. Fig 5.10 illustrates the defect propagation in a sample with a sharp transition between the two alloys. In the vicinity of this transition, pronounced microsegregation of Mo and Nb is observed, creating preferential paths along which the defect propagates more easily.

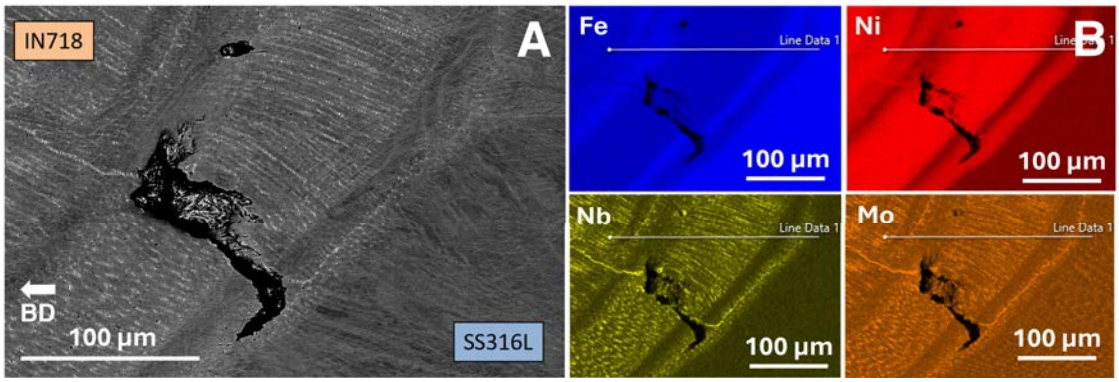

Figure 5.10: (a) SEM image of a defect propagating. (b) EDX maps show the different composition layouts.

To correlate microstructure and micro-scale properties with solute segregation and its potential impact on cracking mechanisms, we performed EDX chemical analyses, as well as nanohardness mapping next to different crack tips within the gradient. The results are illustrated in Fig. 5.11 for the representative FGM05 sample at approximately 15 wt.% IN718. The greatest extent of segregation was found for Mo (b2, c2) and Nb (b3, c3). Notably, the location of crack tips, marked with white arrows in Fig. 5.11, corresponds to the relatively high segregation of Nb and Mo.

The correlation between nanohardness maps and segregation maps in Fig. 5.11 is present but not clear from simple visual inspection, likely because the crack in this region affects the local hardness distribution.

To further ascertain this correlation, a similar analysis of a different non-cracked area at 75 wt.% IN718 was performed, as shown in Fig. 5.12. There, the high segregation and its correlation with high hardness values are clear. Overall, areas showing enhanced Nb content (up to 19.77 wt.%) and Mo content (up to 8.16 wt.%) demonstrate higher nanohardness values (up to 11.9 GPa) compared to the matrix (4.7 GPa).

To quantify the spatial correlation between hardness and microsegregation maps, we calculated the Structural Similarity Index Measure (SSIM) [176], which is appropriate for comparing the spatial patterns of fields that may be nonlinearly related. Figure 5.13 shows the maps used to calculate the correlation, i.e. the SSIM, between nanohardness and the concentration maps of Mo and Nb. On the region delimited by the dash-dotted line in Fig. 5.12, the SSIM between hardness and Nb concentration is 0.71, and the SSIM between hardness and Mo concentration is 0.81, thus highlighting the strong link between microsegregation and local mechanical properties.

The presence of cracks in highly segregated regions, which relates to heterogeneous mechanical properties, provides a potential underlying mechanism for the emergence of cracks.

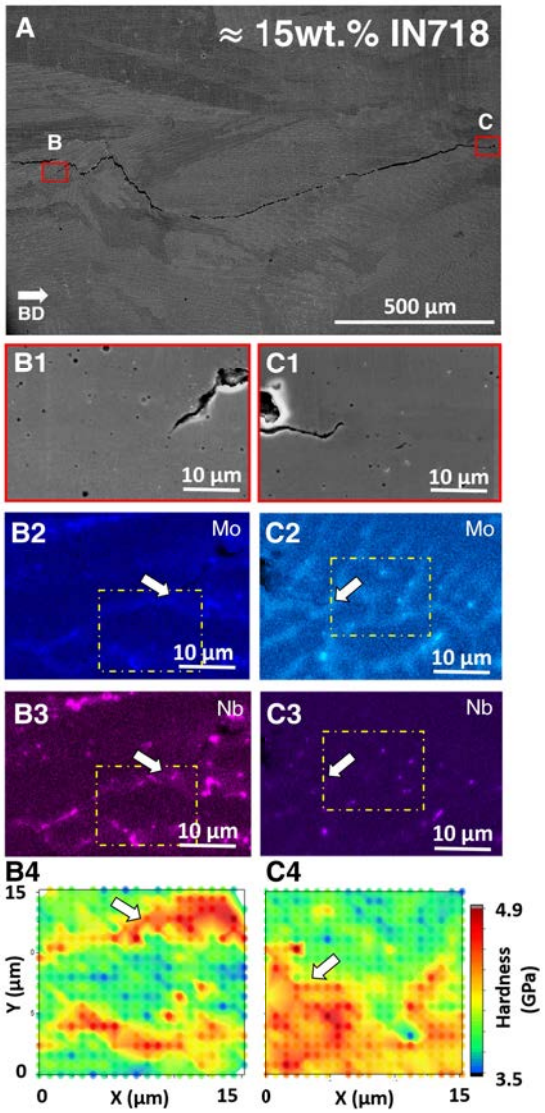

Figure 5.11: (a) SEM image of an intergranular crack propagating in the build direction located approximately at 15 wt.% IN718 within the gradient of sample FGM05. Images (b1-c1) show close-ups of each crack tip, further analyzed in terms of EDX analysis in (b2-c2) for Mo and (b3-c3) for Nb chemical patterns. Within EDX accuracy, the max and min values of composition in these images are 0.08-4.2 wt.% for Mo and 0.03-9.3 wt.% fro Nb. (b4-c4) Nano hardness maps at the same location for both crack tips.

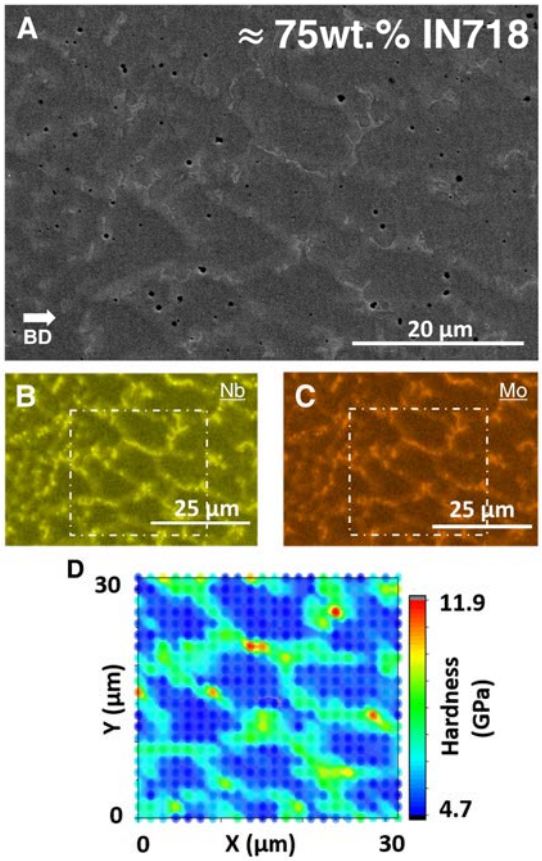

Figure 5.12: (a) SEM image at 75 wt.% IN718 within the gradient. Images (b-c) show EDX analysis for Mo and Nb respectively. Within EDX accuracy, the max and min values of composition in these images are 2.73-8.16 wt.% for Mo and 2.08-19.77 wt.% for Nb. (d) Nano hardness maps at the same location

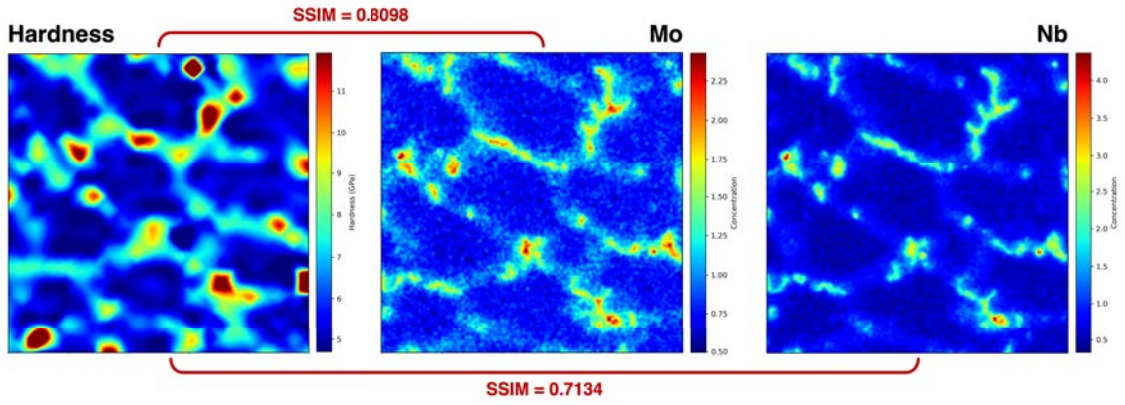

Figure 5.13: Cropped, aligned, and scaled maps of nanohardness (left) and smoothed ($\sigma = 3.0$) EDX maps of Mo (center) and Nb (right) concentrations, used to calculate the Structural Similarity Index Measure between hardness and species concentration.

5.1.2. X-Ray Diffraction

We performed XRD analyses to better identify different phase evolution or lattice distortion along the gradient. When analyzing the different XRD spectra throughout a graded sample (e.g., FGM05), more precisely in the gradient region (Fig. 5.14), FCC peaks are present along the entire area. Some of these peaks appear with different levels of intensity depending on the layer, with no clear signs of any other intermetallic phase (e.g., Laves phase) depicted before. Peak height and broadening vary between compositions, hinting at different stress/strain scenarios. When using the Cr-source X-Rays to obtain residual strain measurements (Fig. 5.15), we could identify a slight correlation between stresses and wt.% IN718. Overall, lower values of compression stresses seem to appear at higher contents of IN718. The steep increase in microstress at the initial stages of the gradient can be linked to the crack location, where stresses are alleviated.

5.2. Macroscopic mechanical characterization

Microhardness along the gradient

Fig. 5.16 shows the evolution in microhardness along the entire gradient region of the sample for the three main sample configurations, namely FGM05, FGM10, and FGM20. Overall, the average HV values for pure IN718 and 316L remain similar and consistent with the literature. The fluctuations in measured hardness values are within expectation, due to microstructure inhomogeneity, since we used an indent of size $\approx$ 35 to 40 µm, which is larger than the typical microstructure length scale (see, e.g., dendritic spacing of a few micrometers in Fig. 5.8). Keeping in mind that each gradient has a different length, and even though the transition is

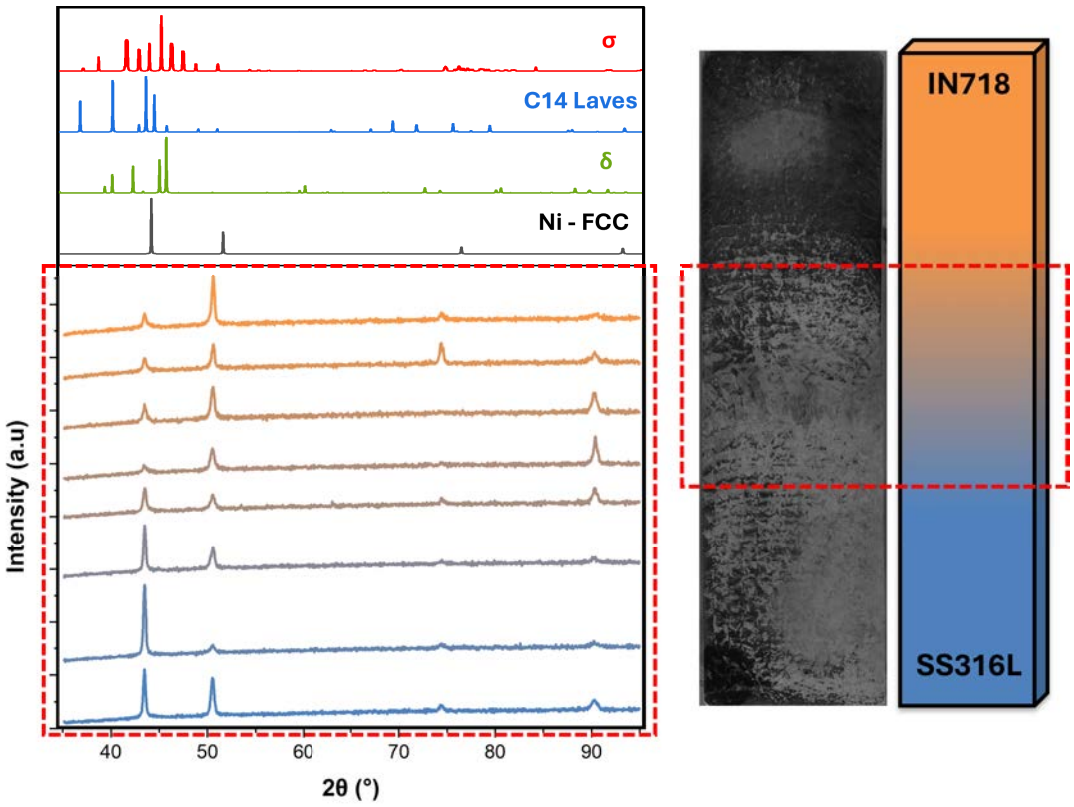

Figure 5.14: Batch XRD analysis at different layers of the FGM05 sample.

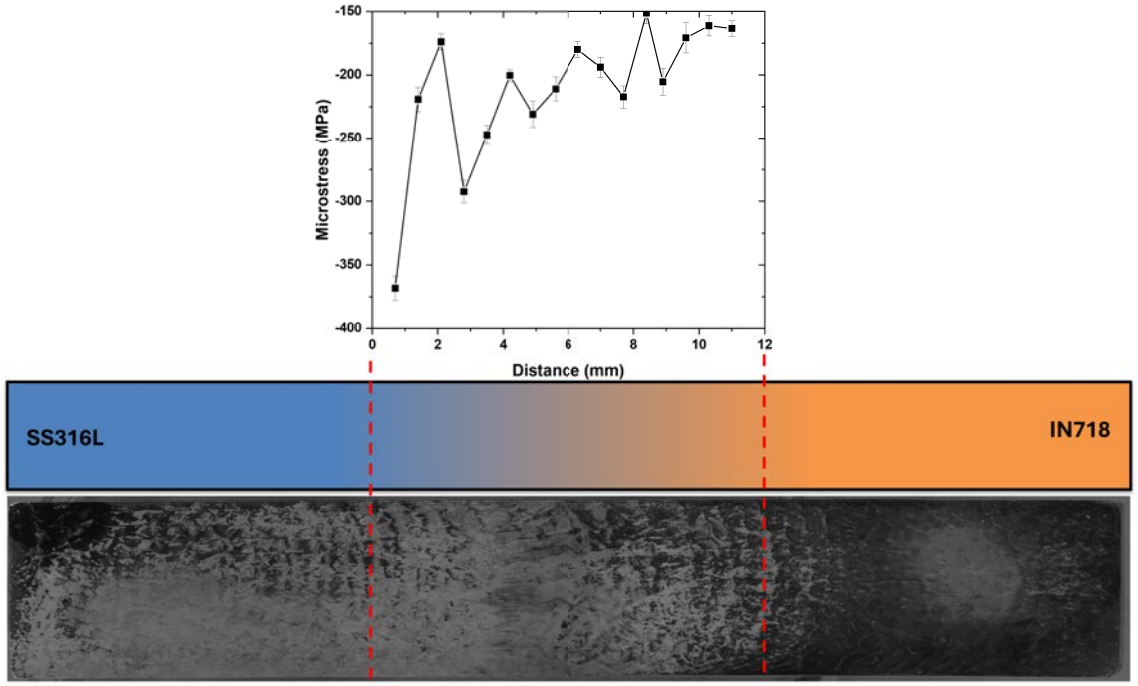

Figure 5.15: Microstrain measurements along the graded region of the FGM05 sample.

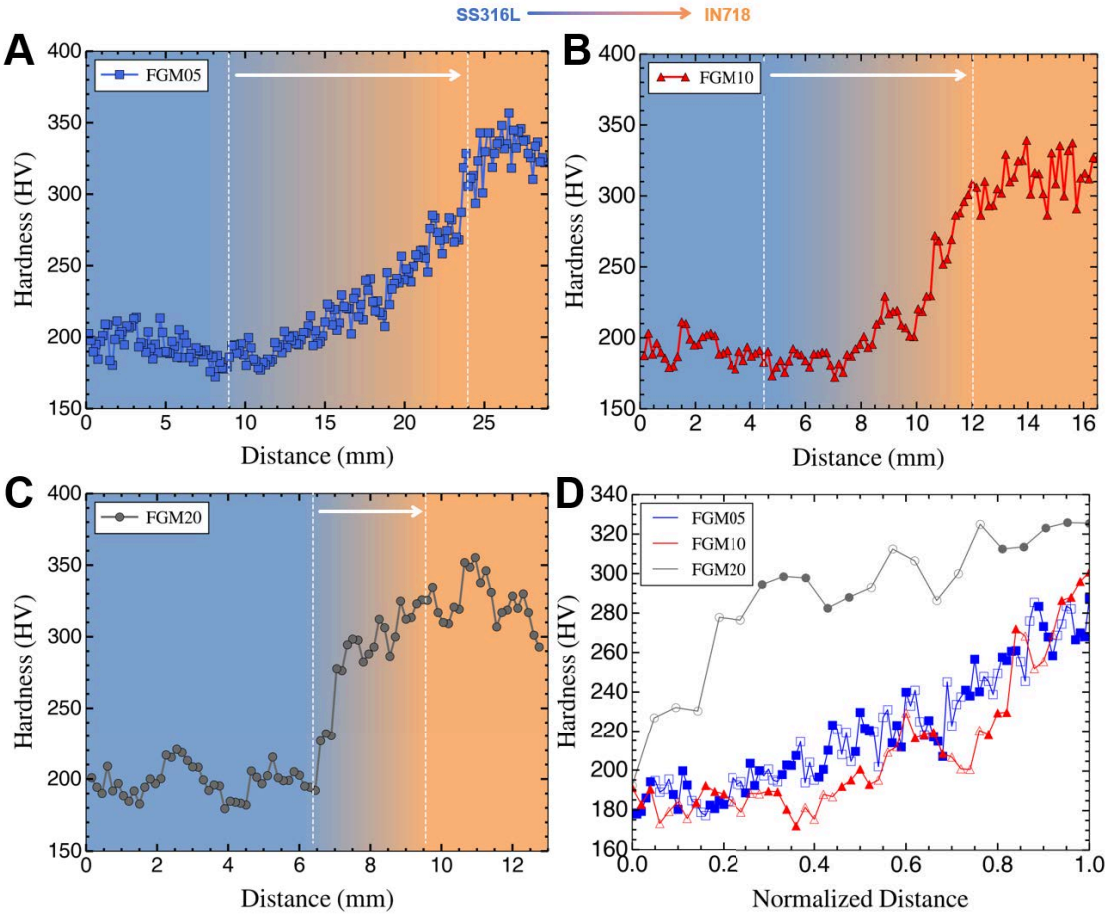

Figure 5.16: Microhardness profiles along the (a) FGM05, (b) FGM10, and (c) FGM20 samples, and (d) superimposed curves as a function of the normalized length between 316L ($x = 0$) and IN718 ($x = 1$). Horizontal arrows in panels (a)-(c) mark the graded region. In panel (d), symbols alternate between filled and open with each change of composition (i.e. with each layer).

relatively smooth and gradual in all cases, different behaviors emerge. As illustrated in Fig. 5.16(d), the microhardness across FGM05 and FGM10 samples is more linear than that in the FGM20 sample. The latter exhibits a relatively steep increase in microhardness across the layer at 20 wt.% IN718 (i.e. at a normalized position $0 \leq x \leq 0.2$), resulting in a relatively higher overall strength over the graded region. It is counterintuitive, as one might expect that a steep gradient in mechanical properties would make the sample more prone to internal stresses and hence defects, while the FGM20 microstructure, in fact, exhibits the lowest density of cracks.

Compression tests along the gradient

Results of compression experiments are presented in Fig. 5.17 in the form of true stress-strain curves obtained for cylindrical specimens extracted at different points in the as-printed pillars. The overall stress-strain results for pure IN718 and pure

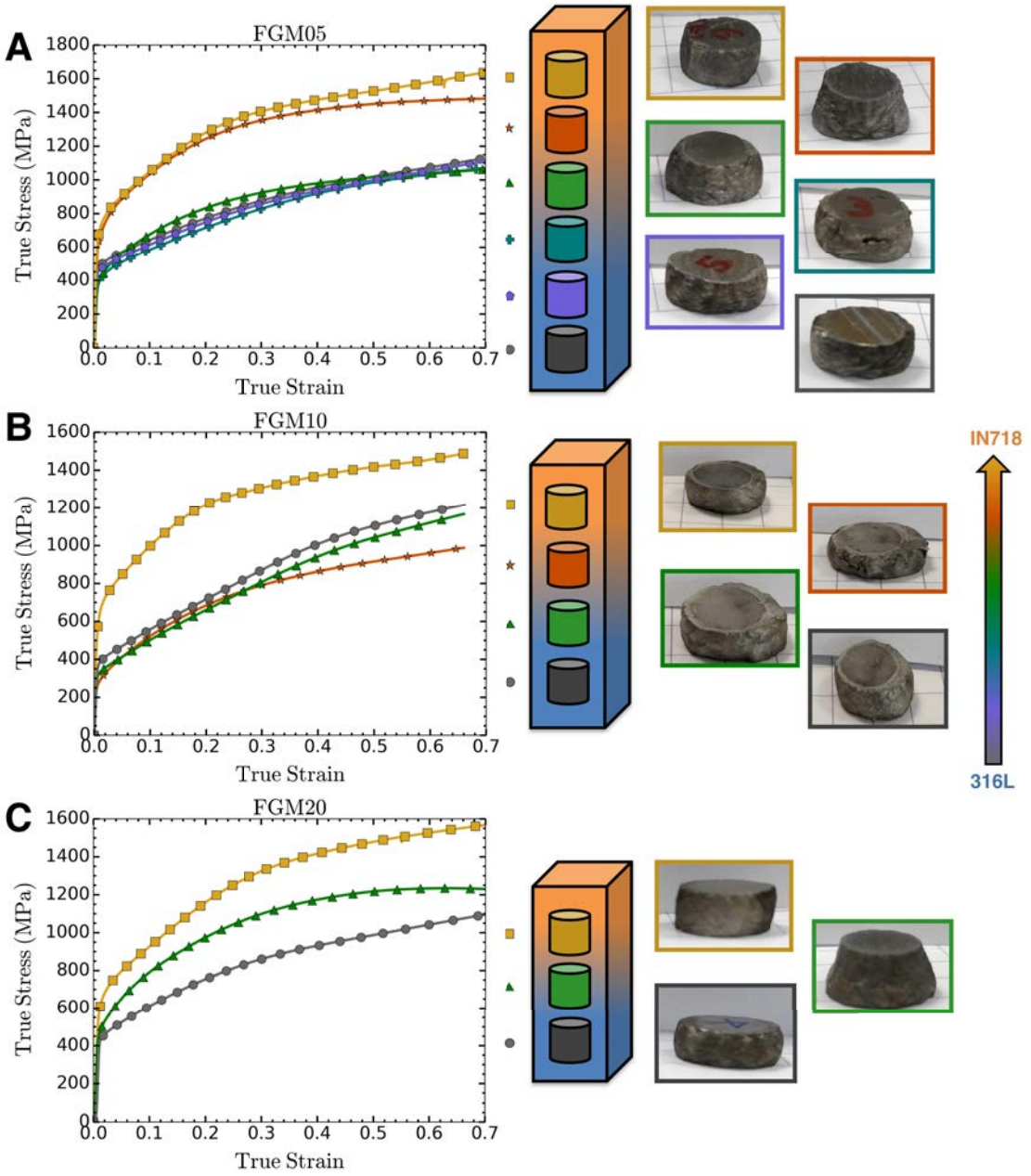

Figure 5.17: Compression curves of selected samples extracted from the graded samples FGM05 (a), FGM10 (b), and FGM20 (c) according to the schematic at the bottom, next to pictures of each sample after testing. The left column shows a schematics of approximately where the samples were extracted in the gradient region, next to pictures of each sample after testing.

316L are consistent with expected results from the literature with higher values in IN718-rich regions of the sample. Progressive grading strategies (FGM05 and FGM10) exhibit a bimodal distribution of behaviors, where most of the gradient region behaves similar to the weaker material (namely 316L) with a sudden jump from 316L-behavior to IN718-behavior. In contrast, for a steeper gradient (FGM20), the behavior is intermediate between that of the two end alloys, and the deformed

specimen also shows a clear gradient of deformation — i.e. of mechanical strength — across the sample. Since the deformed samples do not exhibit any visible shear cracking, we consider that the effect of cracks was relatively minor. However, it cannot be completely discarded as a potential cause for the different behaviors observed in sample FGM20 compared to FGM05 and FGM10.

5.2.1. Dilatometry at different concentrations

Complementary to analyzing the mechanical properties and trying to shed some light on what might be the reason behind cracking, we also checked the thermal expansion behavior, simulating how different composition mixtures might perform. Fig. 5.18 shows the change in CTE along a theoretical gradient — i.e. each measurement using a sample with one given fixed mixture of alloys — between the two alloy systems. The error bars represent the dispersion over three test for each composition, and results are compared with our CalPhaD calculation, and with literature values for the two end-point alloys. Both measured and calculated values exhibit a gradual change of CTE across the gradient. Experimental data agrees well with the theoretical values for pure 316L and IN718, showing an nearly linear variation along the gradient, while CalPhaD shows a more significant discrepancy at lower IN718

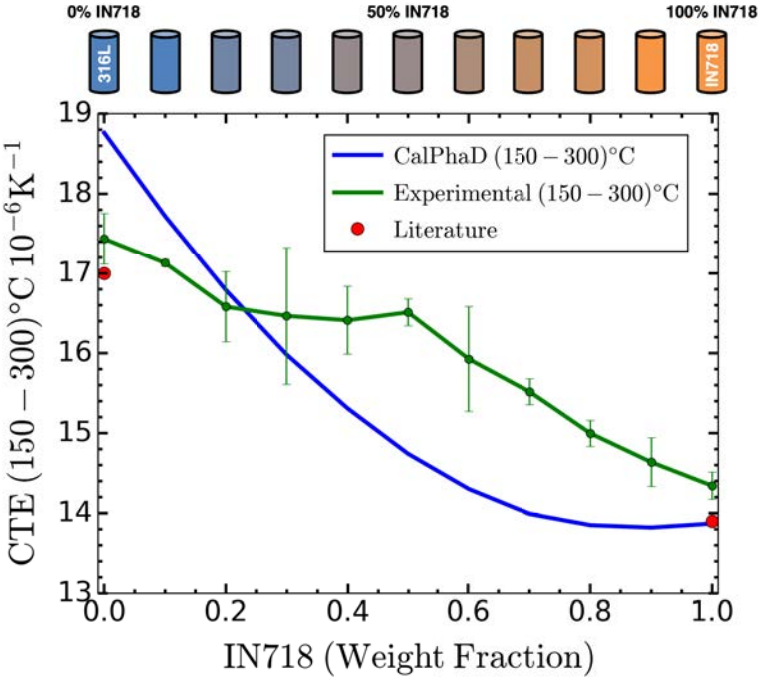

Figure 5.18: Comparison between theoretical (CalPhaD) and experimental CTE evolution along the gradient. Dilatometry experiments used sample with a fixed alloy mixture (i.e. fixed composition) representative of different steps in the gradient. Error bars show the dispersion among three different tests for each composition. (Note that the error bar at 10% IN718 is narrower than the symbol size.)

content. This discrepancy is attributed to the CalPhaD-calculated values, which were obtained within the temperature range between 150 and 300°C considering full equilibrium phase content, while the DED-printed samples are likely to exhibit some deviation from equilibrium microstructures. Still, the difference between calculated and measured values remains below 11%, which is satisfactory. A priori, the absence of a steep jump in CTE across the gradient would tend to discard the hypothesis of CTE mismatch as a major source of defects such as cracks.

5.3. Physical Simulation

To test the viability of the Gleeble procedure and to further explore the compatibility of alloy systems, we used the setup detailed in Fig. 4.14. With the idea of only melting the lowest T_m alloy (IN718), a heating rate was designed, and compression forces were applied to the rods to compensate for thermal expansion and maintain a good contact surface between rods (seeking good electrical contact). After several failed attempts to keep contact between the thermocouples and the IN718 rod when it melts, cemented joints had to be used. After the thermal procedure, a sound joint was obtained, with some Tungsten residue joined at the molten area, which was easy to grind (Fig. 5.19).

After grinding and polishing, the samples were studied at the optical microscope (Fig. 5.20). Optical imaging with polarized light shows different grain structures, with equiaxed polygonal grains in the 316L steel and columnar grains in the IN718.

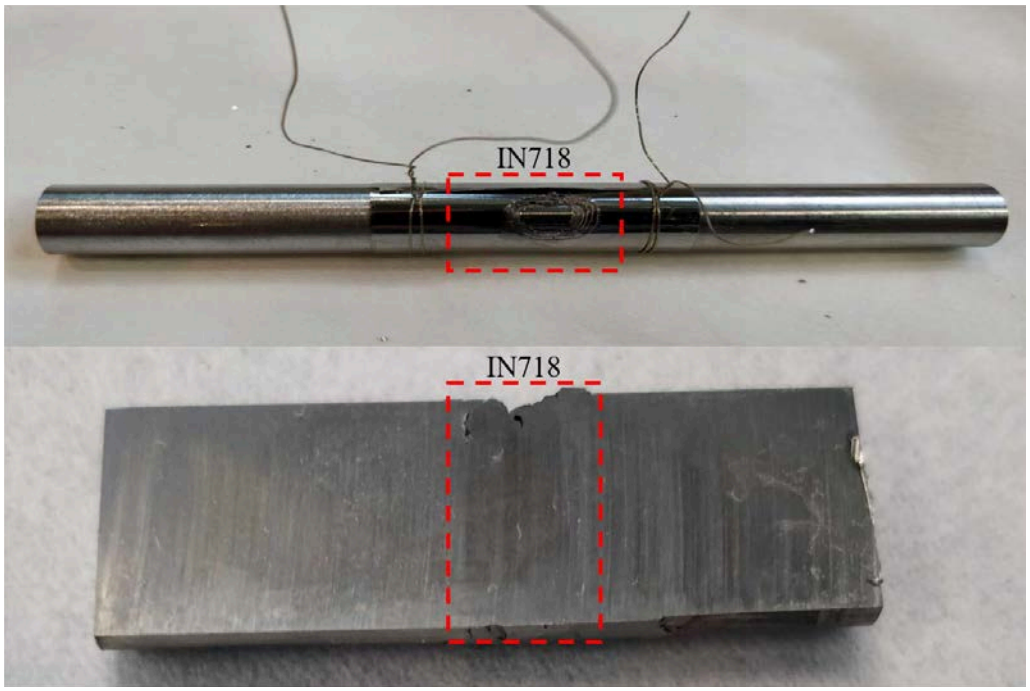

Figure 5.19: Initial setup. A cavity was ground in the middle of the Tungsten foil to fit the thermocouples.

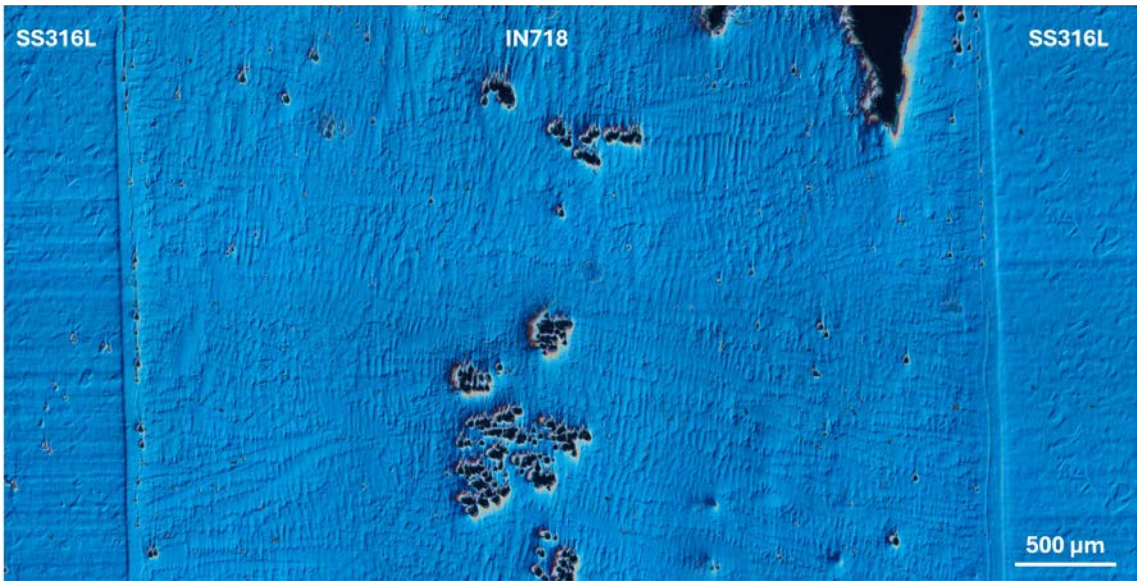

Figure 5.20: Optical micrograph of the Gleeble sample cross-section, where alloys and microstructure morphologies can be seen.

Here, we can also observe dendritic growth following the sample axis, which corresponds to the direction of the heat flux from the molten section through the 316L rods toward the cold Cu grips.

A consistent morphology throughout the cross-section is visible when observing both materials' interfaces. There is a vertical line of pores, which, depending on the section, vary in size and in distance between them, and an intermediate zone (close to 65 µm in width) where interdiffusion takes place. For further understanding, EDX analysis was performed (Fig. 5.21). EDX analysis shows coherent results compared to the estimated compositions of each alloy, with a sharp boundary between one composition and the other (related to the interdiffusion zone seen in the optical micrographs). Precipitants can cause peaks in the content of Nb and Mo, as we could observe in the FGM samples, also following similar segregation patterns.

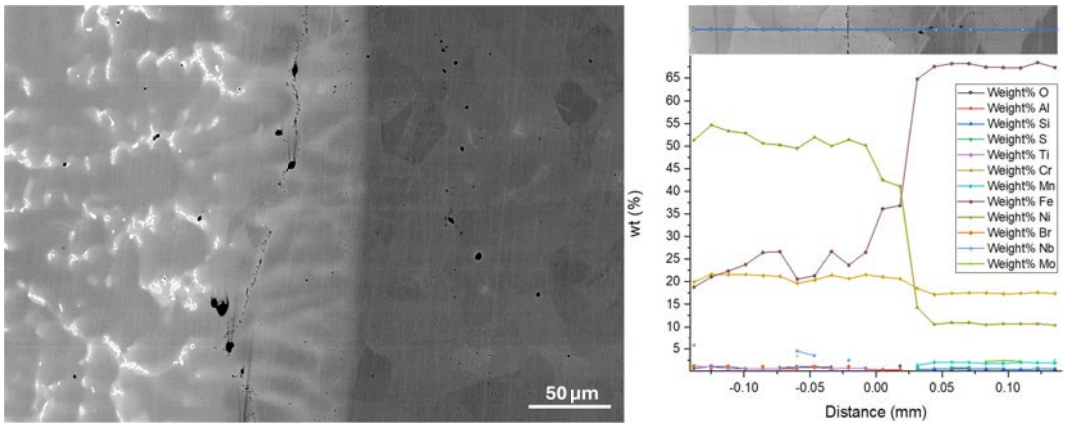

Figure 5.21: SEM image and composition across the interface measured by EDX.

5.4. Computational Thermodynamics (CalPhaD)

5.4.1. Binary and ternary diagrams

The primary purpose of the CalPhaD calculations is to explore the range of stability of potential detrimental phases or solubility gaps in the multidimensional composition-temperature space. As a first step, relevant Fe-based binary diagrams are shown in Fig. 5.22. The Fe-Ni system (a) is the most relevant binary system between Fe-based and Ni-based alloys, both of which share an FCC-γ structure for a broad range of temperatures across the entire Fe-to-Ni composition range. The Fe-Cr diagram (b) exhibits a region of stable σ phase at ranges close to the nominal composition of both alloys (17 wt.% for 316L and 18.31 wt.% for IN718), while Fe-Mo (c) and Fe-Nb (d) diagrams exhibit intermetallic phases such as C14 Laves,

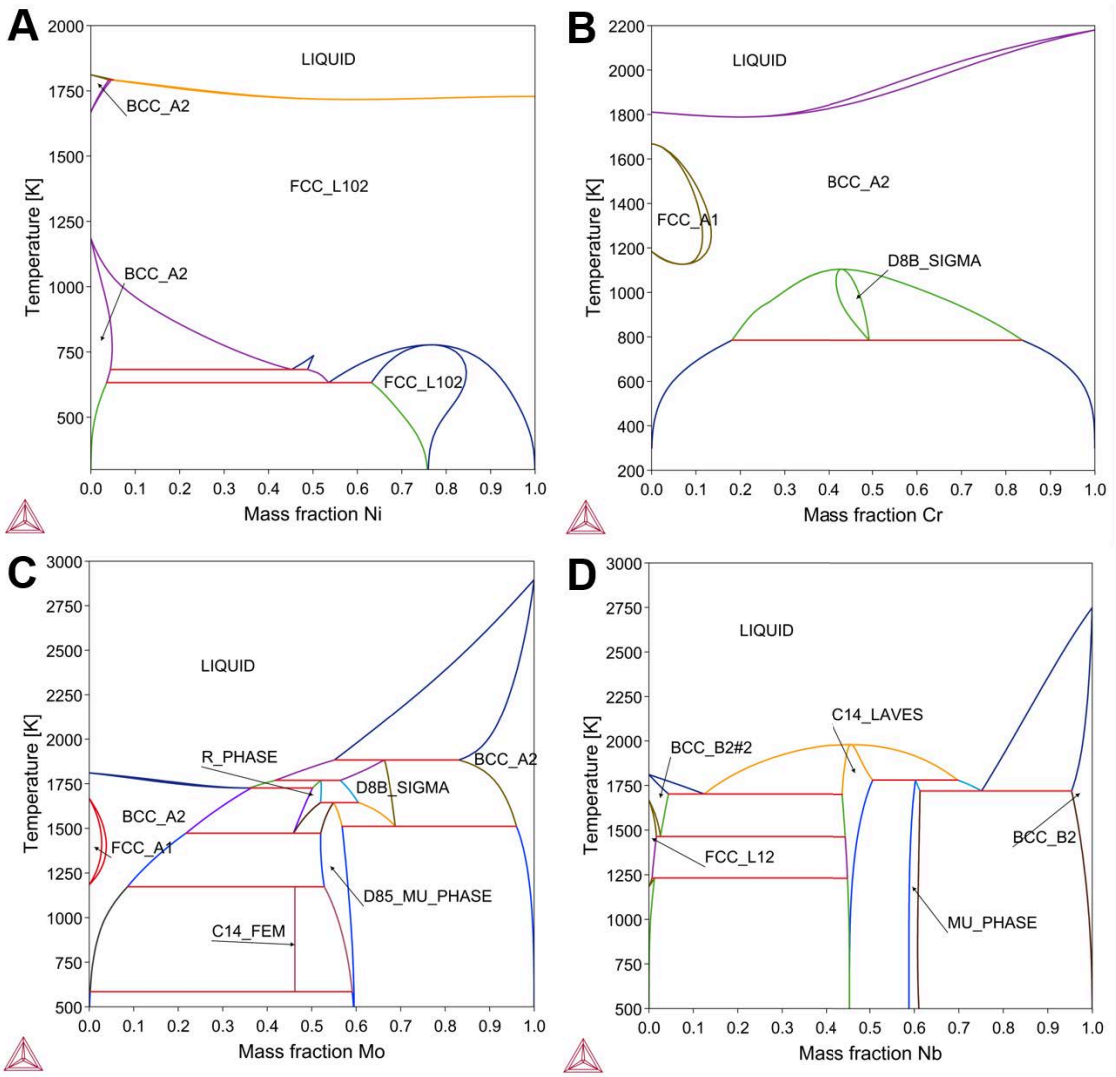

Figure 5.22: Binary phase diagrams for the (a) Fe-Ni, (b) Fe-Cr, (c) Fe-Mo, (d) Fe-Nb systems.

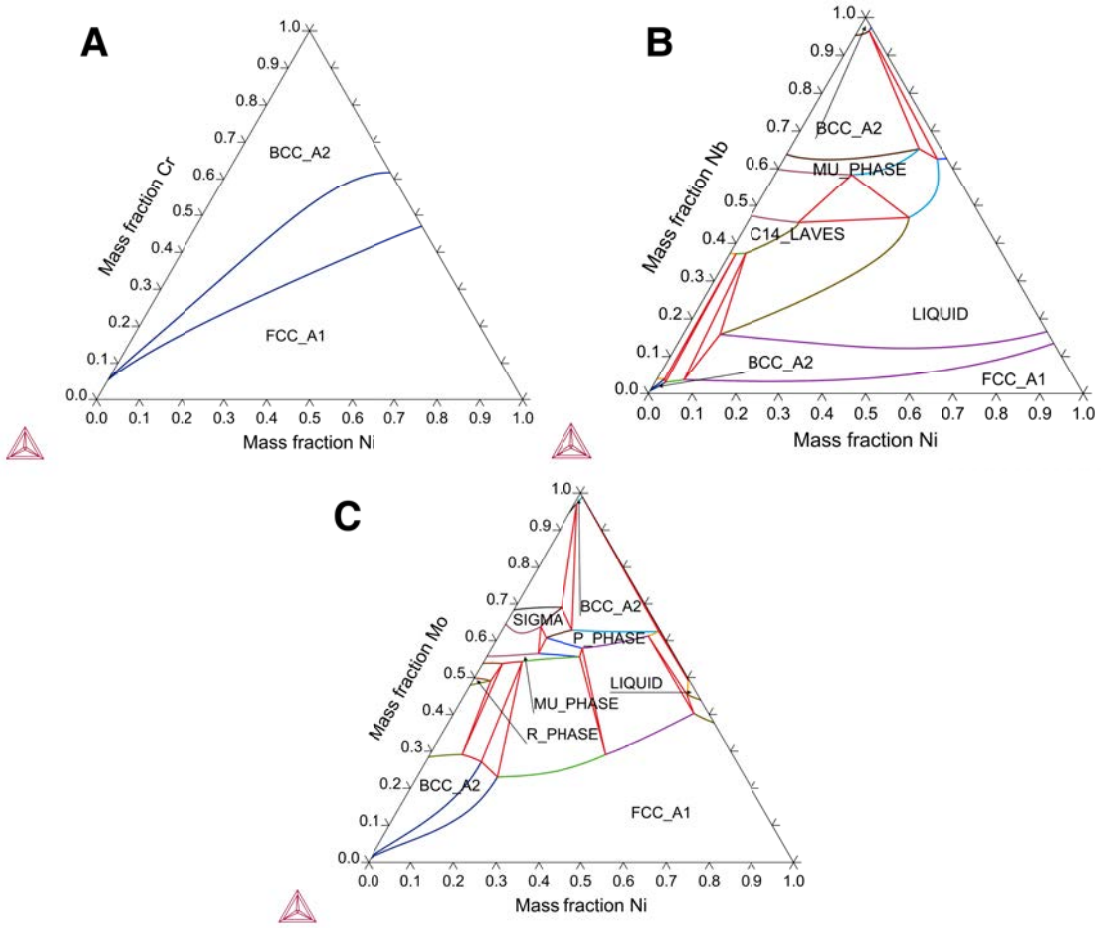

Figure 5.23: Ternary phase diagrams at 1600 K for the (a) Fe-Ni-Cr, (b) Fe-Ni-Nb, (c) Fe-Ni-Mo systems.

μ, and R-phase.

Ternary Fe-Ni-based diagrams, calculated at a temperature of 1600 K close to the solidus for most of the intermediate compositions in the gradient, appear in Fig. 5.23. The addition of Cr (a) does not show any intermetallic through the transition from FCC to BCC. In contrast, the addition of Nb (b) or Mo (c), previously shown as highly segregated elements (Figs. 5.11-5.12), exhibit a broad range of intermetallic phases, such as C14 Laves, σ, and μ.

5.4.2. Isopleth SS316L-IN718 diagram

In Fig. 5.24a, we plot an equilibrium composition-temperature phase diagram along the multicomponent (isopleth) hyperplane going from 316L to IN718.

Notably, it contains a broad region of stability for C14 Laves phase below 1300 K primarily in the 316L-rich half of the composition range, while the same temperature range exhibits a stable δ region in the IN718-rich half of the composition range. At about 1200 K and below, σ is also stable across the entire composition range.

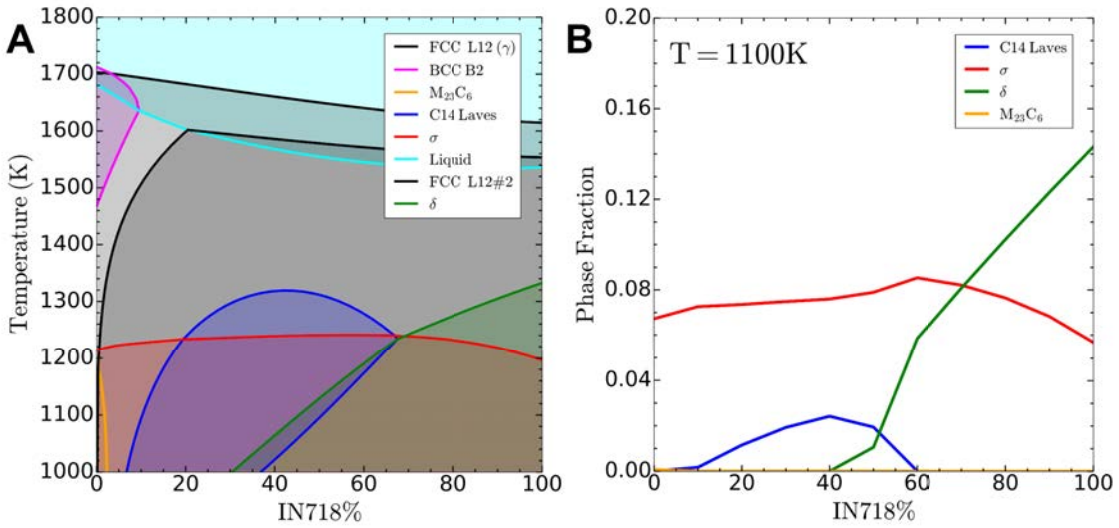

Figure 5.24: Analysis of equilibrium phase diagram isopleth section along the 316L to IN718 gradient path. (a) Phase diagram along the composition range from 316L to IN718 (ThermoCalc, TCFE9). (b) Phase fraction of secondary phases of interest along the composition space at 1100 K.

This is an indication that C14 Laves and δ might be the first intermetallic to form across most of the composition range, which is consistent with their presence in the analyzed microstructures (Fig. 5.9). These two phases are part of a family of structures called TCPs (topologically close-packed phases) [134]. These phases, rich in refractory elements, have complex crystallographic structures, not coherent with the matrix, which are characterized as close-packed layers of atoms [132]. σ has a tetragonal structure with a typical FeCr, FeCrMo or CrCo formulation, while C14 Laves has an hexagonal structure, with a typical $(Fe,Ni,Cr)_2(Nb,Mo,Si)$ formulation (see Table 4.2). In both cases either Mo and or Nb may be present.

Along the same 316L-to-IN718 composition line, Fig. 5.24b shows the fractions of phases at a temperature $T = 1100$ K. This plot shows that, at this temperature, the fraction of σ phase is expected to be high (in spite of it not appearing in the observed microstructures, Fig. 5.9), while a small amount of C14 Laves is present in the 316L-rich alloy, which is replaced between ≈ 40 to 60 wt.% IN718 by an amount of δ phase increasing as the alloy gets closer to IN718. A potential key role of the C14 Laves phase is suggested by the fact that it appears between 10 and 30 wt.% of IN718, i.e., in the composition range exhibiting cracks, while it is mostly absent elsewhere (including in the full 316L alloy, which is printable without such defects under similar printing conditions).

5.4.3. Solidification paths

We also calculated solidification paths, namely using a lever rule (equilibrium) or Gulliver-Scheil model, for compositions along the gradient, namely for 316L-

x wt.% IN718 with $x = 0$ to 100 by steps of 10.

Fig. 5.25 shows the evolution of phase fraction with temperature for specific composition steps in the gradient, keeping full equilibrium (Lever rule) conditions. Solidus and liquids temperatures follow a steady trend as they decrease with the content of IN718. The most prevalent matrix throughout the gradient is FCC-γ, with some minor fraction of δ-ferrite at a higher content of SS316L. Fig. 5.25 also shows the evolution of some other phases, previously targeted as detrimental. σ phase remains overall constant along the gradient while other phases, like δ or certain carbides, increase (related to the amount of Nb in the mix) or decrease respectively with the amount of IN718. C14 Laves, identified in the EBSD analysis, were also present in the simulations at specific temperature ranges, peaking at approximately 20 to 30 wt.% IN718. The occurrence of this phase extends between from 10 to 60 wt.% IN718, coinciding with the results observed with the printed pillars.

These plots are very informative but also somewhat hard to read and interpret as they are. In order to simplify/summarize them, we plot the maximum value of a phase fraction along the entire temperature range (corresponding to the final value for Gulliver-Scheil, but not necessarily for a lever rule) along the composition gradient in Figure 5.26. In these graphs, we only plot the secondary phases, i.e. filtering out the liquid, fcc, and potential bcc phases. Doing so provides a "worst case scenario" for the formation of secondary undesired phases. Both models agree qualitatively on the presence of most phases, like C14 Laves, σ, δ, and to a lower extent μ, as well as several intermetallic phases that vary in identity and amount between the two models.

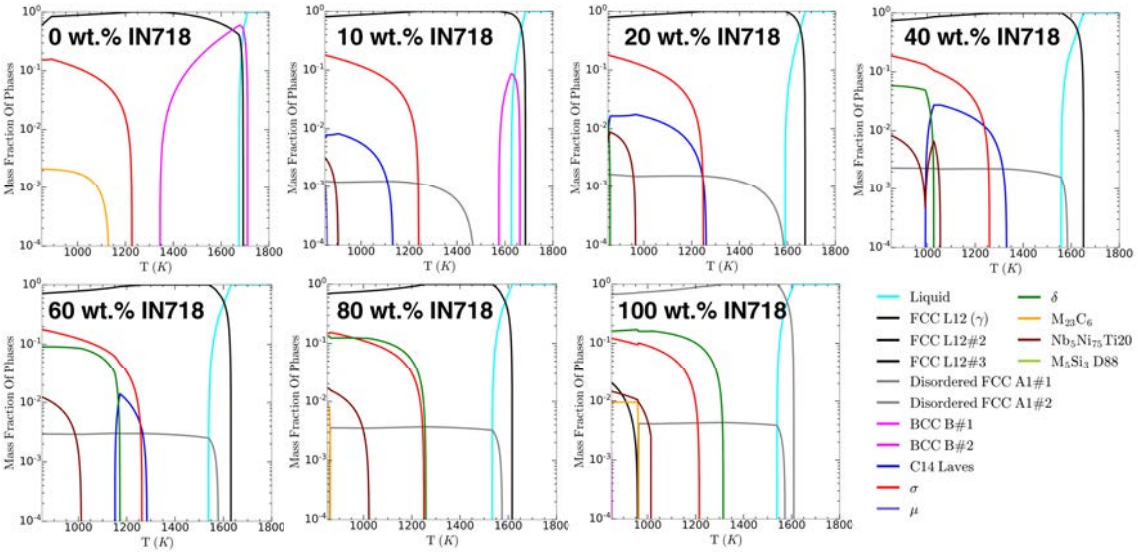

Figure 5.25: Fraction of phases as a function of temperature alongside the FGM (Lever).

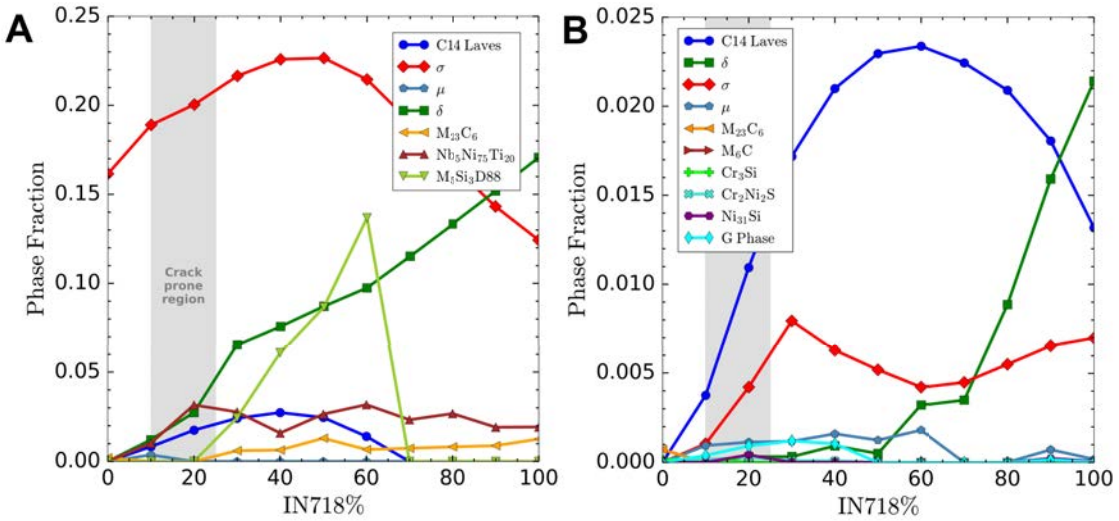

Figure 5.26: Results of solidification paths for starting compositions along the SS316L to IN718 gradient path, showing the maximum phase fractions for secondary phases (i.e. excluding liquid, fcc, and bcc phases) along a (a) lever rule or (b) Gulliver-Scheil solidification path.

5.4.4. Cracking susceptibility

As mentioned in previous chapters, solidification cracking is a major underlying mechanism for the emergence of defects in graded materials.

Using the Gulliver-Scheil calculations described above, we extract the freezing range and the $f_s(T)$ curves in order to calculate the CSI from Eq. (3.3), for compositions along the gradient. Results, displayed in Fig. 5.27, show how the values of CSI at any point of the gradient are higher compared to both initial alloys, peaking at 20 to 40 wt.% IN718. Overall, the highest values of both CSI and freezing range being slightly skewed toward the SS316L half of the gradient qualitatively agree with the region where cracks are present in the samples. The endpoint values from each alloy increase steeply when mixing alloys, especially when adding some IN718 to the 316L, correlating with the cracking behavior analyzed in the printed samples. The overall region where we find the highest values of CSI (approximately 20-40 wt.% IN718) is close to where cracks are found in the samples. Compared to the freezing range, both show a similar tendency up to 40 wt.% IN718, above which the CSI decreases at a higher rate. It has been stated [159] that the freezing range is an important factor when discussing solidification cracking, as this increases when increasing this range. Concentrations close to 40 wt.% of IN718 have as high freezing range as 50 wt.%, but higher overall CSI, which might be promoted by more segregation and formation of intermetallic phases.

Correlation between crack propagation, dendritic microstructure, CSI, freezing range, and chemical gradients from EDS analysis hints at the idea that solidification

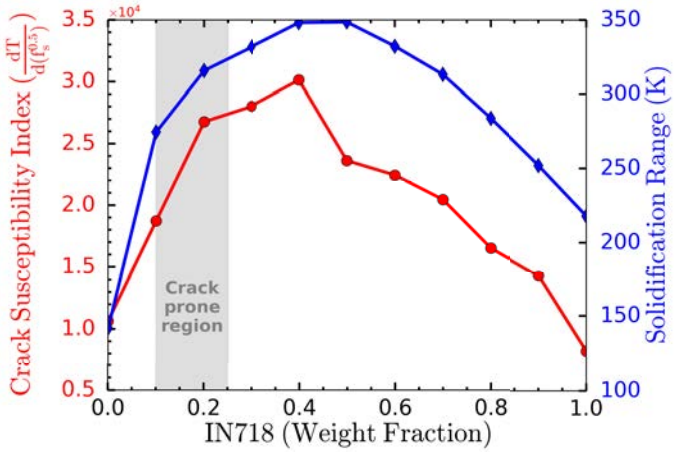

Figure 5.27: Crack susceptibility index (CSI) obtained using the Kou criteria coupled with Gulliver- calculations along the entire solidification range of the graded area. The freezing range was also obtained from the same thermodynamic simulations.

cracking is behind the defects in the samples. Welding studies state [150] that hot cracking in stainless steels is often caused by low-melting eutectics, which contain segregated impurities of elements like Nb, which further supports this theory. For this reason, and to further interpret the differences between CSI values in Fig. 5.27, we also analyze the elemental segregation at later stages of the solidification process.

5.4.5. Solute segregation

Gulliver-Scheil data provides essential information about the segregation patterns of different elements along the f_s evolution. For these simulations, it was decided to include all elements in the composition sheet provided by the powder supplier (including Al, Co, Cu and Ta) to account for any interesting behavior, even if these elements are negligible. Fig. 5.28 shows the evolution of the most interesting elements along the mentioned f_s range for each composition. Full 316L shows fairly steady behavior, except for C, which decreases at the expense of Si, Mn, and Ni. Full IN718 also shows a steady behavior except for C at the expense of Mn and Si. As some IN718 enters the mix, the overall mass fraction of elements like Ni, Nb, Mn, Si (or Ta) increases unevenly at the expense of elements like Fe, Cr, Mo, C, Ti, (or Cu, Co, Al). Fe showcases an almost monotonic behavior along the gradient with minor content in the remaining liquid, not hinting at any suspicious segregation pattern. Conversely, Ni appears to have an abrupt increase in mass fraction when reaching values close to f_s=0.9. This behavior is similar for elements like Mo (with a steep decrease right at the end of the solidification) and especially Nb, which shows an uneven tendency ending in a steep increase at high values of f_s. This means that these elements remain segregated in big quantities in small liquid regions by the later stages of the solidification process and interact with each other, potentially

forming new phases.

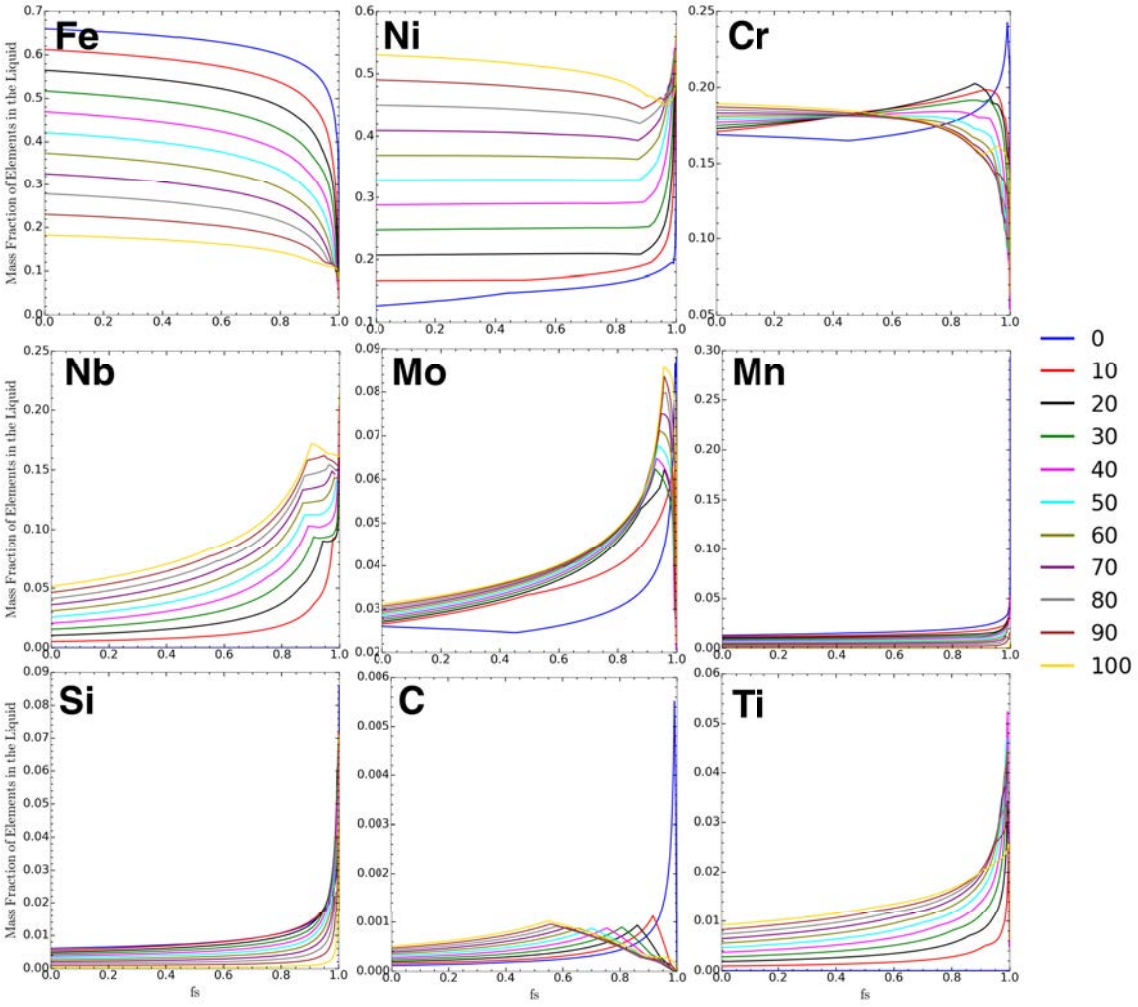

Figure 5.28: Comparative evolution of the mass fraction of different elements of interest along the solidification process. Numbers on the right describe wt.% IN718.

CHAPTER 6

DISCUSSION

All printed samples exhibited cracks ranging from about 100 µm to a several millimeters in length in the region of the gradient close to 20 wt.% of Inconel 718 alloy. Since the thermal properties of both alloys are close, and because the printing conditions (e.g. layer height) are the same for all samples, we consider that the thermal history experienced by each sample is consistent. For this reason, we looked for crack causes rooted in the compositional region explored along the gradient, rather than thermo-mechanical causes (e.g. thermal cycling and resulting stresses).

The change in macroscopic properties across the gradient, such as hardness (Fig. 5.16) and thermal expansion coefficient (Fig 5.18), are relatively smooth and close to linear, with the exception of a steep hardness increase localized closer to the 316L-rich end of the FGM20 sample, resulting in a higher average strength of the gradient. Compression tests (Fig. 5.17) also revealed that lower grading steps (samples FGM05, FGM10) resulted in overall properties closer to the weaker alloy (316L), while results for the steeper gradient (FGM20) indicate a more progressive change in properties with intermediate behavior in the graded region. The greater mechanical properties in the FGM20 sample are consistent with its lower density of defects, in particular cracks (Fig. 5.6). These results seem to indicate that the underlying mechanism for the emergence of cracks is not a steep jump in thermophysical properties, such as CTE, through the gradient, as is often reported in FGMs [137], but rather from mechanisms rooted at lower scales. These results are consistent with previous studies, who already suggested that the mismatch in thermo-mechanical properties, which was identified as the main cause for cracking in sharp multi-material samples [40, 117, 178, 182], was not the main underlying mechanism in progressively graded samples, where the residual stresses are smoothed over the gradient [62].

Indeed, microstructural and micromechanical analyses reveal strong elemental segregation, in particular of Nb and Mo species (Figs 5.11-5.12). Segregation and nanohardness maps show a clear correlation between Nb and Mo local concentration

and mechanical properties (Figs 5.11-5.12). Moreover, the cracked regions seem to correspond to relatively high segregation of Mo and/or Nb. Microstructural analysis also reveals the presence of secondary intermetallic phases, such as C14 Laves and δ, in cracked regions (Fig. 5.9). This is consistent with results from thermodynamic calculations (Figs 5.24-5.26), which also suggest the possible formation of σ phase. Gulliver-Scheil simulation indeed exhibit greater amounts of C14 and δ, which are expected to form at higher temperature than σ, while lever rule calculations result in greater amounts of σ across the composition gradient range (Figs 5.26). The absence of a notable σ phase in our samples might be explained by the fact that C14 (for 316L-rich) or δ (for IN718-rich) phases forming first have already consumed a great amount of solute segregated in the liquid phase to hinder the formation of σ. It might also be due to a potentially slower kinetics of nucleation and/or growth of the σ phase compared to C14 and δ.

The use of a simple crack sensitivity criterion (Fig. 5.27) also correlates reasonably well with the region of presence of the crack. The overall region where we find the highest values of CSI (approximately 20-40 wt.% IN718) is where cracks seem to form in the samples. The highest freezing range, which is also known to correlate with solidification defects, appears at a slightly higher alloy mixture, namely close to 50 wt.% of each alloy. It should be noted that the crack susceptibility criterion considered here only accounts for hot cracking based on the CalPhaD-calculated solidification path and hence neglects the potential effect of thermal stresses during the process. Still, a recent study considering five such cracking criteria on a broad range of FGM combinations (including SS304L-to-IN625, SS316L-to-Ni20Cr, and SS304L-to-Ni20Cr) revealed that Kou's criterion was reliable to predict the composition ranges of experimentally observed cracking [189].

These analyses suggest that solidification and liquidation cracking are responsible for the defects observed in our samples. Our observations and interpretations are consistent with the recent study on hot cracking in graded 316L-IN718 samples, which suggested that cracks were caused by the formation of low-melting eutectics [62]. As we could not identify any prominent oxides, carbides, or major microstructural transition (e.g. no CET), our results also tend to discard these as the causes of cracking [82, 186].

This is consistent with previous welding studies [150] suggesting that hot cracking in stainless steels is often caused by low-melting eutectics, which contain segregated impurities of elements like Nb.

To support our interpretation that Nb/Mo segregation is responsible for the formation of C14 Laves, we plot in Fig. 6.1 the segregation profiles for Nb and Mo resulting from Gulliver-Scheil calculations at different compositions along the 316L to IN718 gradient.

Results for all elements confirm that Nb and Mo exhibit the greatest extent of

microsegregation among solute species (i.e. discarding the concentrations of solvent species Fe and Ni). For both Nb and Mo, the segregation profile changes quite consistently and monotonically when the composition changes from 316L to IN718 — namely: a greater amount of IN718 means a greater initial concentration in Nb and Mo, which results in a greater extent of microsegregation during solidification. The plateau in Nb concentration and decrease in Mo concentration at the end of solidification ($f_s \geq 0.9$) is primarily linked to the predicted formation of C14 Laves, δ, and σ phases. Microsegregation of Nb and Mo is undoubtedly one of the key underlying mechanisms at play. However, as predicted segregation patterns do not exhibit any notable singularities around 20 wt.% IN718, we can conclude that it is only part of the explanation for the emergence of cracks.

In summary, our interpretation of the underlying mechanisms for cracking in 316L-IN718 underlines the key role of Nb and Mo segregation, which trigger the formation of C14 Laves phases in the 316L-rich of the gradient. The brittle C14 Laves phase forms as part of a low-melting temperature eutectic structure (Fig. 5.9), as suggested in [62]. The fact that C14 Laves are expected (from CalPhaD calculations) below and above the observed region for cracking ($\approx$ 10 to 25 wt.% IN718) shows that its mere formation is not a sufficient criterion to predict cracking. At low IN718 content, the content of C14 phases forming might not be sufficient to initiate cracking, which suggests a minimum threshold value for the occurrence of cracking. At higher IN718 content, C14 Laves is progressively replaced by δ phase, the presence of which does not correlate with the occurrence of cracks, absent in the IN718-rich half of the gradient.

In spite of minor discrepancy in terms of phase fractions (in particular σ) and exact temperature or composition ranges – expected when comparing equilibrium-based CalPhaD calculations with a nonequilibrium process such as DED – CalPhaD results are in reasonable agreement with experiments. Most importantly, they allow to rationalize and support the interpretations above.

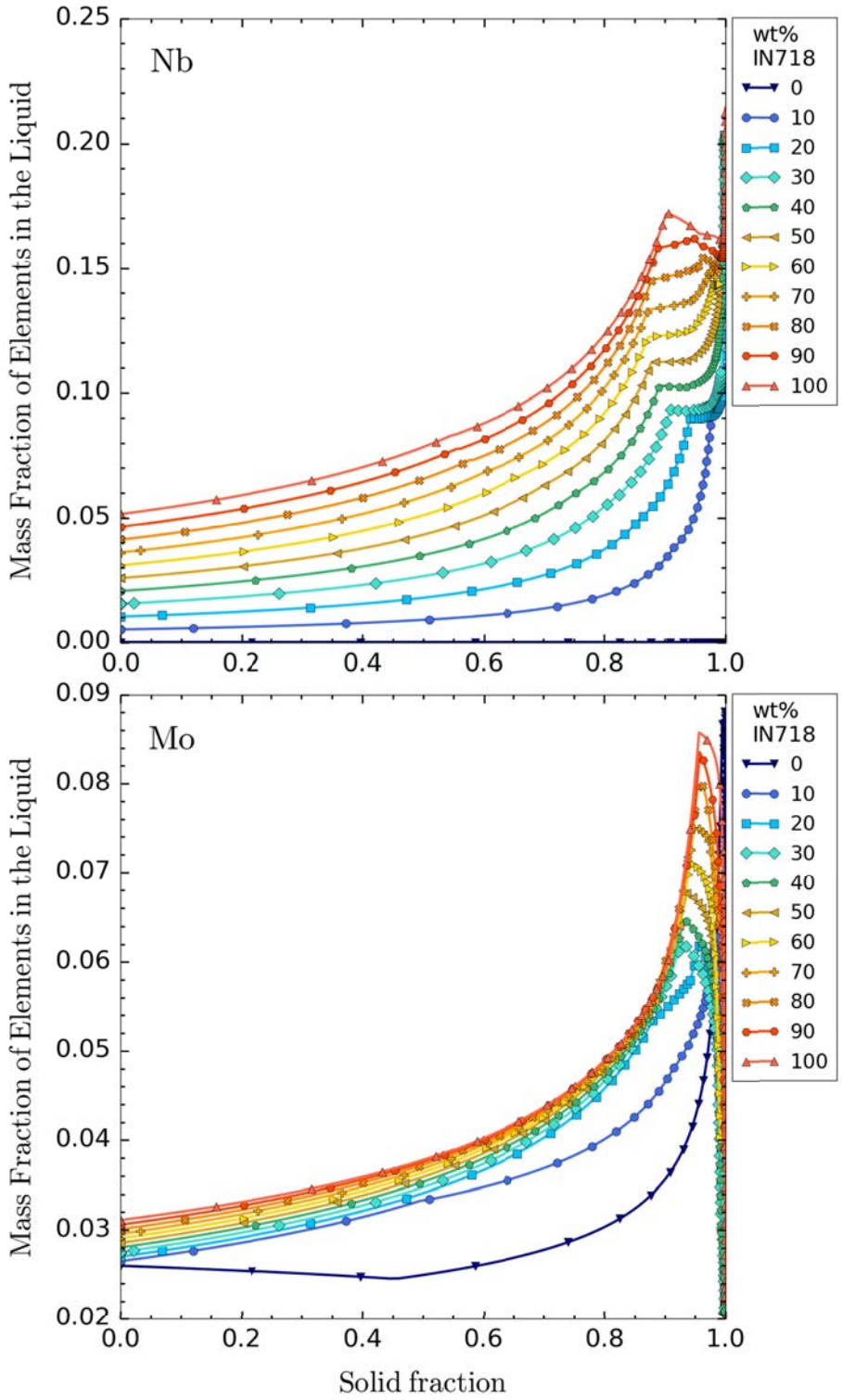

Figure 6.1: Comparative evolution of the mass fraction of Nb and Mo elements during a Gulliver-Scheil solidification path starting from different compositions along the 316L to IN718 gradient (line colors).

CHAPTER 7

CALPHAD STUDIES: ALLOY DESIGN & BEYOND

CalPhaD software, such as ThermoCalc, enable coupling calculations with programming languages like Python. Doing so allows high-throughput calculations, i.e. fast-paced multiple calculations sequentially or in parallel. This opens the possibility of exploring multiple composition ranges, boosting the capabilities of alloy design for a broad range of applications — with many examples throughout the literature [12, 42, 63, 68, 168, 170, 174, 187, 191, 192].

Along the course of my thesis, while focusing primarily on SS316L-IN718 graded alloys central to the MultiFAM project, I had the opportunity to contribute to several projects, providing supporting CalPhaD calculations in various applications. These spanned different technological targets related to metallurgy, like steel sintering (Section 7.1), Co-based superalloys (Section 7.2), high-entropy alloys (HEA) resistant to hydrogen embrittlement (Section 7.3), as well as a foray into the synthesis of nanowires (Section 7.4). Some of these works are already part of published papers (namely Sections 7.4 [65] and 7.2 [122]). For these, we only provide a brief description and refer to the published material for further details. Others studies (Sections 7.1 and 7.3) contributed to projects that are still active and not fully completed — expected to lead to further publicatiosn as co-author. Therefore, we describe their context in greater details, and focus more on the development of the methods and the intermediate results than the ultimate properties of the final selected alloys.

7.1. Master Alloys for Sintered Steels

One of the main studies on high-throughput simulations conducted in this thesis was an ongoing project called DAMAS — a collaborative project between IMDEA Materials, Universidad Carlos III de Madrid, and AMES, a leading companies in

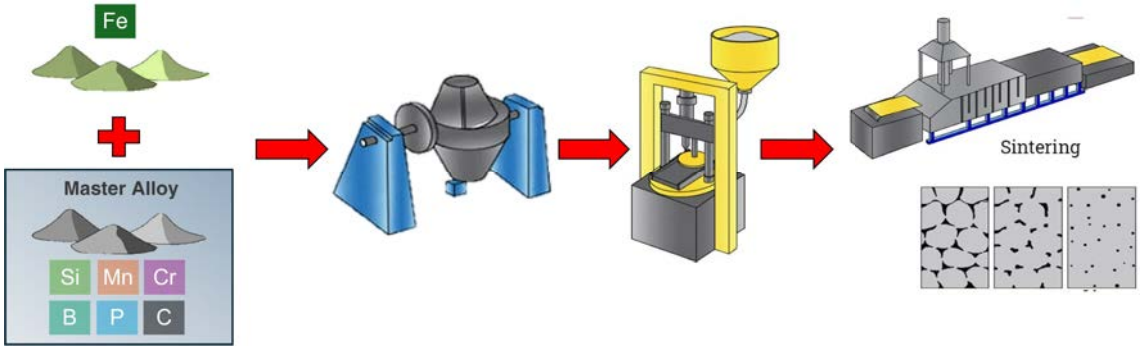

Figure 7.1: Workflow schematic of a sintered alloy manufactured using master alloy powders with Fe-based powders.

the sintering sector. The project aimed to search for new metal alloy compositions in powder form (master alloys), which, when incorporated with Fe powder, would lead to the alloying of different steels to be sintered (as seen in Fig. 7.1). The use of master alloys [28, 29, 30, 69, 121, 129, 194] has become an interesting alternative to pre-alloying mixtures from the beginning.

In this study, we want to decrease the number of alloying elements (while maintaining good properties and specific microstructures), prevent oxidation from specific elements like Si and Cr, and improve hardenability and mechanical properties with elements like Si and Mn. It has been observed in the past, when using these types of powders, that a small oxide layer appears at the sintering temperature T_{sint} (approximately at 1120°C), which can be minimized by having some liquid phase at this stage, enhancing diffusion. Therefore, one of the main boundary conditions to consider when looking for the best compositions was to decrease the liquidus temperature (T_l) and solidus temperature (T_s) to be as close as possible to T_{sint}.

For this study, we coupled ThermoCalc 2024 with Python scripting, using the TCFE9 database and applying a mapping across the composition ranges listed in Table 7.1. Several phases (*GRAPHITE, DIAMOND-FCC-A4, FE8SI2C, HCP-A3, SIC, CEMENTITE, M7C3, M5C2, M3C2, M23C6, GAS*) were rejected. The ranges and phases of interest were selected based on project consortium discussions, with an aim to asses the influence of the main alloying elements (Mn, Si & Cr) and the potential benefit of using some other minor alloying contributors (C, P & B).

All simulations detailed in Table 7.1 resulted in over 28 days of sequential calculations after several scans for a total of 245 446 possible alloy combinations — after some data cleaning for non-converged results. For each alloy combination, we obtained the value of T_l, T_s and monitored the volume fraction of phases at T_{sint}. With this data, we applied some filters to narrow down a more manageable dataset.

The first filter consisted of eliminating some unreliable data points as well as imposing that $T_l < 1100$°C and $T_s < 1000$°C to be closer to the initial T_{sint}. This substantially reduced the number of combinations by approximately a factor of 10,

Elements	Composition Range (wt.%)	Step (wt.%)	n° Steps
Fe	bal.	/	/
Mn	[25-40]	1.88	9
Si	[0, 5-15] + [Si & Cr = 0]	2	7
Cr	[0, 3-15] + [Si & Cr = 0]	1	14
C	[0-5]	1	6
P	[0-2]	0.29	7
B	[0-2]	0.29	7

Table 7.1: Information detailing the composition ranges, step size and number of steps calculated during the simulation campaign.

Filters	T_l Range (°C)	T_s Range (°C)	Vol% @ T_{sint}	n° Compositions
Raw	[875.5 - 2184.2]	[794.7 - 2126.8]	[0 - 100]	245.446
1^{st} Filter	[875.5 - 1100.1]	[795.3 - 999.9]	[100]	27.948
2^{nd} Filter	[1031.6 - 1078.4]	[902.9 - 971.7]	[100]	54
3^{rd} Filter	[1039.4 - 1078.4]	[906.4 - 971.7]	[100]	5

Table 7.2: Number of alloy combinations and parameter ranges after the different filtering steps.

as detailed in Table 7.2. One of the main challenges at this point was to find a compelling way to visualize and properly analyze all of the given combinations and tendencies between elements and how these affect the different parameters. For this reason, we explored different data layouts, like correlation matrices (Fig. 7.2) and interactive multidimensional plots (Fig. 7.3). Fig. 7.2 and any given correlation/anticorrelation matrix illustrates the influence of different parameters upon each other and allows to parametrize that relation with an index. In this case, it indicated which elements had a stronger influence in the variation of T_l and T_s. Here, C is the main contributor to increasing T_l and decreasing T_s, resulting in a bigger (T_l - T_s) freezing range, which is not ideal for any industrial application due to its links to potential defects. Cr and Si also have a remarkable influence, increasing T_l and T_s while decreasing the available liquid fraction at T_{sint}. Mn and P do also have a certain influence in decreasing T_s. To further complement these tendencies with qualitative data, we can plot multidimensional plots (Fig. 7.3), where a given parameter (like T_l) can be compared as a function of up to 4 elements (e.g. adding a slider and a color bar). In this case, we included some of the more relevant elements described before (C, Si, Cr, Mn), confirming these tendencies by obtaining actual T_l values.

Based on these observations and adding certain industrial constraints (e.g. linked accessible furnace temperatures and related production costs), we applied a more severe filter by fixing some of the elements (Mn(wt.%) = 25, Si(wt.%) = 5, Cr(wt.%)

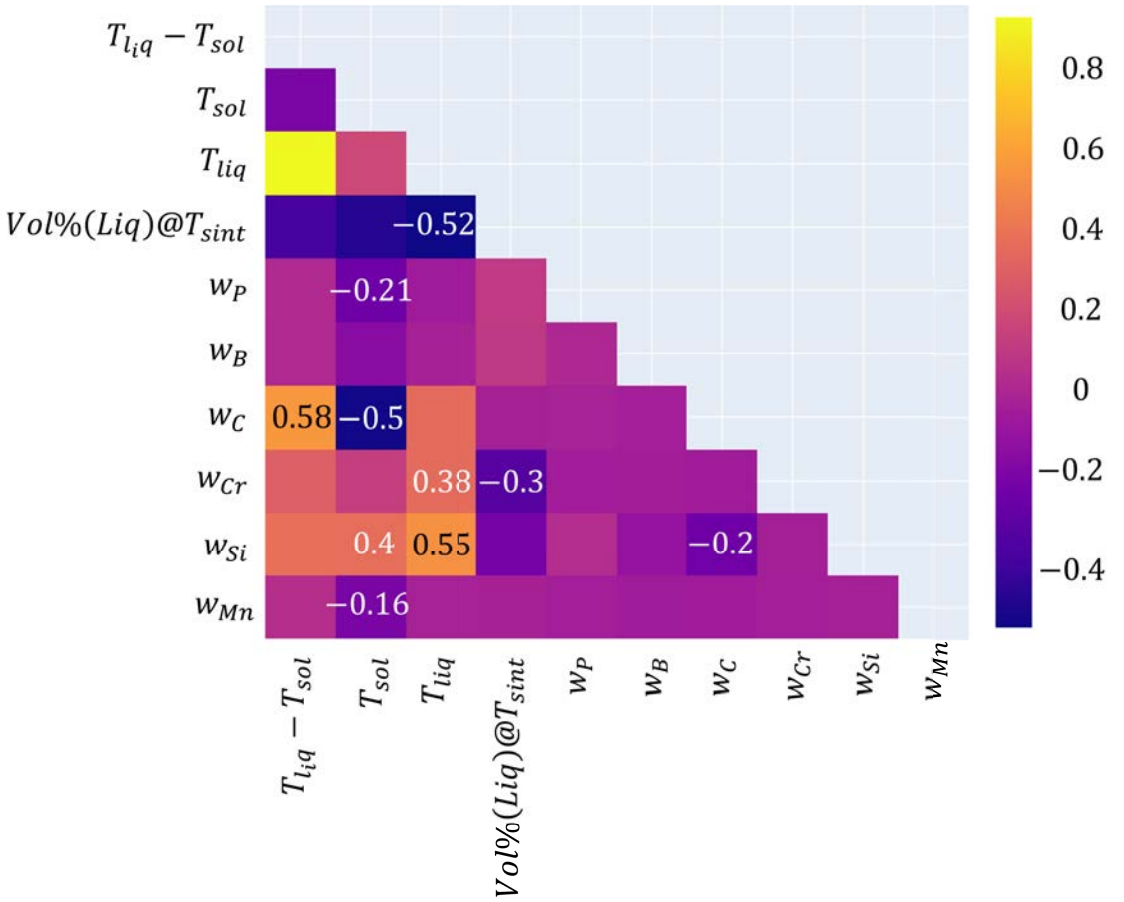

Figure 7.2: Correlation matrix, relating the main indicators with the composition of all alloying elements. The highest and lowest correlation/anticorrelation points are also detailed.

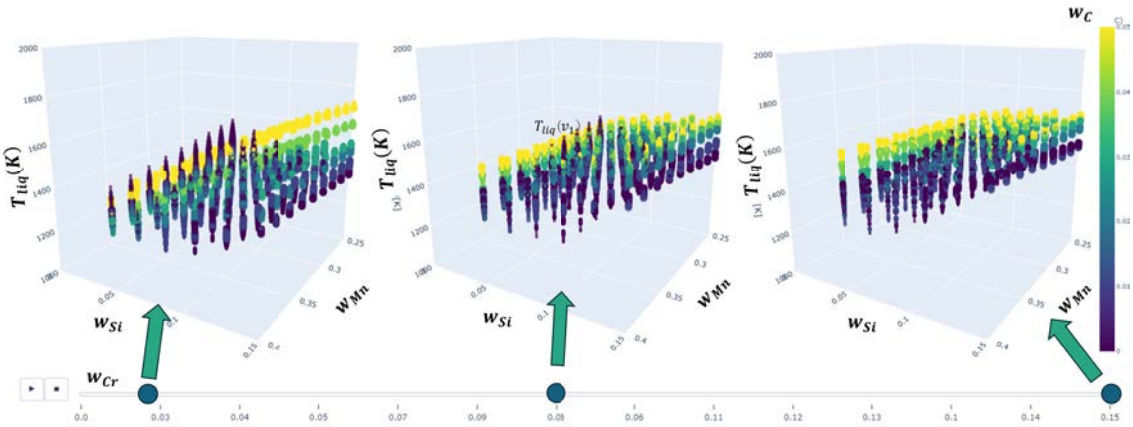

Figure 7.3: Multidimensional plots detailing the evolution in T_l of the datapoints when adding more Cr (slidebar) as a function of Si, Mn, and C (color bar).

= 3, C(wt.%) = 4) and focusing on the influence of some of the remaining alloys, reducing the number of combinations to 54. Alloys in this small group fulfilled some of the requirements of the given application. Still, to select a manageable number

Alloy	Composition (wt.%)							T_l(°C)	T_s(°C)
	Fe	Mn	Si	Cr	C	B	P		
FeMnSiCrC	bal.	25	5	3	4	0	0	1078.4	971.7
FeMnSiCrC + B	bal.	25	5	3	4	0.58	0	1039.4	941.4
FeMnSiCrC + P	bal.	25	5	3	4	0	1.16	1040.9	925.1
FeMnSiCrC + B + P	bal.	25	5	3	4	0.58	0.29	1040.2	906.4
FeMnSiCrC + B + P	bal.	25	5	3	4	0.58	0.58	1040.9	908.3

Table 7.3: Selected compositions by the end of applying all the described filtering.

of combinations to be manufactured, we selected one alloy with B, one with P, two with both, and one without both, as detailed in Table 7.3. These alloys were selected because of their values of T_l and T_s, which are close to previous successful studies from AMES (T_l= 1040°C; T_s= 908°C), and as an interesting approach to experimentally analyze the influence of these elements. At the time of writing, the fabrication and experimental validation of the selected alloys based on this CalPhaD analysis is still in progress.

7.2. Design of High Entropy CoNi-superalloys

Another study in collaboration with the *Sustainable Powder Technologies* group at IMDEA was published in [122]. Here, we supported the design of CoNi-superalloys for high-temperature applications. Based on an extensive literature review, a relationship was identified between the entropy of mixing, the number of elements, and the γ' solvus temperature (T_γ') in Co or CoNi-based superalloys, enabling a better performance at high temperatures. Three alloys (CNS1, CNS2 & CNS3 — see details in [122]) were designed, considering alloying elements with high-temperature capabilities and low density while targeting specific values of entropy of mixing. An idea was to optimize the composition to obtain an alloy with an appropriate and adaptable processing window (thanks to the fine-tuning of the γ' (solvus temperature)) and freezing range. To help support the alloy design, we performed different simulations, showing the evolution of expected phases along the temperature (Fig. 7.4(d-f)), highlighting T_l, T_s, and T_γ'. In addition, we constructed different isopleth diagrams (Fig. 7.4(a-c)) that allowed us to assess the influence of certain elements like Ni in the phase equilibrium and temperature ranges. Comparing with experimental data provided by EBSD and EDS analysis (Fig. 7.4(g-j)) and for this specific case study, CalPhaD was able to successfully predict the microstructure despite not having perfectly aligned (quantitative) results for T_l, T_s, and T_γ'.

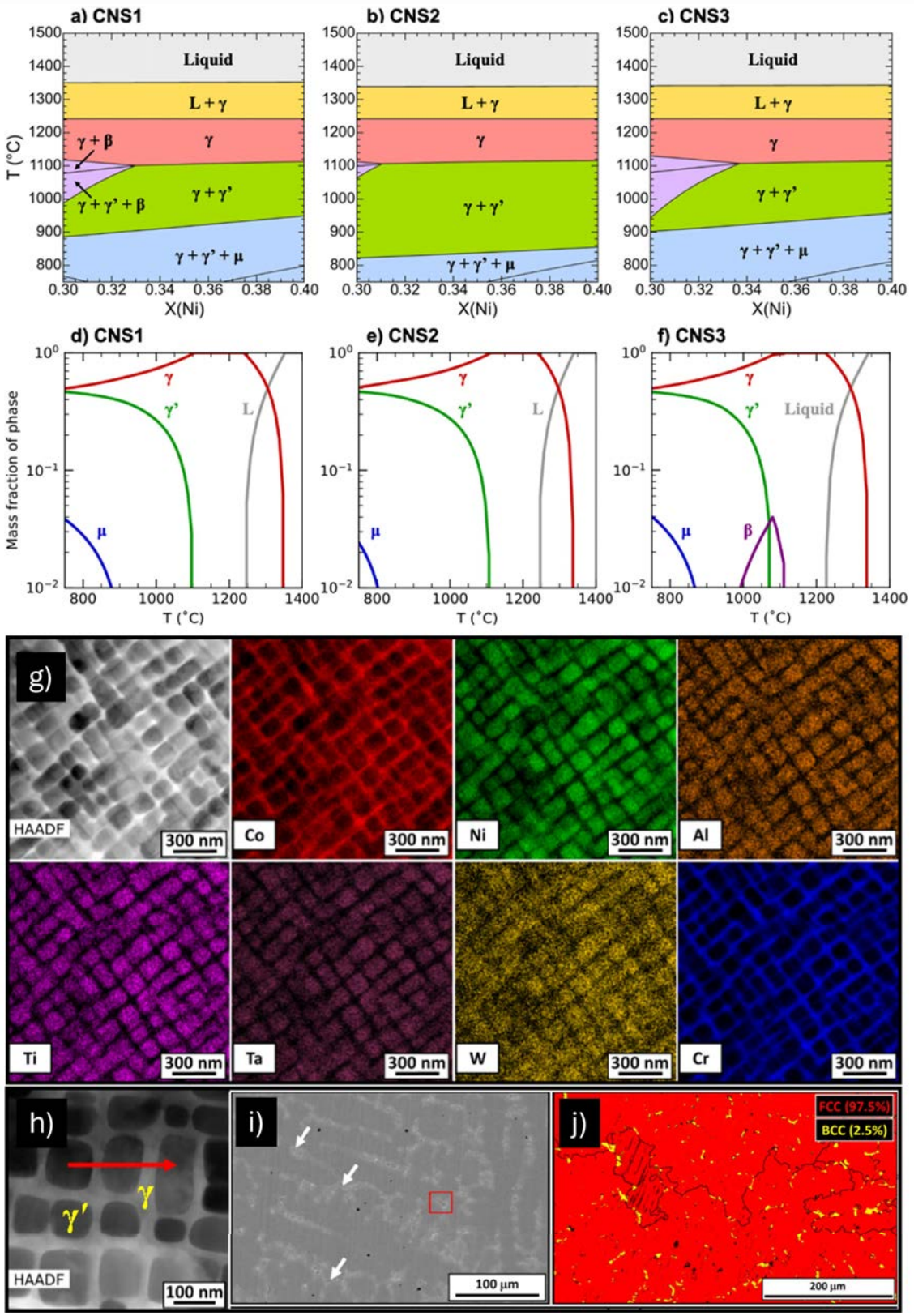

Figure 7.4: (a-c) Phase diagram isopleth sections showing the effect of Ni alloy content at the expense of Co. (d-f) Phase equilibrium evolution along the temperature of the three different alloy configurations. (g) SEM image and corresponding EDS maps of different elements and EBSD phase maps (i-j)[122].

7.3. High Entropy Alloy (HEA) design for better hydrogen behavior

Another application of CalPhaD for alloy design is an ongoing project named EARTH, coordinated by the Universidad Carlos III de Madrid, in collaboration with IMDEA Materials and the Universidad Politécnica de Madrid. The aim of this project is to design new alloys for hydrogen storage to promote the green transition. Stainless steels (especially austenitic) have been used for this purpose for some time [15, 83, 154, 175, 196], having mixed results due to hydrogen-induced embrittlement. For that reason and with the emergence of High Entropy Alloys (HEAs) and advanced computational tools that allow high-throughput calculations for alloy design [63, 168], it has become more popular to seek solutions using this family of materials [109, 155, 185]. HEAs are a family of alloys designed with no base element and small quantities of alloying elements (as in traditional metallurgy) but rather combine multiple alloying elements in high concentrations, (close to) equiatomic in some cases [35, 60]. This has contributed to obtaining alloys with new and improved characteristics for several applications [101, 102], resulting in a rising interest [120, 167, 193]. The use of both high-throughput and HEAs has started to gain some traction [42, 68, 187] despite the remaining need to develop robust methodologies, as well as using different simulation methods such as DFT (Density Functional Theory).

For this project, the idea is to manufacture new HEAs using different manufacturing techniques and test them under hydrogen environment to obtain the best possible candidate. Our specific role in this endeavor is to screen and select the most promising compositions. To do so, we took inspiration into recent studies relating stacking fault energy and hydrogen embrittlement [55, 64], however more related to austenitic stainless steels. These studies suggest that the stacking fault energy (SFE) is a good indicator to register the tendency for the austenite phase to undergo either a direct transformation to α'-martensite (when SFE $\leq$ 20 mJ/m^2) or an indirect martensitic transformation involving the intermediate phase of ε-martensite. This ε-martensite phase seems to have a negligible influence on hydrogen embrittlement since HCP phases do not seem to show hydrogen-induced embrittlement at room temperature [151]. On top of that, this can come as a result of the ε-martensite phase retarding the localization of plastic deformation mechanisms in austenitic steels [163]. Alloys with an increasing propensity for planar slip tend to have higher values of SFE ($= 20 - 40$ mJ/m^2) and higher susceptibility to degradation when doing mechanical testing under hydrogen conditions. Studying this phenomenon and being able to calculate this SFE offers a potential pathway to discover alloys with good resistance to hydrogen embrittlement [64].

To approximate the SFE value, there is a theoretical thermodynamic model [16, 52, 74, 119], which exhibits slight variations and interpretations across publication and has been used recently [16, 44, 59, 96, 142] for this purpose. This model, first presented in [127], is depicted in Eq. (7.1), where ρ is the molar surface density along

the atomic planes, obtained with Eq. (7.2), depending on the lattice parameter (a) of each cubic structure; $\sigma^{\gamma/\varepsilon}$ is the interfacial energy per unit area of the γ/ε phases boundaries and $\Delta G^{\gamma\to\varepsilon}$ is the molar Gibbs free energy for the γ (FCC) $\to \varepsilon$ (HCP) transformation. This Gibbs free energy difference is a sum of different energetic contributions (chemical = $\Delta G^{\gamma\to\varepsilon}_{\text{che}}$, grain size driving force = ΔG_{GS} and magnetic = $\Delta G^{\gamma\to\varepsilon}_{\text{mg}}$) as shown in Eq. (7.3).

$$\gamma_{\text{SFE}} = 2\rho\Delta G^{\gamma\to\varepsilon} + 2\sigma^{\gamma/\varepsilon} \tag{7.1}$$

$$\rho = \frac{4}{\sqrt{3}} \cdot \frac{1}{a^2 \cdot N_A} \tag{7.2}$$

$$\Delta G^{\gamma\to\varepsilon} = \Delta G^{\gamma\to\varepsilon}_{\text{che}} + \Delta G_{\text{GS}} + \Delta G^{\gamma\to\varepsilon}_{\text{mg}} \tag{7.3}$$

Unfortunately and referring to the literature [64], it is challenging to obtain empiric or theoretical values of some of these contributions — often using orders of magnitudes for some of these values or presenting big simplifications of the model [128]. In particular, $\sigma^{\gamma/\varepsilon}$ has been widely used as an empirical value to round the final values of the equation [128], while finding reliable values of $\Delta G^{\gamma\to\varepsilon}_{\text{mg}}$ is also challenging.

Here, we decided to apply a qualitative approach, focusing on the terms that we can explicitly calculate, and assuming that other terms have a relatively minor effect. Hence, $\sigma^{\gamma/\varepsilon}$ was neglected due to insufficient information in the literature, as this is most often just a constant (ranging between $8 - 27$ mJ/m^2) thus not affecting the qualitative comparison between alloys. The same happens with ΔG_{GS} that relates to the grain size, which strongly depends on processing conditions, and here considered constant for the batch calculations. $\Delta G^{\gamma\to\varepsilon}_{\text{mg}}$ was also neglected despite having a remarkable influence on the SFE factor since most of the parameters could not be obtained for all element and phase combinations. Under these considerations, the final estimation revolved around calculating $\Delta G^{\gamma\to\varepsilon}_{\text{che}}$ and ρ across a specific composition range. All calculations were conducted using ThermoCalc coupled with the TC-Python module and the TCHEA6 (High Entropy Alloy) database.

After finding a suitable temperature where we can ensure that both HCP and FCC phases coexist, we generated a batch of simulations for the FeCoCrNiMo system, rejecting all phases but LIQUID, FCC-L12, and HCP-A3. The goal was to obtain the value of $\Delta G^{\gamma\to\varepsilon}_{\text{che}}$ (calculating both $\Delta G^{\gamma}_{\text{che}}$ and $\Delta G^{\varepsilon}_{\text{che}}$) and the volume of the system (to obtain the lattice parameter and consequently, the value of ρ). For this first screening, the composition ranged from 0-100 wt.% for each element in steps of 10 wt.%. In addition to other filtering criteria, we also applied the HEAPS (High-Entropy Alloys Predicting Software) methodology to predict possible TCP (σ, Laves phase,...) formation [115]. This HEA-oriented tool integrates several physical and semi-empirical parameters and applies them to different criteria addressing the prediction of their phase formation and mechanical properties, allowing quick batch calculations that complement the CalPhaD data.

Filters	γ_{SFE} (mJ/m^2)	Compositions
Raw	[-5496.3 – 6603.8]	975
1^{st} Filter (wt.% $\neq 0$)	[105.5 – 5386.4]	126
2^{nd} Filter ($\gamma^N_{\mathrm{SFE}} \leq 20 mJ/m^2$ + HEAPS)	[105.5 – 162.6]	46
3^{rd} Filter ($T_l \leq 1600$°C)	[126.7]	1

Table 7.4: Alloy combinations and parameter ranges after the different batch screenings.

Alloy	Composition (wt.%)					T_l(°C)	γ_{SFE} (γ^N_{SFE}) (mJ/m^2)
	Fe	Co	Cr	Ni	Mo		
FeCoCrNiMo	10	50	10	20	10	1513	126.7 (16.7)

Table 7.5: Final composition after every filtering step.

This first screening resulted in up to 975 alloy combinations, with a wide range of γ_{SFE} values (Table 7.4), most of them in an order of magnitude higher than the literature. This also includes some negative values, commonly not regarded in experimental measurements, but recent studies validate their existence in some cubic-centered alloys [177]. After rejecting any null compositions, focusing closer to more equiatomic configurations, the final dataset included 126 alloy combinations. To support the validity of this qualitative estimation and to be able to calibrate it to our needs, we also included and applied this model to other alloys with well-documented experimental γ_{SFE} values, like the Cantor alloy [35]. By doing so, we could normalize the datasets' values to determine whether γ_{SFE} is higher or lower than 20 mJ/m^2. When applying this, as well as checking for any TCP phases using the HEAPS methodology, we reduced the number of possible candidates to 46. Complimentary and to ensure that the qualitative comparison was reliable, we calculated γ_{SFE} for a specific alloy tested by one of the project collaborators in hydrogen-induced conditions. This alloy presented outstanding mechanical performance and ranked as one of the top-5 lowest in γ_{SFE} compared with the alloy dataset from the calculations.

A final design constraint had to be implemented that helped select one alloy out of the final cluster. In order to facilitate processing by atomization of the final candidate in the facilities available to the project, we restricted $T_l \leq 1600$°C. When calculating T_l for these 46 alloys, one appeared as the ideal candidate (Table 7.5).

It is worth noting that the final selected alloy is relatively far from an equiatomic composition. After doing a finer step scans for the lowest γ_{SFE} close to equiatomic, none of them had low enough T_l. When analyzing these data (Fig. 7.5), γ_{SFE} showed some positive correlation with Ni and some slight anticorrelation with Fe and Co. Surprisingly, Mo showed barely any effect. Some of the alloy candidates with lower γ_{SFE} did show high content in Mo (and consequently, depletion of Ni), but also high

T_l, as displayed in Fig. 7.5. For that reason, we had to move towards less equiatomic configurations. The final alloy selection has a combination of high content of Co (slight anticorrelation with γ_{SFE} and almost no influence on T_l), with low content of Mo to lower T_l and slightly higher values of Ni to obtain an even lower T_l, which resulted in a more restrictive condition than any other. Only two alloy combinations (as well as the previously mentioned alloy with outstanding behavior in hydrogen-induced conditions) fulfilled all conditions, one being the final one, which presented lower γ_{SFE}.

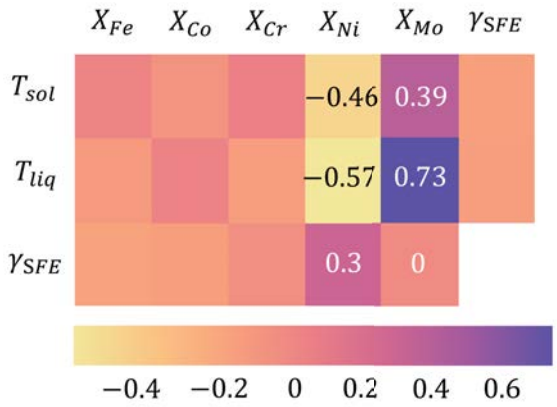

Figure 7.5: Correlation matrix, relating γ_{SFE}, T_l, and T_s with the composition of all alloying elements. The highest and lowest correlation/anticorrelation points are also detailed.

7.4. Reaction path during nanowire growth

The final example of use of CalPhaD is the furthest from classical metallurgy, and illustrates well the range of application fo the method. In close collaboration with the *Multifunctional Nanocomposites* group at IMDEA, we studied the synthesis of SiC nanowires (NWs) using a novel floating catalyst chemical vapor deposition (FC-CVD) method. This novel method, which results in NW growth rates over 3 orders of magnitude faster than classical substrate-based CVD, thus enables the assembly of NWs into macroscopic yarns or fabrics [65]. FCCVD utilizes a floating Fe aerosol with catalytic nanoparticles and hexamethyldisilane (HMDS, $Si_2C_6H_{18}$) as SiC precursor. The role of CalPhaD calculations here was to rationalize the reaction path going from the Fe catalyst to the final SiC NW as HMDS is introduced in the system. The results for this specific case is depicted in Fig. 7.6. We first calculated a ternary phase diagram (Fig. 7.6a) for the Fe-Si-C system close to the reaction temperature ($T \approx 1200$°C) to assess phase equilibria along the change in composition. Fig. 7.6d shows an isopleth diagram to better analyze the straight Fe to SiC path. Fig. 7.6b-c describe the compositional path from the Fe particles to SiC. The dashed line in Fig. 7.6b illustrates the compositional path starting from a Fe-rich

particle (labeled a) exposed to an influx of Si and C, assuming a C:Si influx ratio of 1:3 from HMDS. Our interpretation of the reaction path is the following. From (a) to (b), the Fe phase incorporates Si and C into the FCC Fe phase; from (b) to (c), a liquid phase forms jointly with the FCC solid, and the fraction of liquid increases as the systems gets richer in Si and C species; from (c) to (d), the sole liquid phase is enriched in Si and C; from (d) to (e), the addition of Si and C leads to the liquid exceeding its maximum solubility in C (but not in Si), leading the the segregation of pure C (graphite) and enriching the liquid in Si, until it reaches (e) and starts forming a SiC phase. While this analysis provides valuable insight into the reaction path during the synthesis of SiC NWs from Fe precursors, these calculations show the equilibrium phases for a bulk system at perfect thermodynamic equilibrium, neglecting interfacial energy contributions that are not usually negligible in nano-sized systems. These contributions tend to shift the phase diagram toward lower temperatures when accounted for.

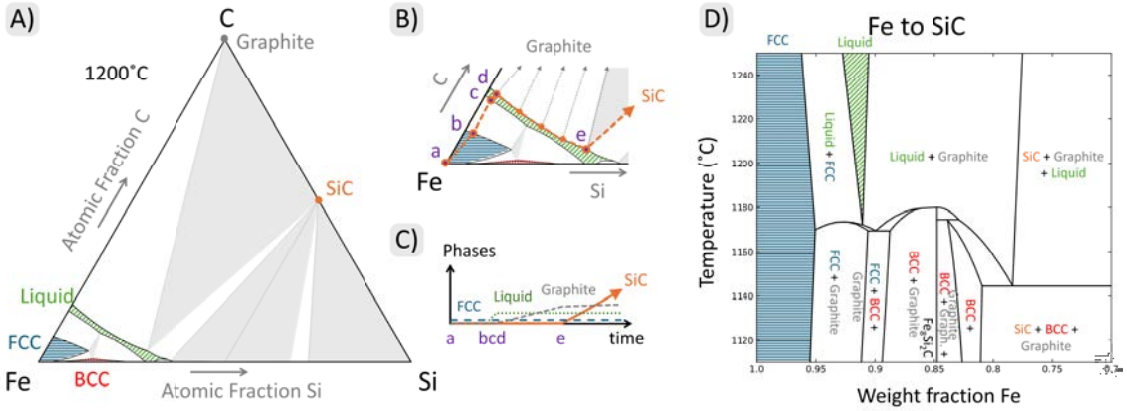

Figure 7.6: Calculated ternary Fe-Si-C phase diagram and compositional path from Fe catalyst to SiC. (a) Ternary isothermal phase diagram at 1200°C. Gray triangles show three-phase invariant equilibria; hatched regions show single-phase regions; for clarity, tie-lines are not shown (hence two-phase regions appear white). (b) The compositional path from pure Fe to SiC formation following continuous addition of Si and C. (c) Qualitative formation of phases along the proposed compositional path. (d) Isopleth section of the phase diagram through pure Fe and SiC [65].

CHAPTER 8

SUMMARY & PERSPECTIVES

8.1. Summary

This thesis encompasses four years of research dedicated to studying functionally graded structures by leveraging thermodynamic principles and advanced characterization techniques. The following conclusions summarize our key findings:

- Our results show that DED can be used to manufacture functionally graded materials for different printing and grading parameters. However, grading strategies explored here resulted in intergranular cracking at a specific composition ranges within the gradient (namely 10-25 wt.% IN718), parallel to the build direction and in increasingly larger amounts when decreasing the grading step value (defects FGM05 > FGM10 > FGM20). These cracks, more prevalent in longer graded transitions, correlate with Nb and Mo segregation patterns and areas of increased hardness.

- Overall, macroscopic properties, such as hardness and thermal expansion coefficients, exhibit a close to linear variation, with no significant steep gradient in the region of high defect density. Compression tests on samples extracted from the graded region revealed that more progressive gradients exhibited stress-strain curves similar to the weaker alloy (316L), while steeper gradients appear to yield a more progressive transition with intermediate behavior within the gradient. These results suggest discarding a mismatch in macroscopic thermomechanical properties as the origin of the cracks.

- At the microscopic scale, cracks were observed to follow segregation patterns in regions of high Nb and Mo content, and resulting micromechanical heterogeneous properties. Moreover, eutectic-like structures rich in C14 Laves phase were identified in the cracked regions, as well as δ phase. Thermodynamic

calculations indicate that the first secondary phase to appear is C14 Laves on the 316L-rich side of the composition range, while it is δ on the IN718-rich side. These observations, combined with a high crack susceptibility index in the 316L-rich side, indicate that microsegregation and the formation of C14 Laves phase in the late stages of solidification are the likely causes of the interdendritic cracking in the 10-25 wt.% IN718 region of the composition gradient.

- The a-priori counterintuitive observation that a more progressive grading leads to larger and denser cracks than a sharper transition actually makes sense when considering that the underlying mechanism for cracking is not the mismatch in thermo-mechanical properties — as observed in sharp-transition multi-material printing [40, 117, 178, 182] — but rather the formation of intermetallics and low-melting eutectics in a given compositional range within the alloy gradient. Indeed, in this context, a more progressive gradient results in more layers within the compositional range leading to cracks, explaining the most prominent cracks observed in FGM05 compared to other samples.

Other thermodynamic calculations for a broad range of applications led to the following conclusions:

- CalPhaD-based simulations are advantageous as an initial step in materials design, aiding in the understanding of how various alloying elements impact targeted microstructures/properties.
- For master alloy design, multiple batch calculations were conducted, enabling the selection of a subset of candidate alloys with the assistance of data analysis tools such as correlation matrices. This approach helped identify key relationships between elements and critical properties, such as liquidus (T_l) and solidus (T_s) temperatures.
- In designing hydrogen-resistant alloys, a simplified model was used to estimate qualitatively the variation of γ_{SFE} (stacking fault energy) as a design metric for assessing susceptibility to hydrogen embrittlement. This model was subsequently adapted and normalized, aligning with trends observed in related experiments and literature. The γ_{SFE} parameter was calculated for a broad compositional range within a five-element system, with filters applied to identify potential hydrogen-resistant alloys that meet project specifications.

8.2. Perspectives

Building upon these findings, several avenues for future research can further advance the understanding of these applications. The following proposed directions address

key challenges identified in this study and suggest ways to enhance design flexibility and predictive accuracy:

- **Expand the Design of Complex Graded Structures:** Increasing the number of DED powder tanks to more than two could unlock broader compositional pathways, allowing for more nuanced gradients and reducing the likelihood of forming undesired phases, uneven solidification ranges, and incompatible solubility gaps. With this approach, one might conceive strategies based on path planning within the compositional space [26, 50, 85, 86] in order to specifically avoid the formation of detrimental phases (here, C14 Laves). Other options include the introduction of intermediate layers of different alloys [22, 24] in order to specifically avoid the formation of detrimental phases or to specifically optimize printability metrics, e.g. minimizing crack susceptibility. In addition, data-centric tools, including machine learning and digital twins, have already made some significant strides in advancing the efficiency, accuracy, and sustainability of AM processes [78] and could certainly play a key role in accelerating the design of defect-free FGMs.

- **Develop CalPhaD-Based Heat Treatments for Graded Joints:** The application of CalPhaD-designed heat treatments could offer greater flexibility in managing graded joint properties, especially in cases where the initial microstructural and property mismatches are significant. Tailoring post-processing steps in this way may reduce stress concentrations, mitigate phase imbalances, and enhance the structural integrity of the joints.

- **Explore Advanced Characterization Techniques:** Incorporate high-resolution methods, such as synchrotron X-ray computed tomography and neutron diffraction, to gain deeper insights into the microstructure, texture, and phase evolution within localized regions of the graded samples. These techniques could offer a more precise depiction of the compositional characteristics across gradients, enhancing the understanding of microstructural variations. This represents a promising path for future work, with ongoing efforts already underway.

- **Utilize Advanced Statistical Tools for Batch CalPhaD Data Analysis:** Incorporating more statistically robust tools for batch CalPhaD calculations would enhance the ability to analyze and visualize complex datasets, revealing correlations across properties, compositions, and elemental interactions. Unlike correlation matrices, these tools could capture the simultaneous effects of multiple elements, providing deeper insights into compositional influences on key properties and helping to identify optimal alloy compositions with increased precision.

BIBLIOGRAPHY

[1] TE Abioye, J Folkes, and Adam T Clare. "A parametric study of Inconel 625 wire laser deposition". In: *Journal of Materials Processing Technology* 213.12 (2013), pp. 2145–2151.

[2] *Additive manufacturing*. https://www.manufacturingguide.com/en/additiv-tillverkning. Accessed: 2024-03-06.

[3] Dong-Gyu Ahn. "Directed energy deposition (DED) process: State of the art". In: *International Journal of Precision Engineering and Manufacturing-Green Technology* 8 (2021), pp. 703–742.

[4] Enes Akca and Ali Gürsel. "A review on superalloys and IN718 nickel-based INCONEL superalloy". In: *Periodicals of engineering and natural sciences* 3.1 (2015).

[5] Suhas Alkunte et al. "Advancements and Challenges in Additively Manufactured Functionally Graded Materials: A Comprehensive Review". In: *Journal of Manufacturing and Materials Processing* 8.1 (2024), p. 23.

[6] Tarak Amine, Joseph W Newkirk, and Frank Liou. "An investigation of the effect of direct metal deposition parameters on the characteristics of the deposited layers". In: *Case Studies in Thermal Engineering* 3 (2014), pp. 21–34.

[7] Tarak Amine, Joseph W Newkirk, and Frank Liou. "Methodology for studying effect of cooling rate during laser deposition on microstructure". In: *Journal of Materials Engineering and Performance* 24.8 (2015), pp. 3129–3136.

[8] K Antony and N Arivazhagan. "Studies on energy penetration and Marangoni effect during laser melting process". In: *J. Eng. Sci. Technol* 10.4 (2015), pp. 509–525.

[9] All rights reserved to ArcelorMittal Innovacion Investigacion e Inversion S.L. *Memoria de retos de Colaboracion 2019 Multi-FAM*.

[10] Marcel Bachmann, Vjaceslav Avilov, Andrey Gumenyuk, and Michael Rethmeier. “Numerical simulation of full-penetration laser beam welding of thick aluminium plates with inductive support”. In: *Journal of Physics D: Applied Physics* 45.3 (2011), p. 035201.

[11] Amit Bandyopadhyay and Bryan Heer. “Additive manufacturing of multi-material structures”. In: *Materials Science and Engineering: R: Reports* 129 (2018), pp. 1–16.

[12] Adarsh Bansal, Pankaj Kumar, Shubham Yadav, VS Hariharan, MR Rahul, and Gandham Phanikumar. “Accelerated design of high entropy alloys by integrating high throughput calculation and machine learning”. In: *Journal of Alloys and Compounds* 960 (2023), p. 170543.

[13] Han-Sheng Bao, Zhi-Hua Gong, Zheng-Zong Chen, and Gang Yang. “Evolution of precipitates in Ni–Co–Cr–W–Mo superalloys with different tungsten contents”. In: *Rare Metals* 39 (2020), pp. 716–724.

[14] J Barcik. “Mechanism of σ-phase precipitation in Cr–Ni austenitic steels”. In: *Materials Science and Technology* 4.1 (1988), pp. 5–15.

[15] Hervé Barthélémy, Mathilde Weber, and Françoise Barbier. “Hydrogen storage: Recent improvements and industrial perspectives”. In: *International Journal of Hydrogen Energy* 42.11 (2017), pp. 7254–7262.

[16] P Behjati and A Najafizadeh. “Role of chemical driving force in martensitic transformations of high-purity Fe-Cr-Ni alloys”. In: *Metallurgical and Materials Transactions A* 42.12 (2011), pp. 3752–3760.

[17] Juraj Belan. “GCP and TCP phases presented in nickel-base superalloys”. In: *Materials Today: Proceedings* 3.4 (2016), pp. 936–941.

[18] A Ben-Artzy et al. “Compositionally graded SS316 to C300 Maraging steel using additive manufacturing”. In: *Materials & Design* 201 (2021), p. 109500.

[19] Jeffrey Malcolm Benson and Ettienne Snyders. “The need for powder characterisation in the additive manufacturing industry and the establishment of a national facility”. In: *South African Journal of Industrial Engineering* 26.2 (2015), pp. 104–114.

[20] Lourdes D Bobbio, Brandon Bocklund, Zi-Kui Liu, and Allison M Beese. “Tensile behavior of stainless steel 304L to Ni-20Cr functionally graded material: experimental characterization and computational simulations”. In: *Materialia* 18 (2021), p. 101151.

[21] Lourdes D Bobbio et al. “Additive manufacturing of a functionally graded material from Ti-6Al-4V to Invar: Experimental characterization and thermodynamic calculations”. In: *Acta Materialia* 127 (2017), pp. 133–142.

[22] Lourdes D Bobbio et al. “Analysis of formation and growth of the σ phase in additively manufactured functionally graded materials”. In: *Journal of Alloys and Compounds* 814 (2020), p. 151729.

[23] Lourdes D Bobbio et al. “Characterization of a functionally graded material of Ti-6Al-4V to 304L stainless steel with an intermediate V section”. In: *Journal of Alloys and Compounds* 742 (2018), pp. 1031–1036.

[24] Lourdes D Bobbio et al. “Design of an additively manufactured functionally graded material of 316 stainless steel and Ti-6Al-4V with Ni-20Cr, Cr, and V intermediate compositions”. In: *Additive Manufacturing* 51 (2022), p. 102649.

[25] Lourdes D Bobbio et al. “Experimental analysis and thermodynamic calculations of an additively manufactured functionally graded material of V to Invar 36”. In: *Journal of Materials Research* 33.11 (2018), pp. 1642–1649.

[26] Brandon Bocklund, Lourdes D Bobbio, Richard A Otis, Allison M Beese, and Zi-Kui Liu. “Experimental validation of Scheil–Gulliver simulations for gradient path planning in additively manufactured functionally graded materials”. In: *Materialia* 11 (2020), p. 100689.

[27] Brandon Bocklund, Lourdes D Bobbio, Richard A Otis, Allison M Beese, and Zi-Kui Liu. “Scheil-Gulliver simulations for the design of functionally graded alloys by additive manufacturing using pycalphad”. In: *arXiv preprint arXiv:2001.11611* (2020).

[28] Leandro Bolzoni, PG Esteban, Elisa María Ruiz-Navas, and E Gordo. “Influence of powder characteristics on sintering behaviour and properties of PM Ti alloys produced from prealloyed powder and master alloy”. In: *Powder Metallurgy* 54.4 (2011), pp. 543–550.

[29] Leandro Bolzoni, PG Esteban, Elisa María Ruiz-Navas, and E Gordo. “Mechanical behaviour of pressed and sintered titanium alloys obtained from master alloy addition powders”. In: *Journal of the mechanical behavior of biomedical materials* 15 (2012), pp. 33–45.

[30] Leandro Bolzoni, T Weissgaerber, B Kieback, Elisa María Ruiz-Navas, and E Gordo. “Mechanical behaviour of pressed and sintered CP Ti and Ti–6Al–7Nb alloy obtained from master alloy addition powder”. In: *Journal of the Mechanical Behavior of Biomedical Materials* 20 (2013), pp. 149–161.

[31] David Bourell et al. “Materials for additive manufacturing”. In: *CIRP Annals* 66.2 (2017), pp. 659–681.

[32] MC Brennan, JS Keist, and TA Palmer. *Defects in metal additive manufacturing processes*. 2021.

[33] GJ Brentrup, BS Snowden, JN DuPont, and JL Grenestedt. “Design considerations of graded transition joints for welding dissimilar alloys”. In: *Welding journal* 91 (2012), pp. 252–59.

[34] Felipe Rocha Caliari, Nara Miranda Guimarães, Danieli Aparecida Pereira Reis, Antonio Augusto Couto, Carlos de Moura Neto, and Katia Cristiane Gandolpho Candioto. "Study of the secondary phases in inconel 718 aged superalloy using thermodynamics modeling". In: *Key Engineering Materials*. Vol. 553. Trans Tech Publ. 2013, pp. 23–28.

[35] Brian Cantor. "Multicomponent high-entropy Cantor alloys". In: *Progress in Materials Science* 120 (2021), p. 100754.

[36] GH Cao et al. "Investigations of γ', γ" and δ precipitates in heat-treated Inconel 718 alloy fabricated by selective laser melting". In: *Materials Characterization* 136 (2018), pp. 398–406.

[37] Beth E Carroll et al. "Functionally graded material of 304L stainless steel and inconel 625 fabricated by directed energy deposition: Characterization and thermodynamic modeling". In: *Acta Materialia* 108 (2016), pp. 46–54.

[38] Pankaj Kumar Chauhan and Sabah Khan. "Microstructural examination of aluminium-copper functionally graded material developed by powder metallurgy route". In: *Materials Today: Proceedings* 25 (2020), pp. 833–837.

[39] Fei Chen, Mingyong Jia, Yulong She, Yueqi Wu, Qiang Shen, and Lianmeng Zhang. "Mechanical behavior of AlN/Mo functionally graded materials with various compositional structures". In: *Journal of Alloys and Compounds* 816 (2020), p. 152512.

[40] Wei-Ying Chen, Xuan Zhang, Meimei Li, Ruqing Xu, Cang Zhao, and Tao Sun. "Laser powder bed fusion of Inconel 718 on 316 stainless steel". In: *Additive Manufacturing* 36 (2020), p. 101500.

[41] Bishub Choudhury and M Chandrasekaran. "Investigation on welding characteristics of aerospace materials–A review". In: *Materials Today: Proceedings* 4.8 (2017), pp. 7519–7526.

[42] Patrick LJ Conway, TPC Klaver, Jacob Steggo, and Ehsan Ghassemali. "High entropy alloys towards industrial applications: high-throughput screening and experimental investigation". In: *Materials Science and Engineering: A* 830 (2022), p. 142297.

[43] CE Cross. "On the origin of weld solidification cracking". In: *Hot cracking phenomena in welds*. Springer, 2005, pp. 3–18.

[44] Sea Curtze, V-T Kuokkala, Aino Oikari, Juho Talonen, and Hannu Hänninen. "Thermodynamic modeling of the stacking fault energy of austenitic steels". In: *Acta Materialia* 59.3 (2011), pp. 1068–1076.

[45] L So Darken. "Diffusion, mobility and their interrelation through free energy in binary metallic systems". In: *Trans. Aime* 175 (1948), pp. 184–201.

[46] Tarasankar DebRoy et al. “Additive manufacturing of metallic components–process, structure and properties”. In: *Progress in Materials Science* 92 (2018), pp. 112–224.

[47] Naol Dessalegn Dejene and Hirpa G Lemu. “Current status and challenges of powder bed fusion-based metal additive manufacturing: literature review”. In: *Metals* 13.2 (2023), p. 424.

[48] Anton Du Plessis, Ina Yadroitsava, and Igor Yadroitsev. “Effects of defects on mechanical properties in metal additive manufacturing: A review focusing on X-ray tomography insights”. In: *Materials & Design* 187 (2020), p. 108385.

[49] B Dutta, S Palaniswamy, J Choi, L Song, and J Mazumder. “Direct metal deposition”. In: *Advanced materials & processes* (2011), p. 33.

[50] OV Eliseeva et al. “Functionally Graded Materials through robotics-inspired path planning”. In: *Materials & Design* 182 (2019), p. 107975.

[51] JW Elmer, DL Olson, and DK Matlock. “Thermal expansion characteristics of stainless steel weld metal.” In: *WELDING J.* 61.9 (1982), p. 293.

[52] PJ Ferreira and P Müllner. “A thermodynamic model for the stacking-fault energy”. In: *Acta Materialia* 46.13 (1998), pp. 4479–4484.

[53] Behzad Fotovvati, Steven F Wayne, Gladius Lewis, and Ebrahim Asadi. “A review on melt-pool characteristics in laser welding of metals”. In: *Advances in Materials Science and Engineering* 2018 (2018).

[54] Karin Frisk and Malin Selleby. “The compound energy formalism: applications”. In: *Journal of alloys and compounds* 320.2 (2001), pp. 177–188.

[55] Robert Fussik, Gero Egels, Werner Theisen, and Sebastian Weber. “Stacking fault energy in relation to hydrogen environment embrittlement of metastable austenitic stainless CrNi-steels”. In: *Metals* 11.8 (2021), p. 1170.

[56] Islam M El-Galy, Bassiouny I Bassiouny, and Mahmoud H Ahmed. “empirical model for dry sliding wear behaviour of centrifugally cast functionally graded Al/SiCp composite”. In: *Key Engineering Materials*. Vol. 786. Trans Tech Publ. 2018, pp. 276–285.

[57] Islam M El-Galy, Bassiouny I Saleh, and Mahmoud H Ahmed. “Functionally graded materials classifications and development trends from industrial point of view”. In: *SN Applied Sciences* 1 (2019), pp. 1–23.

[58] David Gandy et al. “Design, fabrication, and characterization of graded transition joints”. In: *Welding Journal* 96.8 (2017).

[59] Junheng Gao et al. “Enhancing strength and ductility in a near medium Mn austenitic steel via multiple deformation mechanisms through nanoprecipitation”. In: *Acta Materialia* 243 (2023), p. 118538.

[60] Easo P George, Dierk Raabe, and Robert O Ritchie. “High-entropy alloys”. In: *Nature reviews materials* 4.8 (2019), pp. 515–534.

[61] Reza Ghanavati, Erika Lannunziata, Ehsan Norouzi, Sara Bagherifard, Luca Iuliano, and Abdollah Saboori. “Design and development of SS316L-IN718 functionally graded materials via laser powder bed fusion”. In: *Materials Letters* 349 (2023), p. 134793.

[62] Reza Ghanavati et al. “Design optimization for defect-free AISI 316 L/IN718 functionally graded materials produced by laser additive manufacturing”. In: *Materials Characterization* 220 (2025), p. 114697.

[63] E Ghassemali and PLJ Conway. *High-throughput CALPHAD: a powerful tool towards accelerated metallurgy. Front Mater 9: 889771.* 2022.

[64] Paul J Gibbs, Patricia D Hough, K Thürmer, Brian P Somerday, C San Marchi, and Jonathan A Zimmerman. “Stacking fault energy based alloy screening for hydrogen compatibility”. In: *Jom* 72 (2020), pp. 1982–1992.

[65] Isabel Gómez-Palos, Miguel Vazquez-Pufleau, Jorge Valilla, Álvaro Ridruejo, Damien Tourret, and Juan J Vilatela. “Ultrafast synthesis of SiC nanowire webs by floating catalysts rationalised through in situ measurements and thermodynamic calculations”. In: *Nanoscale* 14.48 (2022), pp. 18175–18183.

[66] Dong Dong Gu, Wilhelm Meiners, Konrad Wissenbach, and Reinhart Poprawe. “Laser additive manufacturing of metallic components: materials, processes and mechanisms”. In: *International materials reviews* 57.3 (2012), pp. 133–164.

[67] GH Gulliver. “The quantitative effect of rapid cooling upon the constitution of binary alloys”. In: *J. Inst. Met* 9.1 (1913), pp. 120–157.

[68] Liuliu Han et al. “Thermodynamics-Guided High-Throughput Discovery of Eutectic High-Entropy Alloys for Rapid Solidification”. In: *Advanced Science* (2024), p. 2401559.

[69] DF Heaney, TW Mueller, and PA Davies. “Mechanical properties of metal injection moulded 316L stainless steel using both prealloy and master alloy techniques”. In: *Powder Metallurgy* 47.4 (2004), pp. 367–373.

[70] Alejandro Hinojos et al. “Joining of Inconel 718 and 316 Stainless Steel using electron beam melting additive manufacturing technology”. In: *Materials & Design* 94 (2016), pp. 17–27.

[71] Douglas C Hofmann et al. “Compositionally graded metals: A new frontier of additive manufacturing”. In: *Journal of Materials Research* 29.17 (2014), pp. 1899–1910.

[72] Douglas C Hofmann et al. “Developing gradient metal alloys through radial deposition additive manufacturing”. In: *Scientific reports* 4.1 (2014), pp. 1–8.

[73] Alex Huckstepp. “Digital Alloys Guide to Metal Additive Manufacturing Part 9 ; Directed Energy Deposition (DED)”. In: *https://www.digitalalloys.com/blog/directed-energy-deposition/* (2019).

[74] K Ishida. “Direct estimation of stacking fault energy by thermodynamic analysis”. In: *physica status solidi (a)* 36.2 (1976), pp. 717–728.

[75] L.E. Cambronero J.M Ruiz Prieto and J.M. Ruiz Roman. *Materiales Metalicos Volumen I; Aceros y Fundiciones*. Madrid, Spain: Escuela Tecnica Superior de Ingenieros de Minas, UPM, 2010.

[76] Chen Ji, Kun Li, Jianbin Zhan, Shengwen Bai, Bin Jiang, and Lawrence E Murr. “The effects and utility of homogenization and thermodynamic modeling on microstructure and mechanical properties of SS316/IN718 functionally graded materials fabricated by laser-based directed energy deposition”. In: *Journal of Materials Processing Technology* 319 (2023), p. 118084.

[77] Shuwei Ji, Zhonggang Sun, Wenshu Zhang, Xiaolong Chen, Guoliang Xie, and Hui Chang. “Microstructural evolution and high temperature resistance of functionally graded material Ti-6Al-4V/Inconel 718 coated by directed energy deposition-laser”. In: *Journal of Alloys and Compounds* 848 (2020), p. 156255.

[78] Liuchao Jin et al. “Big data, machine learning, and digital twin assisted additive manufacturing: A review”. In: *Materials & Design* 244 (2024), p. 113086.

[79] Paul Kah, Madan Shrestha, and Jukka Martikainen. “Trends in joining dissimilar metals by welding”. In: *Applied Mechanics and Materials*. Vol. 440. Trans Tech Publ. 2014, pp. 269–276.

[80] D Kaminski. “Laser Marking: How to choose the best laser for your marking application”. In: *Laser focus world* (2011).

[81] B Kieback, A Neubrand, and H Riedel. “Processing techniques for functionally graded materials”. In: *Materials Science and Engineering: A* 362.1-2 (2003), pp. 81–106.

[82] Sang Hoon Kim et al. “Selective compositional range exclusion via directed energy deposition to produce a defect-free Inconel 718/SS 316L functionally graded material”. In: *Additive Manufacturing* 47 (2021), p. 102288.

[83] YH Kim et al. “The effect of sigma phases formation depending on Cr/Ni equivalent ratio in AISI 316L weldments”. In: *Materials & Design* 32.1 (2011), pp. 330–336.

[84] JF King, MD Sullivan, and GM Slaughter. “Development of an improved stainless steel to ferritic steel transition joint”. In: *Welding Journal* 56.11 (1977), pp. 354–358.

[85] Tanner Kirk, Edgar Galvan, Richard Malak, and Raymundo Arroyave. "Computational design of gradient paths in additively manufactured functionally graded materials". In: *Journal of Mechanical Design* 140.11 (2018), p. 111410.

[86] Tanner Kirk, Richard Malak, and Raymundo Arroyave. "Computational Design of Compositionally Graded Alloys for Property Monotonicity". In: *Journal of Mechanical Design* 143.3 (2021), p. 031704.

[87] John Samuel Kirkaldy and David John Young. "Diffusion in the condensed state". In: *The Institute of Metals, 1 Carlton House Terrace, London SW 1 Y 5 DB, UK, 1987.* (1987).

[88] Christoph Klahn, Bastian Leutenecker, and Mirko Meboldt. "Design strategies for the process of additive manufacturing". In: *Procedia Cirp* 36 (2015), pp. 230–235.

[89] CY Kong, PA Carroll, P Brown, and RJ Scudamore. "The effect of average powder particle size on deposition efficiency, deposit height and surface roughness in the direct metal laser deposition process". In: *14th International Conference on Joining of Materials.* 2007.

[90] Sindo Kou. "A criterion for cracking during solidification". In: *Acta Materialia* 88 (2015), pp. 366–374.

[91] Sindo Kou. "Solidification and liquation cracking issues in welding". In: *Jom* 55 (2003), pp. 37–42.

[92] Robert Krakow et al. "On the crystallography and composition of topologically close-packed phases in ATI 718Plus®". In: *Acta Materialia* 130 (2017), pp. 271–280.

[93] Yen-Ling Kuo, Shota Horikawa, and Koji Kakehi. "The effect of interdendritic δ phase on the mechanical properties of Alloy 718 built up by additive manufacturing". In: *Materials & Design* 116 (2017), pp. 411–418.

[94] W 1 Kurz, B Giovanola, and R Trivedi. "Theory of microstructural development during rapid solidification". In: *Acta metallurgica* 34.5 (1986), pp. 823–830.

[95] Quan Lai et al. "Investigation of a novel functionally graded material for the repair of premium hypereutectoid rails using laser cladding technology". In: *Composites Part B: Engineering* 130 (2017), pp. 174–191.

[96] Dong Lang, Qiangguo Li, Xuefei Huang, and Weigang Huang. "Stacking fault energy and fcc→ hcp transformation driving force in Fe-Mn-C-Cr-Si high manganese steels and experimental investigation". In: *Materials Research Express* 8.8 (2021), p. 086507.

[97] Trong-Nhan Le and Yu-Lung Lo. "Effects of sulfur concentration and Marangoni convection on melt-pool formation in transition mode of selective laser melting process". In: *Materials & Design* 179 (2019), p. 107866.

[98] Kun Li et al. “A functionally graded material design from stainless steel to Ni-based superalloy by laser metal deposition coupled with thermodynamic prediction”. In: *Materials & Design* 217 (2022), p. 110612.

[99] PP Li, Maarten JC Sluijsmans, HJH Brouwers, and QL Yu. “Functionally graded ultra-high performance cementitious composite with enhanced impact properties”. In: *Composites Part B: Engineering* 183 (2020), p. 107680.

[100] Wei Li, Lei Yan, Xueyang Chen, Jingwei Zhang, Xinchang Zhang, and Frank Liou. “Directed energy depositing a new Fe-Cr-Ni alloy with gradually changing composition with elemental powder mixes and particle size’effect in fabrication process”. In: *Journal of Materials Processing Technology* 255 (2018), pp. 96–104.

[101] Weidong Li, Peter K Liaw, and Yanfei Gao. “Fracture resistance of high entropy alloys: A review”. In: *Intermetallics* 99 (2018), pp. 69–83.

[102] Weidong Li, Di Xie, Dongyue Li, Yong Zhang, Yanfei Gao, and Peter K Liaw. “Mechanical behavior of high-entropy alloys”. In: *Progress in Materials Science* 118 (2021), p. 100777.

[103] Weikai Li and Baohong Han. “Research and application of functionally gradient materials”. In: *IOP Conference Series: Materials Science and Engineering*. Vol. 394. 2. IOP Publishing. 2018, p. 022065.

[104] Yan Li et al. “A review on functionally graded materials and structures via additive manufacturing: from multi-scale design to versatile functional properties”. In: *Advanced Materials Technologies* 5.6 (2020), p. 1900981.

[105] John C Lippold and Damian J Kotecki. *Welding metallurgy and weldability of stainless steels*. 2005.

[106] Dejian Liu, John C Lippold, Jia Li, Stan R Rohklin, Justin Vollbrecht, and Richard Grylls. “Laser engineered net shape (LENS) technology for the repair of Ni-base superalloy turbine components”. In: *Metallurgical and Materials Transactions A* 45 (2014), pp. 4454–4469.

[107] Yang Liu, Yachao Wang, Xin Wu, and Jing Shi. “Nonequilibrium thermodynamic calculation and experimental investigation of an additively manufactured functionally graded material”. In: *Journal of Alloys and Compounds* 838 (2020), p. 155322.

[108] Yi-tong Long, Pu-lin Nie, Zhu-guo Li, Jian Huang, LI Xiang, and Xin-mei Xu. “Segregation of niobium in laser cladding Inconel 718 superalloy”. In: *Transactions of Nonferrous Metals Society of China* 26.2 (2016), pp. 431–436.

[109] Long Luo et al. “High-entropy alloys for solid hydrogen storage: a review”. In: *International Journal of Hydrogen Energy* 50 (2024), pp. 406–430.

[110] YW Luo, T Ma, WW Shao, GP Zhang, and B Zhang. "Effects of heat treatment on microstructures and mechanical properties of GH4169/K418 functionally graded material fabricated by laser melting deposition". In: *Materials Science and Engineering: A* 821 (2021), p. 141601.

[111] Rasheedat Modupe Mahamood, Esther Titilayo Akinlabi, Rasheedat Modupe Mahamood, and Esther Titilayo Akinlabi. "Types of functionally graded materials and their areas of application". In: *Functionally graded materials* (2017), pp. 9–21.

[112] TA Mai and AC Spowage. "Characterisation of dissimilar joints in laser welding of steel–kovar, copper–steel and copper–aluminium". In: *Materials Science and Engineering: A* 374.1-2 (2004), pp. 224–233.

[113] AK Mallik. "Computer calculations of phase diagrams". In: *Bulletin of Materials Science* 8 (1986), pp. 107–121.

[114] SGK Manikandan, D Sivakumar, K Prasad Rao, and M Kamaraj. "Laves phase in alloy 718 fusion zone—microscopic and calorimetric studies". In: *Materials Characterization* 100 (2015), pp. 192–206.

[115] Pablo Martin, Claudio E Madrid-Cortes, Camilo Cáceres, Nicolás Araya, Claudio Aguilar, and Jose Maria Cabrera. "HEAPS: A user-friendly tool for the design and exploration of high-entropy alloys based on semi-empirical parameters". In: *Computer Physics Communications* 278 (2022), p. 108398.

[116] RK McGeary. "Mechanical packing of spherical particles". In: *Journal of the American ceramic Society* 44.10 (1961), pp. 513–522.

[117] Xinliang Mei, Xiangyu Wang, Yinbo Peng, Hongyan Gu, Gaoyan Zhong, and Shoufeng Yang. "Interfacial characterization and mechanical properties of 316L stainless steel/inconel 718 manufactured by selective laser melting". In: *Materials Science and Engineering: A* 758 (2019), pp. 185–191.

[118] Daniel Melzer, Jan Džugan, Martina Koukolíková, Sylwia Rzepa, and Jaroslav Vavřík. "Structural integrity and mechanical properties of the Functionally Graded Material based on 316L/IN718 processed by DED technology". In: *Materials Science and Engineering: A* (2021), p. 141038.

[119] AP Miodownik. "The calculation of stacking fault energies in Fe, Ni, Cr alloys". In: *Calphad* 2.3 (1978), pp. 207–226.

[120] Daniel B Miracle and Oleg N Senkov. "A critical review of high entropy alloys and related concepts". In: *Acta materialia* 122 (2017), pp. 448–511.

[121] S Mocarski, DW Hall, RA Chernenkoff, DA Yeager, and CO McHugh. "Master alloys to obtain premixed hardenable powder metallurgy steels". In: *Powder metallurgy* 39.2 (1996), pp. 130–137.

[122] Ahad Mohammadzadeh et al. “Exploring the Impact of Configurational Entropy on the Design and Development of CoNi-Based Superalloys for Sustainable Applications”. In: *Journal of Alloys and Compounds* (2023), p. 171380.

[123] Abdel R Moustafa, A Durga, Greta Lindwall, and Zachary C Cordero. “Scheil ternary projection (STeP) diagrams for designing additively manufactured functionally graded metals”. In: *Additive Manufacturing* 32 (2020), p. 101008.

[124] Mohammad Zamani Nejad, Negar Alamzadeh, and Amin Hadi. “Thermoelastoplastic analysis of FGM rotating thick cylindrical pressure vessels in linear elastic-fully plastic condition”. In: *Composites Part B: Engineering* 154 (2018), pp. 410–422.

[125] Inwoong Noh, Jaehun Jeon, and Sang Won Lee. “A Study on Metallographic and Machining Characteristics of Functionally Graded Material Produced by Directed Energy Deposition”. In: *Crystals* 13.10 (2023), p. 1491.

[126] Warren Carl Oliver and George Mathews Pharr. “An improved technique for determining hardness and elastic modulus using load and displacement sensing indentation experiments”. In: *Journal of materials research* 7.6 (1992), pp. 1564–1583.

[127] GB Olson and Morris Cohen. “A general mechanism of martensitic nucleation: Part III. Kinetics of martensitic nucleation”. In: *Metallurgical Transactions A* 7 (1976), pp. 1915–1923.

[128] Malin Olsson. *Thermodynamic modeling of the stacking fault energy in austenitic stainless steels*. KTH Royal Institute of Technology, Stockholm, 2014.

[129] Raquel de Oro Calderon, Christian Gierl-Mayer, and Herbert Danninger. “Master alloys in powder metallurgy: the challenge of exploring new alloying compositions”. In: *Powder Metallurgy* 60.2 (2017), pp. 86–96.

[130] XF Peng, XP Lin, DJ Lee, Y Yan, and BX Wang. “Effects of initial molten pool and Marangoni flow on solid melting”. In: *International journal of heat and mass transfer* 44.2 (2001), pp. 457–470.

[131] A Perron et al. “Understanding sigma-phase precipitation in a stabilized austenitic stainless steel (316Nb) through complementary CALPHAD-based and experimental investigations”. In: *Acta Materialia* 79 (2014), pp. 16–29.

[132] Tresa M Pollock and Sammy Tin. “Nickel-based superalloys for advanced turbine engines: chemistry, microstructure and properties”. In: *Journal of propulsion and power* 22.2 (2006), pp. 361–374.

[133] W Pompe et al. “Functionally graded materials for biomedical applications”. In: *Materials Science and Engineering: A* 362.1-2 (2003), pp. 40–60.

[134] CMF Rae, MSA Karunaratne, CJ Small, RW Broomfield, CN Jones, and RC Reed. "Topologically close packed phases in an experimental rhenium-containing single crystal superalloy". In: *Superalloys* 2000 (2000), pp. 767–776.

[135] M Rappaz, J-M Drezet, and Met Gremaud. "A new hot-tearing criterion". In: *Metallurgical and materials transactions A* 30.2 (1999), pp. 449–455.

[136] KS Ravichandran. "Thermal residual stresses in a functionally graded material system". In: *Materials Science and Engineering: A* 201.1-2 (1995), pp. 269–276.

[137] Ashley Reichardt. *Additive Manufacturing of Metal-based Functionally Graded Materials*. University of California, Berkeley, 2017.

[138] Ashley Reichardt et al. "Advances in additive manufacturing of metal-based functionally graded materials". In: *International Materials Reviews* 66.1 (2021), pp. 1–29.

[139] Kandice SB Ribeiro, Fábio E Mariani, and Reginaldo T Coelho. "A study of different deposition strategies in direct energy deposition (DED) processes". In: *Procedia Manufacturing* 48 (2020), pp. 663–670.

[140] JL Robinson and MH Scott. "Liquation cracking during the welding of austenitic stainless steels and nickel alloys". In: *Philosophical Transactions of the Royal Society of London. Series A, Mathematical and Physical Sciences* 295.1413 (1980), pp. 105–117.

[141] Tiago A Rodrigues, Valdemar Duarte, RM Miranda, Telmo G Santos, and JP Oliveira. "Current status and perspectives on wire and arc additive manufacturing (WAAM)". In: *Materials* 12.7 (2019), p. 1121.

[142] Alireza Saeed-Akbari, J Imlau, U Prahl, and W Bleck. "Derivation and variation in composition-dependent stacking fault energy maps based on subregular solution model in high-manganese steels". In: *Metallurgical and Materials Transactions A* 40 (2009), pp. 3076–3090.

[143] Sandeep Sahu, James Harris, Andrew R Hamilton, and Nong Gao. "Interfacial characteristics of multi-material SS316L/IN718 fabricated by laser powder bed fusion and processed by high-pressure torsion". In: *Journal of Manufacturing Processes* 110 (2024), pp. 52–69.

[144] Bassiouny Saleh et al. "30 Years of functionally graded materials: An overview of manufacturing methods, Applications, and Future Challenges". In: *Composites Part B: Engineering* (2020), p. 108376.

[145] Manu Sam, R Jojith, and N Radhika. "Progression in manufacturing of functionally graded materials and impact of thermal treatment—A critical review". In: *Journal of Manufacturing Processes* 68 (2021), pp. 1339–1377.

[146] Noah Sargent, Yuankang Wang, Daozheng Li, Yunhao Zhao, Xin Wang, and Wei Xiong. "Exploring alloy design pathway through directed energy deposition of powder mixtures: A study of Stainless Steel 316L and Inconel 718". In: *Additive Manufacturing Letters* 6 (2023), p. 100133.

[147] Philippe Schaffnit, Charles Stallybrass, Joachim Konrad, Frank Stein, and Matthias Weinberg. "A Scheil–Gulliver model dedicated to the solidification of steel". In: *Calphad* 48 (2015), pp. 184–188.

[148] Kamran Shah. *Laser direct metal deposition of dissimilar and functionally graded alloys*. The University of Manchester (United Kingdom), 2011.

[149] Kamran Shah, Izhar ul Haq, Ashfaq Khan, Shaukat Ali Shah, Mushtaq Khan, and Andrew J Pinkerton. "Parametric study of development of Inconel-steel functionally graded materials by laser direct metal deposition". In: *Materials & Design (1980-2015)* 54 (2014), pp. 531–538.

[150] V Shankar, TPS Gill, SL Mannan, and S Sundaresan. "Solidification cracking in austenitic stainless steel welds". In: *Sadhana* 28 (2003), pp. 359–382.

[151] VN Shivanyuk, J Foct, and VG Gavriljuk. "On a role of hydrogen-induced ε-martensite in embrittlement of stable austenitic steel". In: *Scripta Materialia* 49.6 (2003), pp. 601–606.

[152] Chester Thomas Sims, Norman S Stoloff, and William C Hagel. *superalloys II*. Vol. 8. Wiley New York, 1987.

[153] John A Slotwinski, Edward J Garboczi, Paul E Stutzman, Chiara F Ferraris, Stephanie S Watson, and Max A Peltz. "Characterization of metal powders used for additive manufacturing". In: *Journal of research of the National Institute of Standards and Technology* 119 (2014), p. 460.

[154] Karl Gunnar Solheim, Jan Ketil Solberg, John Walmsley, Fredrik Rosenqvist, and Tor Henning Bjørnå. "The role of retained austenite in hydrogen embrittlement of supermartensitic stainless steel". In: *Engineering Failure Analysis* 34 (2013), pp. 140–149.

[155] Thabang R Somo, Mykhaylo V Lototskyy, Volodymyr A Yartys, Moegamat Wafeeq Davids, and Serge Nyallang Nyamsi. "Hydrogen storage behaviours of high entropy alloys: A Review". In: *Journal of Energy Storage* 73 (2023), p. 108969.

[156] Jiří Sopoušek and Rudolf Foret. "More sophisticated thermodynamic designs of welds between dissimilar steels". In: *Science and Technology of Welding and Joining* 13.1 (2008), pp. 17–24.

[157] Tayfun Soysal and Sindo Kou. "A simple test for assessing solidification cracking susceptibility and checking validity of susceptibility prediction". In: *Acta Materialia* 143 (2018), pp. 181–197.

[158] PJ Spencer. “A brief history of CALPHAD”. In: *Calphad* 32.1 (2008), pp. 1–8.

[159] Soumya Sridar, Noah Sargent, Xin Wang, Michael A Klecka, and Wei Xiong. “Determination of location-specific solidification cracking susceptibility for a mixed dissimilar alloy processed by wire-arc additive manufacturing”. In: *Metals* 12.2 (2022), p. 284.

[160] Amanda J Sterling, Brian Torries, Nima Shamsaei, Scott M Thompson, and Denver W Seely. “Fatigue behavior and failure mechanisms of direct laser deposited Ti–6Al–4V”. In: *Materials Science and Engineering: A* 655 (2016), pp. 100–112.

[161] Yi Su, Bo Chen, Caiwang Tan, Xiaoguo Song, and Jicai Feng. “Influence of composition gradient variation on the microstructure and mechanical properties of 316 L/Inconel718 functionally graded material fabricated by laser additive manufacturing”. In: *Journal of Materials Processing Technology* 283 (2020), p. 116702.

[162] Waheed Ul Haq Syed, Andrew J Pinkerton, and Lin Li. “A comparative study of wire feeding and powder feeding in direct diode laser deposition for rapid prototyping”. In: *Applied surface science* 247.1-4 (2005), pp. 268–276.

[163] SM Teus, VN Shyvanyuk, and VG Gavriljuk. “Hydrogen-induced $\gamma \rightarrow \varepsilon$ transformation and the role of ε-martensite in hydrogen embrittlement of austenitic steels”. In: *Materials Science and Engineering: A* 497.1-2 (2008), pp. 290–294.

[164] RG Thompson and S Genculu. “Microstructural evolution in the HAZ of Inconel 718 and correlation with the hot ductility test”. In: *Welding journal* 62.12 (1983), 337s–345s.

[165] Beril Tonyali et al. “Additively manufactured Ni-20Cr to V functionally graded material: Computational predictions and experimental verification of phase formations”. In: *Journal of Alloys and Compounds* 985 (2024), p. 174011.

[166] José Manuel Torralba, Paula Alvaredo, and Andrea García-Junceda. “High-entropy alloys fabricated via powder metallurgy. A critical review”. In: *Powder Metallurgy* 62.2 (2019), pp. 84–114.

[167] Ming-Hung Tsai and Jien-Wei Yeh. “High-entropy alloys: a critical review”. In: *Materials Research Letters* 2.3 (2014), pp. 107–123.

[168] Axel Van De Walle and Mark Asta. “High-throughput calculations in the context of alloy design”. In: *MRS Bulletin* 44.4 (2019), pp. 252–256.

[169] Ayush Verma, Angshuman Kapil, Damjan Klobčar, and Abhay Sharma. “A review on multiplicity in multi-material additive manufacturing: process, capability, scale, and structure”. In: *Materials* 16.15 (2023), p. 5246.

[170] Axel van de Walle, Ruoshi Sun, Qi-Jun Hong, and Sara Kadkhodaei. "Software tools for high-throughput CALPHAD from first-principles data". In: *Calphad* 58 (2017), pp. 70–81.

[171] HT Wang, GZ Wang, FZ Xuan, and ST Tu. "Fracture mechanism of a dissimilar metal welded joint in nuclear power plant". In: *Engineering Failure Analysis* 28 (2013), pp. 134–148.

[172] L Wang, S Felicelli, Y Gooroochurn, PT Wang, and MF Horstemeyer. "Optimization of the LENS® process for steady molten pool size". In: *Materials Science and Engineering: A* 474.1-2 (2008), pp. 148–156.

[173] N Wang, S Mokadem, M Rappaz, and W Kurz. "Solidification cracking of superalloy single-and bi-crystals". In: *Acta materialia* 52.11 (2004), pp. 3173–3182.

[174] Xin Wang, Soumya Sridar, and Wei Xiong. "Thermodynamic investigation of new high-strength low-alloy steels with heusler phase strengthening for welding and additive manufacturing: high-throughput CALPHAD calculations and key experiments for database verification". In: *Journal of Phase Equilibria and Diffusion* 41 (2020), pp. 804–818.

[175] Zhangwei Wang et al. "High stress twinning in a compositionally complex steel of very high stacking fault energy". In: *Nature communications* 13.1 (2022), p. 3598.

[176] Zhou Wang, Alan C. Bovik, Hamid R. Sheikh, and Eero P. Simoncelli. "Image Quality Assessment: From Error Visibility to Structural Similarity". In: *IEEE Transactions on Image Processing* 13.4 (Apr. 2004), pp. 600–612.

[177] Konstantin V Werner, Frank Niessen, Matteo Villa, and Marcel AJ Somers. "Experimental validation of negative stacking fault energies in metastable face-centered cubic materials". In: *Applied Physics Letters* 119.14 (2021).

[178] Wessel W Wits and Emiel Amsterdam. "Graded structures by multi-material mixing in laser powder bed fusion". In: *CIRP Annals* 70.1 (2021), pp. 159–162.

[179] Bintao Wu et al. "A review of the wire arc additive manufacturing of metals: properties, defects and quality improvement". In: *Journal of manufacturing processes* 35 (2018), pp. 127–139.

[180] Dongjiang Wu, Xiaokang Liang, Qian Li, and Lijia Jiang. "Laser rapid manufacturing of stainless steel 316L/Inconel718 functionally graded materials: microstructure evolution and mechanical properties". In: *International Journal of Optics* 2010 (2010).

[181] Hui Xiao, Simeng Li, Xu Han, Jyoti Mazumder, and Lijun Song. "Laves phase control of Inconel 718 alloy using quasi-continuous-wave laser additive manufacturing". In: *Materials & Design* 122 (2017), pp. 330–339.

[182] Li Xing, Wang Quanjie, Zhang Qirui, Guan Yingchun, and Zhou Wei. "Interface analyses and mechanical properties of stainless steel/nickel alloy induced by multi-metal laser additive manufacturing". In: *Journal of Manufacturing Processes* 91 (2023), pp. 53–60.

[183] Gang Xu, Runbao Wu, Kaiyu Luo, and Jinzhong Lu. "Effects of heat treatment on hot corrosion behavior of directed energy deposited In718/316L functionally graded material". In: *Corrosion Science* 197 (2022), p. 110068.

[184] Ming Yan and Peng Yu. "An Overview of densification, microstructure and mechanical property of additively manufactured Ti-6Al-4V—Comparison among selective laser melting, electron beam melting, laser metal deposition and selective laser sintering, and with conventional powder". In: *Sintering techniques of materials* (2015).

[185] Fusheng Yang et al. "Recent progress on the development of high entropy alloys (HEAs) for solid hydrogen storage: A review". In: *International Journal of Hydrogen Energy* 47.21 (2022), pp. 11236–11249.

[186] Seung Weon Yang, Jongcheon Yoon, Hyub Lee, and Do Sik Shim. "Defect of functionally graded material of inconel 718 and STS 316L fabricated by directed energy deposition and its effect on mechanical properties". In: *Journal of Materials Research and Technology* 17 (2022), pp. 478–497.

[187] Songge Yang, Jun Lu, Fangzhou Xing, Lijun Zhang, and Yu Zhong. "Revisit the VEC rule in high entropy alloys (HEAs) with high-throughput CALPHAD approach and its applications for material design-A case study with Al–Co–Cr–Fe–Ni system". In: *Acta Materialia* 192 (2020), pp. 11–19.

[188] Zhening Yang, Cory D Jamieson, Zi-Kui Liu, and Allison M Beese. "Effect of Dilution on Fabricated Functionally Graded Materials Compositions: Modelling and Mitigation Methods". In: *SSRN 4914959* (2024).

[189] Zhening Yang, Hui Sun, Zi-Kui Liu, and Allison M Beese. "Design methodology for functionally graded materials: Framework for considering cracking". In: *Additive Manufacturing* 73 (2023), p. 103672.

[190] Chi Zhang et al. "Additive manufacturing of functionally graded materials: A review". In: *Materials Science and Engineering: A* 764 (2019), p. 138209.

[191] Cong Zhang et al. "High-throughput thermodynamic calculations of phase equilibria in solidified 6016 Al-alloys". In: *Computational Materials Science* 167 (2019), pp. 19–24.

[192] Jize Zhang, Rui Wang, and Yu Zhong. "Identification of the Eutectic Points in the Multicomponent Systems with the High-Throughput CALPHAD Approach". In: *Journal of Phase Equilibria and Diffusion* 43.6 (2022), pp. 844–857.

[193] Yong Zhang et al. “Microstructures and properties of high-entropy alloys”. In: *Progress in materials science* 61 (2014), pp. 1–93.

[194] Zongyin Zhang and Rolf Sandström. “Fe–Mn–Si master alloy steel by powder metallurgy processing”. In: *Journal of alloys and Compounds* 363.1-2 (2004), pp. 199–207.

[195] HH Zhu, JYH Fuh, and L Lu. “The influence of powder apparent density on the density in direct laser-sintered metallic parts”. In: *International Journal of Machine Tools and Manufacture* 47.2 (2007), pp. 294–298.

[196] Andreas Züttel. “Materials for hydrogen storage”. In: *Materials today* 6.9 (2003), pp. 24–33.